ANALYSIS AND SYNTHESIS OF SERIES DAMPER ACTUATOR

ZHOU WEI

(M.Eng, 2002)

A DISSERTATION SUBMITTED FOR

THE DEGREE OF DOCTOR OF PHILOSOPHY

DEPARTMENT OF MECHANICAL ENGINEERING

NATIONAL UNIVERSITY OF SINGAPORE

2007

Acknowledgements

The four-year study in NUS is an incredible experience for me and would be truly appreciated all through the rest of my life.

First of all I would like to thank my supervisors, Dr. Chee-Meng Chew and A/P. Geok-Soon Hong, for their advice, guidance, help, encouragement and support over these years. It has been a great pleasure to learn from them as advisors, teachers, mentors and especially friends.

Thanks to Eddie Choong who helped me during the initial stage in Control Lab. He had given me a lot of valuable suggestions and help that enabled me to start my research work smoothly and successfully. The Control Lab is a great place to do research work due to these agile and talented people - Ho Hoan Nigha, Talasila Sateesh, Sim Wai Yong, Feng Kai, Samuel and Hang Wei Wei. Living, studying and working with them has been a great pleasure and valuable experience.

I am also want to thank all the lab staff in Control Lab, Mr. Yee Chong Seng, Ms. Ooi-Toh Chew Hoey, Ms. Tshin Oi Meng, Mr. Zhang and Ms. Hamidah Bte Jasman, for their creating an ideal research environment and providing endless assistance.

I particularly appreciate the support from my family. Thanks to my parents and sisters for their love and support over these years. Special thanks to my recent arriving baby, Zi Han. Her crying on overseas call has been a strong motivation for me to finish up early.

Finally, I give my deep appreciation to my eternal companion Ma Ling. She has alone undertaken the burden of family for these years without any complain. I am

thankful for her love, faith, support, responsibility, selflessness and gentleness.

Table of contents

Abstract

The overall objective of this thesis is to develop a novel type of force control actuator for biomimetic systems to obtain good output force fidelity, low output impedance and high system bandwidth and, furthermore, ease the design tradeoffs that exist in Series Elastic Actuator system.

To achieve this objective, a novel force/torque control actuator called Series Damper Actuator (SDA) is proposed, modelled, analyzed, designed and tested. The proposed SDA system incorporates a series damper instead of a series elastic component between the actuator and the load. The system is designed to effectively control the relative velocity in the damper to achieve the desired force given the damping coefficient. An experimental SDA system is developed, in which a Magneto-Rheological (MR) fluid damper is employed as the series damper to achieve variable damping coefficient. The dynamic property of SDA system based on MR damper is analyzed. The effect of extra dynamics introduced by the MR fluid damper is revealed by comparing SDA based on MR fluid damper with SDA based on a linear Newtonian viscous damper. To linearize MR fluid damper and compensate the effect of its extra dynamics, a modified Bingham Model is proposed to give inverse dynamics compensation for the MR damper. Force feedback control loop based on this inverse model is implemented after damper linearization. System is tested and experimental results are also presented. Plant design problems of SDA system are investigated in the aspects of plant component selection, design optimization based on Mechatronic Design Quotient (MDQ) and design of a compact MR fluid damper.

Compared to conventional force/torque control schemes and Series Elastic Actu-

ator (SEA), SDA has good output force/torque fidelity, low output impedance and large force/torque range. Furthermore, varying damping coefficient endows the SDA with more advantages, eases the design tradeoffs and makes the system more versatile. The experimental results show that SDA system is an effective force/torque control actuator with high performance.

List of Figures

List of Tables

Chapter 1

Introduction

1.1 Motivation

Robotics has shown a rapid progress in past decades and robots have been successfully applied in vast fields. The main successful applications of robots involve the tasks to control the position, trajectory or velocity for each degree of freedom (DOF) of robot (Kuntze, 1988; Kazanzides, 1989; Cetinkunt, 1990; Shin, 1999). Traditional robots can do this with high speed, endurance, precision and accuracy. Robots have been used in the field where repetitive tasks require high precision and accuracy and are difficult and tedious for humans, for example, chips picking, automatic welding, and spray painting and so on.

However there are many tasks, such as walking, running, jumping, grasping, catching and manipulation, in which the robot performance, despite extensive research, is inferior to its biological counterparts. These tasks all require interacting with the real world which is usually unknown to robots. Force/torque control is necessary when robots need to interact with the unknown environment (Steven, 1989; Nitish, 1994). This is especially true for robotics system such as assembly manipulators, legged robots, haptic devices, tele-operation robots system, and so on (Sakakibara, 1996; Carignan, 2000; Shen, 2003; Pratt, 2004). Successful force control (from here force control generally represents force/torque control) includes two aspects. One is to use algorithms and sensory information to determine the

desired force for each actuator on robots so that desired interacting force can be achieved on robot-environment interface (Antonelli, 2001; Roy, 2002; Bojan, 2002). The other aspect of successful force control is to generate the desired force on each actuator (Sun, 1999; Erika, 2000; Grant, 2000; Abidi, 2004). This thesis deals with the second aspect of force control and especially on the actuators that generate the forces.

For a long time, actuation technology had been typically poor at generating and maintaining accurate output force and, especially, holding a low output impedance for the environment (Pratt, 1995-2). Traditionally and also most commonly, force control would be achieved with a force sensor located at the point where the interacting force is to be controlled, to implement a force feedback control loop (Xu, 1988; Youcef, 1989; Sugano, 1992; Dieter, 1995). In these schemes, force control is achieved without direct control of the output force of the actuator. This method is simple but has a relatively low performance.

Actuator technology has improved greatly since the idea of force control actuator was proposed. A good solution of force control actuator is called series elastic actuator (SEA)(Pratt, 1995-1; Williamson, 1995; Robinson, 1999; Sulzer, 2005; Sensinger, 2005), which was proposed by the MIT legged locomotion group in the last decade. The SEA system introduces a series elastic component between the output end of motor and load and therefore reduces the system stiffness. Such a configuration gives the actuator a lot of advantages over conventional force control method, such as good output force fidelity, low output impedance and therefore high impact tolerance ability.

To give more background knowledge and relevant information, a detailed literature review of the relative work about force control and force control actuators will be presented in Chapter 2.

1.2 Thesis Contribution

In this thesis, we will propose a novel force control actuator system called "Series Damper Actuator" (SDA) . Having a similar structure to Series Elastic Actuator (SEA), SDA system adopts a damper as its series component rather than an elastic component, e.g. a spring, in the SEA system. Two different types of damper will be proposed as the series damper in the SDA system. Besides the common linear viscous damper which has a fixed damping constant, nonlinear Magneto-Rheological (MR) fluid damper is also proposed for the SDA system so that variable damping coefficient can be achieved. The suggested SDA system will be modeled, analyzed and evaluated based on its force control performances, i.e. system bandwidth, output impedance, impact tolerance and system efficiency. The controller design for SDA actuator system will be described especially for the SDA system based on nonlinear MR fluid damper, for which the control problem is much more difficult than that of linear viscous damper. Dynamics of MR will be analyzed and modeled. A new MR damper model, modified Bingham Model, will be proposed to implement inverse dynamics control for the SDA system based on MR fluid damper. Design procedures of SDA plant will also be investigated, including the steps for plant component selection, design optimization based on Mechatronic Design Quotient (MDQ), and the design of a novel compact MR fluid damper.

The Series Damper Actuator system described in this thesis could provide a better force control implementation for compliant actuation of robot. The study and analysis of this thesis may provide a better understanding of SDA system and give some basic guidelines for engineers when they design such an actuator system. The proposed SDA system, a force control actuator system, should have a broad application range covering the fields such as humanoids robots, industrial manipulators, teleoperation systems, haptic devices, virtual reality systems, and so on.

As a summary, the contributions of this thesis are:

1. Proposing a novel force control actuator, series damper actuator (SDA) inspired from an existing force control actuator, series elastic actuator (SEA).

2. Modelling SDA system and analyzing the system properties in terms of system bandwidth, output impedance, impact tolerance ability and system efficiency. Proving the feasibility of SDA system for force control applications.

3. Investigating the effect of the extra dynamics caused by the introduction of Magneto-Rheological (MR) fluid damper on the overall system performance.

4. Developing control schemes for SDA system considering the extra dynamics of the series damper.

5. Proposing a new MR fluid damper model, modified Bingham model, to implement inverse dynamics control for SDA based on MR fluid damper with good force control performance achieved.

6. Revealing the hardware design procedures for SDA system, including plant component selection and optimization based on Mechatronic Design Quotient (MDQ).

7. Developing a compact MR fluid damper design with novel double-disc structure, including damper structure design, FEA analysis, dimensional optimization, and prototyping and testing.

This thesis will not address such problems as actuator saturation analysis and control, design for a viscous damper, and properties of series damper actuators with other types of driving source, e.g. hydraulic pumps, pneumatic pistons and so on.

1.3 Organisation of Thesis

The thesis proceeds as follows:

Chapter 1 gives a brief introduction to the motivation of the thesis and highlights the main contributions.

Chapter 2 presents the background study for this thesis, including force control and force control actuators.

Chapter 3 presents the concept of series damper actuator, describes the models and analyzes the force control properties by comparing with series elastic actuator.

Chapter 4 analyzes the effect of the extra dynamics of Magneto-Rheological fluid damper on the overall system control properties.

Chapter 5 describes the controller design for SDA systems. A novel MR fluid damper model is proposed to implement inverse dynamics control for SDA system based on MR fluid damper. Experimental results is also shown to proof the properness of the designed controllers.

Chapter 6 describes the plant design procedures for SDA system, including plant component selection, Mechatronic Design Quotient (MDQ) based optimization, and a novel MR fluid damper designing.

Chapter7 concludes the thesis with discussion and advice on future research.

Chapter 2

Background and Related Work

Force control is necessary for controlled interaction between a robot and an external unknown environment (Whitney, 1985; Gorinevsky, 1997; Yoshikawa, 2000). The purpose of force control could be quite diverse, such as applying a controlled force needed for a manufacturing process (e.g. deburring or grinding), pushing a external object using a controlled force, and dealing with geometric uncertainty by establishing controlled contacts (e.g. in assembly).

2.1 Force Control and Its Applications

The vast majorities of force control techniques and algorithm have been developed to control and monitor the end effector forces or torques with or without a force sensor at the robot tip (Nitish, 1994; Gorinevsky, 1997; Siciliano, 1998). Those various force control strategies include passive compliance, pure force control, impedance control, hybrid position/force control, and so on.

Passive compliance (Goswami, 1991, 1993)is the simplest way to achieve pseudo force control. Different from the other three methods, it is not a truly force control since it doesn't use force information to implement feedback control. With passive compliance, the robot can do certain environment interaction tasks successfully by using only position control, such as grasping and holding objects.

Pure force control (Vischer, 1995; Nitish, 1994)is to simply control the interaction force based on only force sensor feedback, disregarding the information such as velocity and position. The control reference represents the desired interaction force. The controller input is the error between the desired force and the actual measured endpoint force. There is no position or velocity feedback which means that there is no control on the absolute endpoint position or velocity.

Impedance control (Hogan, 1985; Anderson, 1988; Valency, 2000)generalizes the ideas of stiffness control and damping control, which measure the endpoint forces as well as the joint positions and velocities in order to generate a desired force output relating to the virtual spring and damper. For impedance control, the endpoint will behave as if it is a second order (elastic and damping) system. Therefore the endpoint force, joint positions and velocities are used to generate actuator forces/torques. The gain matrices which set the stiffness, damping and inertia of the manipulator endpoint correlate directly with stability and bandwidth criteria for the robot. Impedance control works with dynamics constraints.

Hybrid position/force control(Raibert, 1981; Yang, 1995; Budiman, 1999; Goldsmith, 1999) is a method that combines conventional position control and force control. The environment dictates natural constraints where only force control can be used. Similarly, position control is used in the directions where there are no constraints and the robot can move freely. Hybrid position/force control works with geometry constraints.

Application of force control is quite versatile in modern industry and research. For industry manipulators, force control is employed for the tasks such as assembly, packing, surface machining (e.g. grinding and drilling), and so on. Haptic devices need force control to generate force depending on the motion of the user to create a virtual environment. Teleoperation system always has a local force control loop for the master to duplicate the force felt by the slave, which can improve the overall

performance of the whole system(Zhu, 1999; Lonnie, 2004). Biomimetic robots, such as bipedal walking robots, need force controlled actuation to generation soft, compliant and force controlled movements and therefore behavior as naturally as biological systems(Robinson, 1999; Caldwell, 2001).

2.2 Force control implementations

2.2.1 Conventional Method

To implement force control, the conventional and also the most popular method is to use the strain gauge setup to obtain the force signal (Yabuta, 1988; Wilfinger, 1994; Whitcomb, 1995; Cortesao, 2000). Figure 2.1 shows a typical implementation of force control for manipulator with a strain gauge sensor.

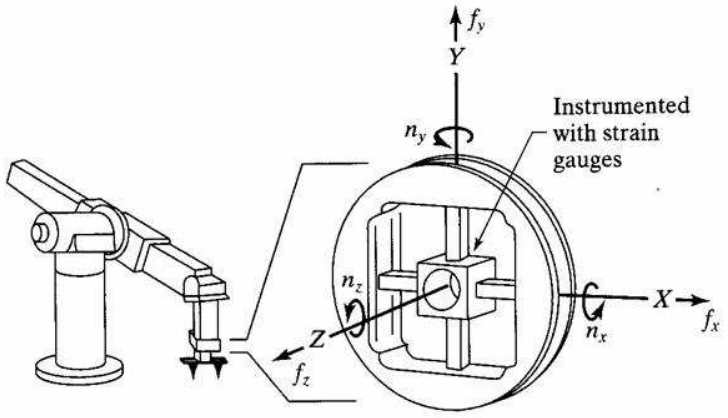

Figure 2.1: A typical implementation for manipulator force control

In this case, the sensor usually is located at the end effector of the manipulator, where the interaction force is intended to be controlled. A closed-loop controller would be built based on the feedback of the force sensor. The robot joints or system actuators are driven and controlled accordingly so that the desired force can be achieved at that location. This method is simple and effective to achieve force control.

But it is well known that the force sensor, e.g. typically a strain gauge, has a

significant sensor noise. Therefore, the force control performance of this method is poor due to its low signal-to-noise ratio. Although the using of low pass signal filter can get a clear force signal from force sensor, such signal processing always, more or less, distorts the signal from it true value and hence compromises the system control performance, especially when the noise band is close to that of the signal. Furthermore, traditional robot design had a maximized structure stiffness to obtain the precision, stability and bandwidth of position control. Because of high structural stiffness, such design strategy is not suitable to be used for biomimetic legged robots or haptic devices, which require their joints to be both compliant and precisely force-controlled to interact with unknown environments. The idea that reducing stiffness between an actuator and load for the robot joints can increase the robot force control performance was accepted by engineers gradually.

Another well known problem for robot force control is dynamical noncolocation, which may significantly limit the closed-loop performance (Gevarter, 1970; Colgate, 1989; Steven, 1989). The noncolocation problem was first noted by Gevarter (Gevarter, 1970). It was shown that, if an actuator and sensor are physically located at different points on a flexible structure, then there will be unstable modes in the closed-loop system. Steven has investigated some dynamics problems in robot force control, including the noncolocation (Steven, 1989). He concluded that the frequency of the lowest dynamically noncolocated mode is a fundamental limitation for conventional PD controllers. Therefore, Locating the force sensor physically to the actuator to implement a locale force feedback control loop can effectively minimize the noncolocation problem.

Consequently, the concept of compliant robot force controlled actuation appeared in 1990s with the proposal of Series Elastic Actuator, a kind of force control actuator.

2.2.2 Force Control Actuator - Series Elastic Actuator

A type of force control actuator is called "series elastic actuator" (SEA) (Pratt, 1995; Williamson, 1995; Robinson, 1999), which was proposed by MIT leg laboratory. SEA uses springs in the series elastic component between the motor and the load. The

output force can be indirectly controlled by controlling the deformation (measured by a sensor) of the springs, given the spring constants. Figure 2.2 shows a principle diagram of Series Elastic Actuator with a force feedback closed-loop system.

(a)

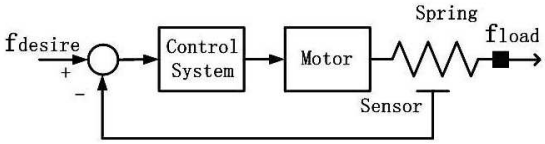

(b)

Figure 2.2: Series elastic actuator. (a) Picture of series elastic actuator plant. (b) Block diagram of series elastic actuator system. The closed-loop series elastic actuator is topologically identical to any motion actuator with a load sensor and closed-loop feedback controller. The major difference is that the sensor is very compliant.

The closed-loop SEA actuator is topologically identical to any motion actuator with a load sensor and closed-loop feedback controller. The major difference is that the sensor is very compliant. The sensor measures the deflection or strain in the spring which is a representation of the force, , acting through the spring. By controlling this deflection, the output force/torque is essentially controlled according to Hooke's law:

$$F = k_e X$$

where k_e is the spring constant and X is the spring deflection.

G. A. Pratt [1995] and D. W. Robinson [1999] had analyzed the properties of Series Elastic Actuator. Its application performance was also evaluated on two different real robot systems, which perform some natural tasks such as walking and

manipulation. The primary advantage of series elasticity is that the compliant load bearing sensor lowers the loop gain of the closed-loop system. The control gain can be proportionally increased to maintain the overall loop gain of the actuator at desired stability margins. This allows series elastic actuators to have low output impedance, be tolerant to shock loading and robust to changing loads.

However, the introduction of the spring in the series elastic actuator system increases the compliance of system, and the bandwidth and the stability margin of the system is reduced greatly. Low bandwidth has greatly limited the application of such force control system in some robot systems such as force feedback virtual reality systems. Furthermore the selection of the spring stiffness for series elastic component, e.g. a spring, is mainly governed by the trade-offs among the force bandwidth, force range and impact tolerance. Due to the fact that the spring stiffness is usually a constant (since it is difficult to achieve variable spring-stiffness design), it is very hard to achieve good force fidelity at both low and high end range. Detailed analysis regarding this will be given in the next chapter.

2.2.3 Series Damper Actuator

To solve the problem highlighted for the SEA and to ease the design tradeoffs, we propose a novel force control actuator system called "Series Damper Actuator" (SDA) (Chew, 2004-1, 2004-2; Zhou, 2002). Fig.2.3 shows a picture of SDA plant and a principle sketch of SDA system.

The SDA system consists of an actuator (e.g. a motor with gear transmission) and a damper connected in series. A velocity sensor is used to measure the relative velocity between the input and output of the damper. An appropriate force feedback controller is then implemented to indirectly control the output force by driving the actuator so that the desired relative velocity in the damper is achieved (since the damping coefficient is known). The force experienced in the damper is the same as that experienced by the load. The controlled output force can be known from the

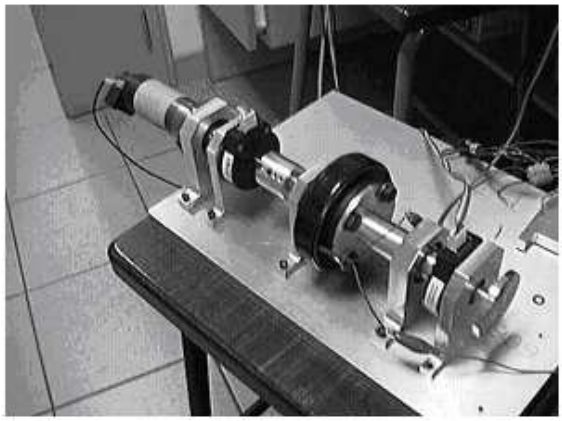

(a)

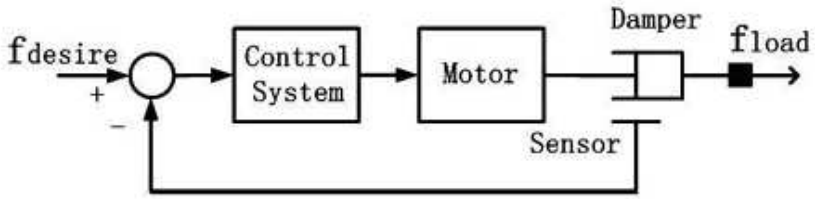

(b)

Figure 2.3: Series Damper actuator. (a) Picture of series damper actuator plant. (b) Block diagram of series elastic actuator system.

following damping force equation (for linear viscous damper):

$$F = k_b v$$

where F is the output force of the Series Damper Actuator, k_b is the damping coefficient and v is the relative velocity in the damper.

Compared with the SEA system, the SDA uses a series damping component instead of a series elastic component for force control. The damping component will not add to the order of the system as the spring does in the SEA, and the stability margin of the SDA system is not significantly affected. Another advantage of SDA is that the damping coefficient of the damper can easily be made variable by adopting an appropriate damper design. For example, one possible approach is to adopt Magneto-rheological (MR) fluid for the damper so that it has variable viscosity. The damping coefficient can then be adjusted according to the operating conditions. For example, the damping coefficient could be increased and reduced

for high and low force, respectively, so that good force fidelity could be achieved in both cases. This endows the system with large force bandwidth.

Furthermore, the SDA has good impact absorption due to the series damper. This will help to reduce the rate of wear experienced by the actuator (for example, the gear transmission of the electric motor will breakdown very soon if there is no impact absorption between the load and the output of the gear transmission). This characteristic is very important for those systems which are required to interact frequently with unknown environment. Examples of such systems are walking robots, haptic devices, robot manipulators, etc.

2.2.4 Other Force Control Actuator Solutions

2.2.4.1 Micro-Macro Motor Actuator

To overcome the force control performance limitation of actuators, the concept of micro-macro actuators was introduced (Morrell, 1995, 1996; Lee, 2002; Zinn, 2002-1). Zinn combined the SEA with the concept of micro-macro actuator to solve the low bandwidth problem of SEA and porposed a new robot actuation structure, called Distribute Macro-Mini (DM^2) Actuator (Zinn, 2002-1, 2002-2, 2002-3).

Picture 2.4 shows the DM^2 actuator approach, which employs two distribute motors (a macro motor and a mini motor) for each actuator. The torque generation is partitioned into low and high frequency components for mini and macro motors respectively. This method can maintain high actuator bandwidth; reduce the effective inertia of the manipulator; and obtain low output impedance and, thereafter, the human interaction safety.

However, this approach employs a pair of actuators which are connected in parallel. One of which is used to realize the low-frequency torque generation. The other one is for the high frequency. Therefore the system is more complex and costlier due to the requirement of additional actuators. Furthermore, the actual force output is the summation of those two motors, Micro and Macro motors, hence the output force performance in its frequency range relies on the performance of each motor

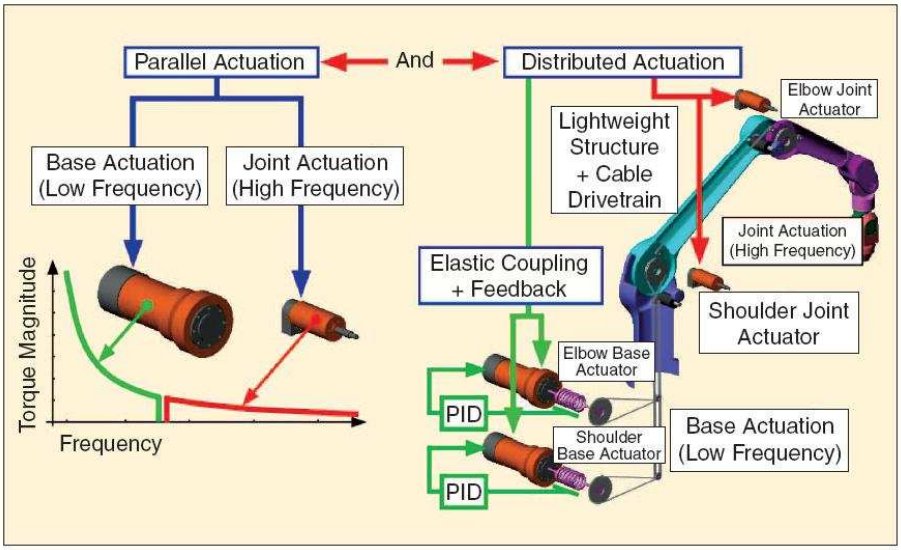

Figure 2.4: DM^2 actuator approach

and their combination.

2.2.4.2 Magneto-Rheological Fluid Actuator

Intelligent materials, such as Electro-Rheological (ER) fluids and Magneto-Rheological fluids, have been used in force control actuators for the special control properties of them (Stanway, 1995; Sakaguchi, 1998; Takesue, 2000). MR fluid actuator had been proposed and prototypes of such actuator system had been successfully developed by Professor Furusho's group several years ago (Takesue, 2000, 2001, 2002, 2003). Fig.2.5 shows a MR actuator, MRA2, developed by Furusho's group. In this actuator system, MR fluid damper was employed and located between a motor and load. By controlling the damper input current, the output torque of the actuator was effectively achieved with high precision.

For this actuator system, it assumes that the output force is not dependent on the input/output relative velocity of the damper. The drive unit (motor) mainly acts as a velocity source to one end of the MR damper. The output force of the actuator system is controlled mainly by varying the current supply to the MR fluid damper, which will in turn alter the Coulomb friction behaviour for the damper. The function of the MR damper is more like a force clutch.

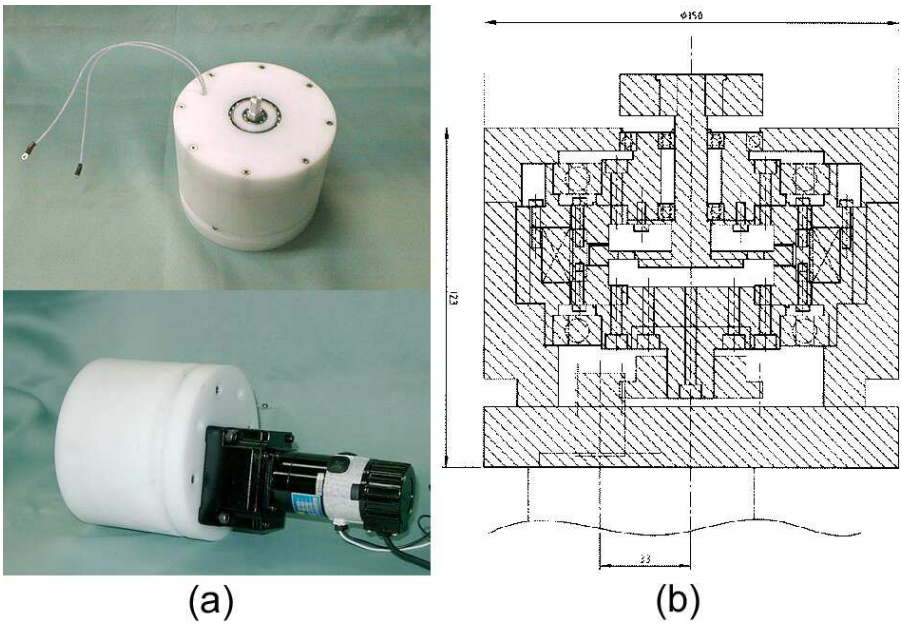

Figure 2.5: A MR actuator, MRA2, developed by Furusho's group. (a) Pictures of MRA2. (b) Section view of MRA2.

However, MR actuator has a similar topology with our proposed SDA system when a MR fluid damper is employed as the series damper. In this context, clarifying the differences between our SDA system and Professor Furusho's MR actuator system is necessary to validate our contributions. Although our actuator system based on the MR damper has a similar physical structure as the MR damper actuator proposed by Professor Furusho, the approach adopted by our system for force control is different from theirs. The main difference is that the latter assumes that the output force is not dependent on the input/output relative velocity of the damper. The drive unit (motor) mainly acts as a velocity source to one end of the MR damper. The output force of their actuator system is controlled mainly by varying the current supply to the MR fluid damper, which will in turn alter the Coulomb friction behaviour for the damper. The function of the MR damper is more like a force clutch. For our SDA system, the target damper is desirable to be of viscous type whose damping force is dependent on the damper's input/output relative velocity. If we know the constitutive property of the damper, the output force can be indirectly controlled by controlling the damper's input/output relative velocity. That is, the damper is acting like a force sensor. The MR damper in our actuator system is mainly used

to emulate a viscous damper. In fact, the system can use a broad range of dampers, such as linear or nonlinear viscous damper, MR fluid damper, ER fluid damper, or other types of dampers, as long as their force output can be made to be a function of the input/output relative velocity (either by virtue of their designs or by software control).

Besides those force control actuators, there are a lot of work on other types of actuators with force control, such as hydraulic actuators, pneumatic actuators, Piezoelectric actuators, shape memory alloy actuators, and so on (Grant, 2000; Ben-Dov, 1995; Niksefat, 2001; Abidi, 2004).

2.3 Summary

In this chapter, the necessary background about force control force control actuators have been given in detail. Several different force control actuator solutions has been introduced and discussed.

The SEA has good force fidelity, low output impedance, tolerance to shock loading and robust to changing loads. However, the introduction of an elastic component increases the compliance of the system and consequently, reduces the bandwidth of the system. Furthermore, due to the parameters trade-off, it is very hard to achieve good force fidelity at both low and high end range.

The proposed SDA system would have large bandwidth, high force fidelity at both high and low force ranges, low output impedance and high impact absorption ability. Another advantage of the SDA system is that the damping coefficient of the damper can easily be made variable by adopting an appropriate damper design, e.g. MR fluid damper. It will endow SDA with large force range and eased design trade-off.

Some other types of force control actuators, Micro-Macro actuators and MR fluid actuators, have also been introduced. The differences between SDA based on MR fluid damper with the existed MR actuators were also clarified to validate the originality and contribution of our work.

Chapter 3

Series Damper Actuator

In this chapter, we propose a novel force control actuator system, called "Series Damper Actuator" (SDA). Inspired by series elastic actuator (SEA), the proposed SDA system will be modelled and analyzed to show its properties by comparing with the SEA system. A simple PID controller is proposed for the general SDA model based on a linear series damper. Experimental setup is built and tested. Results are presented and discussed at the end of this chapter.

3.1 Force Control Actuators

3.1.1 Series Elastic Actuator (SEA)

Series elastic actuator(SEA) was proposed by MIT leg laboratory(Pratt, 1995-1; Williamson, 1995; Robinson, 1999, 2000-1). SEA uses springs in the series elastic component between the motor and the load. The output force can be indirectly controlled by controlling the deformation (measured by a sensor) of the springs, given the spring constants. Fig.3.1 shows a principle diagram of Series Elastic Actuator with a force feedback closed-loop system.

The sensor measures the deflection or strain in the spring which is a representation of the force, F, acting through the spring. By controlling this deflection, the

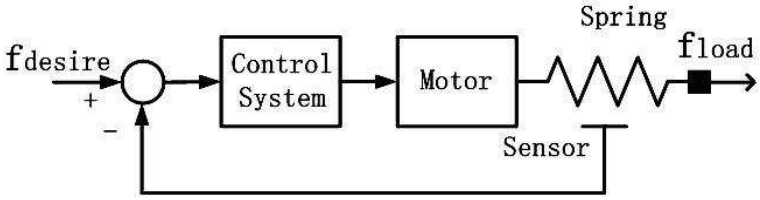

Figure 3.1: Schematic diagram of a Series Elastic Actuator

output force is essentially controlled according to Hooke's law:

$$F = kx$$

where k is the spring constant and x is the spring deflection.

The primary advantage of series elasticity is that the compliant load bearing sensor lowers the loop gain of the closed-loop system. The control gain can be proportionally increased to maintain the overall loop gain of the actuator at desired stability margins. This allows series elastic actuators to have low output impedance, be tolerant to shock loading and robust to changing loads. However, the introduction of the spring in the series elastic actuator system increases the compliance of system, and consequently the bandwidth of the system is reduced significantly (Steven, 1989). Furthermore, the selection of the spring stiffness for series elastic component is mainly governed by the trade-offs among the force bandwidth, force range and impact tolerance. Due to the fact that the spring stiffness is usually a constant (since it is difficult or of poor performance to achieve variable spring-stiffness design), it is very hard to achieve good force fidelity at both low and high end range.

3.1.2 Series Damper Actuator (SDA)

To solve these problems or ease the design tradeoffs, we propose a novel force control actuator system called "series damper actuator" (SDA) (Chew, 2004-1, 2004-2; Zhou, 2002). The SDA system consists of a control module and three hardware modules - a motor, a gear transmission and a damper, connected in series in the same order. A theoretical block diagram of Series Damper Actuator is shown in

Fig.3.2. The system is in fact designed to effectively control the relative velocity in the damper to achieve the desired the force with an already known damping coefficient. The controlled output force can be known from the following damping force equation:

$$F = bv$$

where the b is damping coefficient and v is the relative velocity in the damper

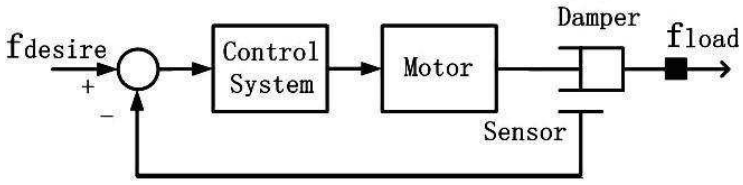

Figure 3.2: Schematic diagram of Series Damper Actuator

Compared with SEA system, SDA uses a damping component instead of a spring component and, consequently, reduces the system order by one. The SDA possesses a larger bandwidth than the SEA. Another advantage of the SDA is that the damping coefficient of the damper can easily be made variable by adopting an appropriate damper design. For example, one possible design is to adopt Magneto-rheological (MR) fluid, which has variable viscosity. The damping coefficient can become a controlled variable, which can be adjusted according to the environment conditions. For example, at high force and low force range, the damping coefficient would be increased and reduced respectively to allow a proper corresponding relative velocity in the damper. This endows the system higher force fidelity at both high and low force range. Furthermore, the series damper actuator has a distinctive advantage of outside impact absorption due to the damper energy dissipation characteristic. This characteristic is very important for walking robots, haptic devices or robot manipulators to protect them from damage when they are subjected to external unexpected impact.

However, before we design a SDA force control system, we need to give a detailed investigation on the force control properties of SDA to know the limitations of the system and the trade-offs among the design parameters. The following sections

study the characteristics of SDA by comparing the performance between SDA and SEA in term of system bandwidth, output impedance, impact tolerance and system efficiency. In the analysis, we assume the spring coefficient of SEA and damper coefficient of SDA are both constant.

3.2 General Models

3.2.1 Models of SEA

Ignoring the output inertia, the model and frequency domain diagram of Series Elastic Actuator can be shown as in Fig.3.3 (a) and (b). (Robinson, 1999; Williamson, 1995)

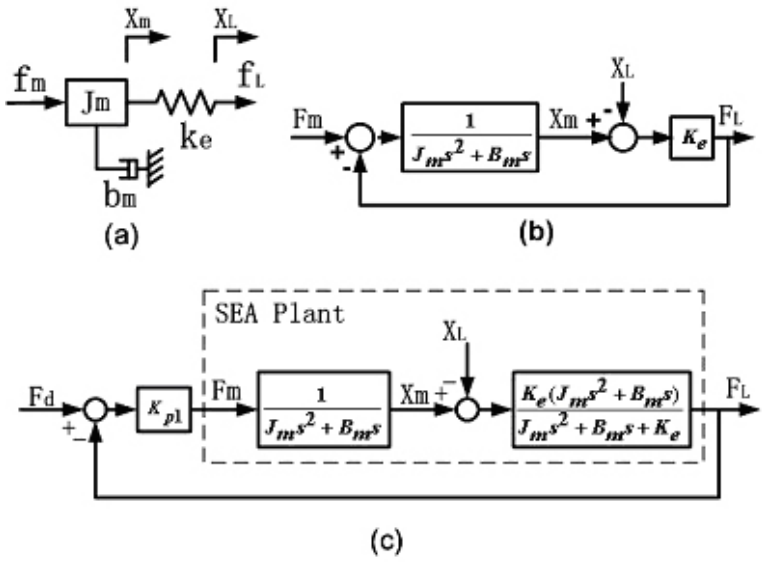

Figure 3.3: The SEA model (a), the block diagram of SEA plant (b), and the block diagram of the SEA control system with a unit feedback and a proportional controller (c)

From the SEA model diagram, we can write the following dynamics equations:

$$F_L = K_e * (X_m - X_L) \tag{3.1}$$

$$F_m - F_L = J_m \ddot{X}_m + B_m \dot{X}_m \tag{3.2}$$

where J_m is motor inertia;F_m is magnetic force applied on motor rotor; F_L is

output force of the actuator; X_m is motor position; X_L is load position; B_m is motor damping constant; K_e is spring constant;

Combining above two equations and taking Laplace Transform, we can solve the actuator output F_L as follows:

$$F_L(s) = \frac{K_e F_m(s) - K_e(J_m s^2 + B_m s)X_L(s)}{J_m s^2 + B_m s + K_e} \tag{3.3}$$

This is just the plant transfer function of SEA. To compare SEA with the SDA, we investigate those two kinds of plants both in a unit feedback closed-loop system and assume a proportional control law is used for the feedback controller. A simple control law can make the properties of the plants to be conspicuous.

Now, the block diagram for SEA can be shown as Fig.3.3(c). According to the block diagram, we can write the closed loop transfer function of the SEA as follows:

$$F_L(s) = \frac{K_{p1} K_e F_d(s) - K_e(J_m s^2 + B_m s)X_L(s)}{J_m s^2 + B_m s + K_e(K_{p1} + 1)} \tag{3.4}$$

where F_d is Desired force and K_{p1} is proportional controller gain.

3.2.2 Models of SDA

This subsection provides the model for SDA. The model and frequency domain block diagram for SDA plant is shown as Fig.3.4(a) and (b).

According to the model, we can write the dynamics equations of the SDA plant:

$$F_L = K_b(V_m - V_L) \tag{3.5}$$

$$F_m - F_L = J_m \dot{V}_m + B_m V_m \tag{3.6}$$

where K_b is damper constant, V_m is motor rotor velocity and V_L is load velocity.

Combining above two equations and taking Laplace Transform, we get the plant

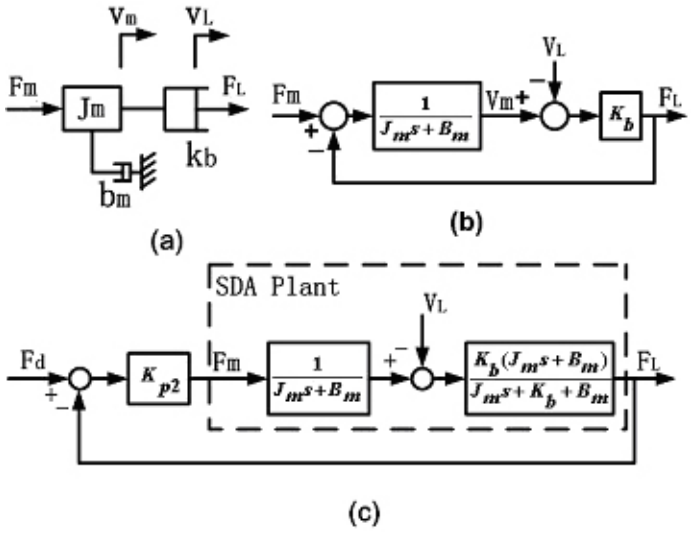

Figure 3.4: The SDA model (a), the block diagram of SDA plant (b), and the block diagram of SDA control system with a unit feedback and a proportional controller (c)

transfer function as follow

$$F_L(s) = \frac{K_b}{J_m s + B_m + K_b} F_m(s) - \frac{K_b(J_m s + B_m)}{J_m s + B_m + K_b} V_L(s) \tag{3.7}$$

Let's assume that the control law is also of proportional type. Then the closed loop system block diagram can be shown as in Fig. 3.4(c). According to the block diagram, we can write the following equation.

$$F_L(s) = \left\{ \frac{K_{p2}}{J_m s + B_m} [F_d(s) - F_L(s)] - V_L(s) \right\} \frac{K_b(J_m s + B_m)}{J_m s + B_m + K_b} \tag{3.8}$$

where $K_{p2}$is the proportional gain.

Solving the above equation for $F_L(s)$ gives the closed loop transfer function of the SDA:

$$F_L(s) = \frac{K_{p2} K_b F_d(s) - K_b(J_m s + B_m) V_L(s)}{J_m s + B_m + K_b(K_{p2} + 1)} \tag{3.9}$$

3.3 Property Analysis

3.3.1 System Bandwidth (Fixed End)

The system bandwidth is defined as the frequency at which the system frequency response (gain) has declined 3 db from its zero-frequency value (Richard, 1997).

- **SEA** This subsection assumes that the actuator output end is fixed. That is $X_L(s) = 0$. Therefore, the closed-loop transfer function can be written as

$$G_{cl}(s) = \frac{F_L(s)}{F_d(s)} = \frac{K_{p1}K_e}{J_m s^2 + B_m s + K_e(K_{p1}+1)} \tag{3.10}$$

By defining

controlled natural frequency as

$$\omega_{n1} = \sqrt{\frac{K - e(K_{p1}+1)}{J_m}} \tag{3.11}$$

and, equivalent damping factor as

$$\zeta_1 = \frac{B_m}{2\sqrt{J_m K_e(K_{p1}+1)}} \tag{3.12}$$

the closed-loop transfer function becomes:

$$G_{cl}(s) = \frac{F_L(s)}{F_d(s)} = K_1 \frac{\omega_{n1}^2}{s^2 + 2\zeta_1\omega_{n1}s + \omega_{n1}^2} \tag{3.13}$$

where

$$K_1 = \frac{K_{p1}}{K_{p1}+1} \tag{3.14}$$

We assume that the controller gain $K_{p1} >> 1$, then K_1 approximates to one. Then the closed-loop transfer function can be written that

$$G_{cl} = \frac{\omega_{n1}^2}{s^2 + 2\zeta_1\omega_{n1}s + \omega_{n1}^2} \tag{3.15}$$

From Equation 3.15, it is observed that SEA is a second order system. At low

frequencies, the transfer function approaches unity. As frequency increases, the actuator response begins to drop off, and in the limit, it goes to zero. With different equivalent damping factor, ζ_1, the system closed-loop bandwidth is varying around its natural frequency, ω_{n1}. So the value of ω_{n1} can reflect the bandwidth of the closed-loop system. According to Equation 3.11, it is easy to know that large proportional gain K_{p1} and spring constant K_e are desired to achieve high bandwidth.

Normalize Equation 3.15 with ω_{n1}, we can get:

$$G_{cl}(S) = \frac{1}{S^2 + 2\zeta_1 S + 1} \tag{3.16}$$

where $S = s/\omega_{n1}$, is a scaled complex variable.

It is obvious that the SEA system described by Equation 3.15 is an ideal second order system. Assuming that $\zeta_1 = 0.3$, we can get the frequency response plot of the SEA system and it is shown in Fig.3.5.

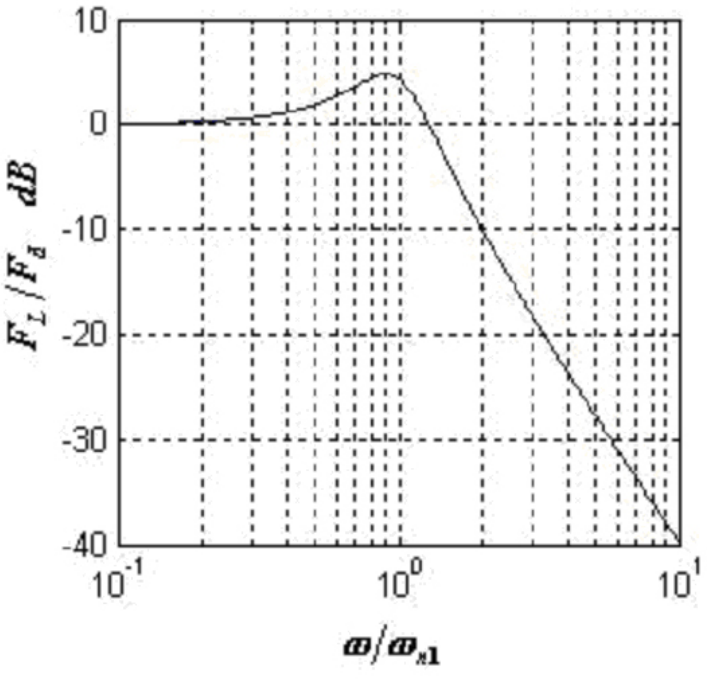

Figure 3.5: Fixed end bandwidth of the SEA system

- **SDA**

Let's assume that the actuator output end is fixed. That is, the load velocity $V_L(s)$ is zero in Equation 3.9. Then the closed-loop transfer function can be written as:

$$G_{cl} = \frac{F_L(s)}{F_d(s)} = \frac{K_{p2}K_b}{J_m s + B_m + K_b(K_{p2}+1)} \tag{3.17}$$

For simplicity, we assume that $B_m << K_b(K_{p2}+1)$. Then above equation can be written as

$$G_c l = \frac{K_{p2}K_b}{J_m s + K_b(K_p 2 + 1)} \tag{3.18}$$

By using the following definitions:

Controlled natural frequency

$$\omega_{n2} = \frac{K_b(K_{p2}+1)}{J_m} \tag{3.19}$$

we obtain

$$G_c l(s) = \frac{F_L(s)}{F_d(s)} = K_2 \frac{\omega_{n2}}{s + \omega_{n2}} \tag{3.20}$$

where

$$K_2 = \frac{K_{p2}}{K_{p2}+1} \tag{3.21}$$

Obviously, SDA is a first order system. Similar to the SEA, if the proportional controller gain K_{p2} is large enough (i.e.$K_{p2} >> 1$), K_2 approaches to unit and then ω_{n2} is just the SDA system closed-loop bandwidth. From Equation 3.19, we can know that the system bandwidth can be increased by increasing damper constant K_b and proportional gain K_{p2}. Assuming that$K_2 = 1$ and normalizing Equation 3.20 with ω_{n2} gives:

$$G_{cl}(S) = \frac{1}{S+1} \tag{3.22}$$

where S is a complex variable which is obtained by normalizing s with ω_{n2}.

The frequency response of the SDA system is shown in Fig.3.6.

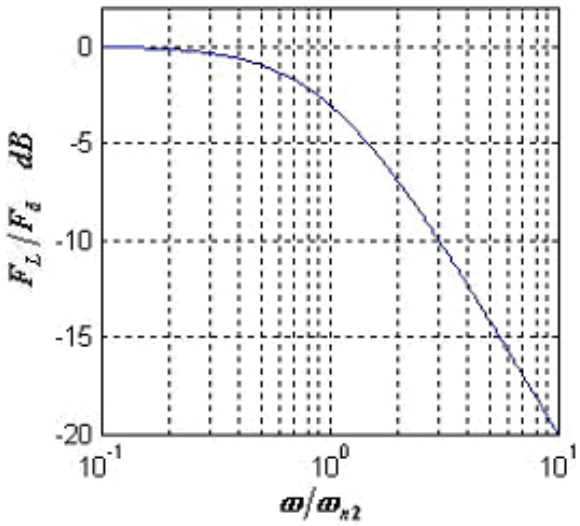

Figure 3.6: Fixed end bandwidth of the SDA system

3.3.2 Output Impedance (For Zero Force)

- **SEA** When the input, $F_d(s)$ is set to zero, the system dynamic function, Equation 3.4, can be written as:

$$F_L(s) = \frac{-K_e(J_m s^2 + B_m s)}{J_m s^2 + B_m s + K_e(K_{p1} + 1)} X_L(s) \tag{3.23}$$

The minus sign in the above equation represent the reversed direction of the generated force. For convenience, we adjust the definition of the output impedance as:

$$Z(s) = -\frac{F_L(s)}{X_L(s)} \tag{3.24}$$

Then we can get

$$Z(s) = \frac{K_e(J_m s^2 + B_m s)}{J_m s^2 + B_m s + K_e(K_{p1} + 1)} = K_e \frac{s^2 + 2\zeta_1 \omega_{n1} s}{s^2 + 2\zeta_1 \omega_{n1} s + \omega_{n1}^2} \tag{3.25}$$

From Equation 3.23, we see that the impedance at low frequency approaches zero. At high frequency (when $\omega > \omega_{n1}$), it approaches K_e, the elastic constant of the physical spring. It can be seen that reducing spring constant K_e can reduce the output impedance.

Normalizing Equation 3.25 gives:

$$Z'(S) = \frac{Z(S)}{K_e} = \frac{S^2 + 2\zeta_1 S}{S^2 + 2\zeta_1 S + 1} \tag{3.26}$$

where

$$S = \frac{s}{\omega_{n1}} \tag{3.27}$$

Taking $\zeta_1 = 0.3$, the output impedance is plotted against the frequency as shown in Fig.3.7.

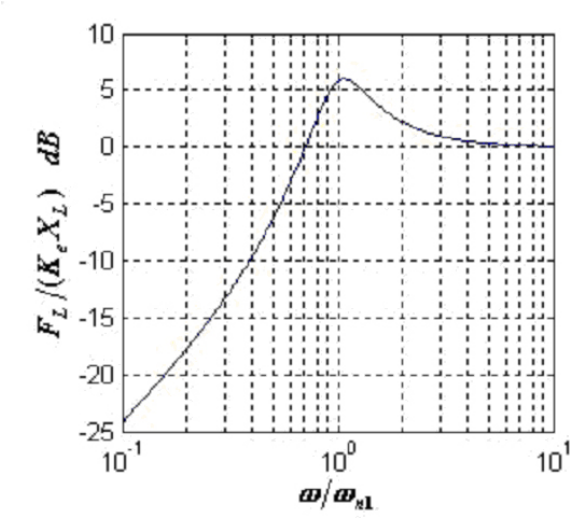

Figure 3.7: The output impedance of the SEA system

- **SDA**

When the input $F_d(s)$ is zero, the SDA transfer function, Equation 3.9, relating the load force to the load velocity can be written as:

$$D(s) = -\frac{F(s)}{V_L(s)} = \frac{K_b(J_m s + B_m)}{J_m s + K_b(K_{p2} + 1) + B_m} \tag{3.28}$$

Assuming $B_m << K_b(K_{p2} + 1)$ gives that

$$D(s) = K_b \frac{s}{s + \omega_{n2}} \tag{3.29}$$

where

$$S = \frac{s}{\omega_{n2}}$$

Equation 3.29 can be viewed as system output damping with zero force command. It can be shown that the output damping at low frequency is ideally equal to zero and increases with the increasing of frequency. At high frequency ($\omega > \omega_{n2}$), it would approach to K_b, the damping constant. This property is very similar to the output impedance of SEA.

To make a comparison, we also calculate the output impedance of the closed loop SDA system with zero force command. It is easy to obtain from Equation 3.29 that

$$Z(s) = -\frac{F_L}{X_L} = s * D(s) = K_b \frac{s^2}{s + \omega_{n2}} \tag{3.30}$$

Rewrite the above equation as follow

$$Z'(s) = -\frac{F_L}{X_L K_b} = \frac{s^2}{s + \omega_{n2}} \tag{3.31}$$

The frequency response of the output impedance of the SDA system is shown in Fig.3.8. Different from SEA, the output impedance of SDA goes infinite when frequency increases continuously. But at low frequency, the output impedance of the SDA is still ideally low. According to Equation 3.30, decreasing damper constant K_b can effectively reduce the system output impedance $Z(s)$.

3.3.3 System Efficiency

- **SEA**

  The system efficiency is defined as the ratio of system output power to the system input power. If the subsystems are connected in series, the system efficiency can be computed by taking the product of the efficiencies of the subsystems. For example, the overall system efficiency (η) of SEA can be obtained by taking the product of the efficiency of the motor, η_m and the

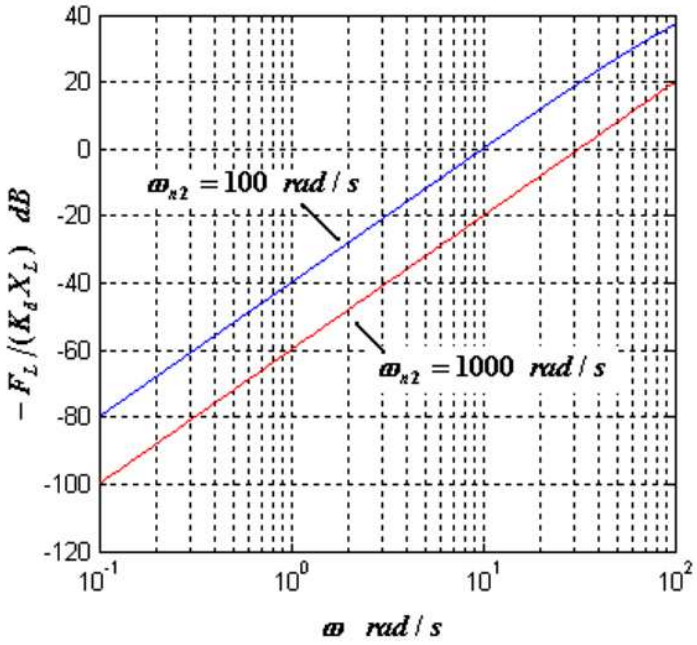

Figure 3.8: The output impedance for $\omega_{n2} = 100rad/s$ and $\omega_{n2} = 1000rad/s$ of the SDA system.

efficiency of the series elastic component, η_s:

$$\eta = \eta_m * \eta_s \tag{3.32}$$

If series elastic component consists of only ideal springs, it is 100% efficient, that is $\eta_s = 1$. So the total system efficiency equals to the efficiency of the motor:

$$\eta = \eta_m \tag{3.33}$$

- **SDA**

  In SDA, the series component is the damper. Neglecting damper inertia force, the constitutive equations of the damper (assuming viscous type) are given as follows:

$$F = K_b(V_m - V_L) = K_b \Delta V \tag{3.34}$$

$$F = F_L \tag{3.35}$$

where F is the output force of the damper and ΔV is the difference between

V_m and V_L.

The power dissipated in the damper is

$$\Delta P = F\Delta V = \frac{F_L^2}{K_b} \tag{3.36}$$

Equation 3.36 gives a limitation to chose the damper constant K_b, if there is a upper boundary of the dissipation power ΔP defined. Considering that there should be a range for the output force F_L, then a low limitation for the value of damper constant K_b is given by the following equation:

$$K_b \geq \frac{F_{max}^2}{\Delta P_{max}} \tag{3.37}$$

where F_{max} is the maximum output force and ΔP_{max} is the upper boundary of dissipation power allowed.

The efficiency of damper is

$$\eta_d = \frac{P_L}{P_m} = \frac{FV_L}{FV_m} = \frac{V_L}{V_m} \tag{3.38}$$

where P_L is the output power of the damper and P_m is the output power of the motor.

The possible relationships between V_L and V_m are as follows:

1. $\frac{V_L}{V_m} > 1$
2. $\frac{V_L}{V_m} = 1$
3. $\frac{V_L}{V_m} < 0$
4. $0 \leq \frac{V_L}{V_m} < 1$

From Equation 3.34 and Equation 3.38, we know that, for both Case 1 and Case 3, the damper output power is less than zero, that is, $P_L < 0$. This means that the SDA system do negative work on the load. In other words, the energy is actually transmitted from the load to the system. When $V_L = V_m$ (Case 2), the damper output force F would be zero and there is no power output from

the motor, that is, $P_L = P_m = 0$. We will not discuss the system efficiency for these three cases considering that we only concern efficiency problem when the system does active work. Then we only discuss the system efficiency for the Case 4. This is the expected working state for the system, in which the motor runs actively and the energy is transmitted form the motor to the load through the damper. A detail view on the system efficiency should be given.

Combining Equation 3.36 and Equation 3.38 gives

$$\eta_d = \frac{P_L}{P_m} = \frac{V_L}{V_L + \Delta V} = \frac{K_b V_L}{F_L + K_b V_L} \tag{3.39}$$

So the overall system efficiency, η, equals to the product of the efficiency of motor (η_m) and the efficiency of the damper (η_d).

$$\eta = \eta_m \eta_d = \eta_m \left(\frac{K_b V_L}{F_L + K_b V_L} \right) \tag{3.40}$$

Here,we only care about the damper efficiency. According to Equation 3.39, when the motor works with low output force and high output velocity, then the system achieves a high efficiency. Contrarily, the system efficiency is low with high load force and low load output velocity. It can be noted that the system efficiency will increase when the damping coefficient K_b increases. When the K_b goes infinity, the efficiency of the damper η_d approaches to 1. It is easy to understand that, in such occasion ($K_b \to \infty$), the damper actually acts as a rigid connector between the motor and load.

3.3.4 Impact Tolerance

- **SEA**

  For the impact tolerance character, we are concerned with the interaction energy transferred to the actuator from the environment. We assume that the environment dictates s a sudden load motion V_L. The impact power, P_L, from

the load is defined by the load force and load velocity at the system output:

$$P_L = F_L V_L \tag{3.41}$$

Substituting $X_L = \frac{V_L}{s}$ into Equation 3.23 gives

$$F_L(s) = \frac{-K_e(J_m s + B_m)}{J_m s^2 + B_m s + K_e(K_{p1} + 1)} V_L(s) \tag{3.42}$$

Combining Equations 3.41 and 3.42 gives the controlled impact power

$$P_L(s) = -V_L^2 K_e \frac{J_m s + B_m}{J_m s^2 + B_m s + K_e(Kp1 + 1)} = -V_L^2 K_e \frac{s + 2\omega_{n1}\zeta_1}{s^2 + 2\omega_{n1}\zeta_1 s + \omega_{n1}^2} \tag{3.43}$$

The minus sign in Equation 3.43 represents the energy flow direction and means that the energy is transmitted form the outside to the actuator. Since the spring will ideally not dissipate any energy, the impact power P_L generated on the spring output end will be totally transmitted to the other end, which is connected with the actuator. Following Equation 3.43, it can be stated that, to achieve high impact tolerance, small value of spring constant K_e is desirable.

- **SDA**

  Neglecting the minus in Equation 3.28 and combining Equations 3.41 and 3.28 gives the controlled impact power P_L

$$P_L(s) = V_L^2 K_b \frac{J_m s + B_m}{J_m s + K_b(K_{p2} + 1)B_m} = V_L^2 K_b \left(\frac{s + \sigma\omega_{n2}}{s + \omega_{n2}} \right) \tag{3.44}$$

  where

$$\sigma = \frac{B_m}{K_b(K_{p2} + 1)} \tag{3.45}$$

  Equation 3.44 is the power generated by the given impact velocity V_L at the output end of the damp. In fact, we are concerned about the power transmitted to the motor, P_{cp}:

$$P_{cp} = P_L(s) - \Delta P(s) \tag{3.46}$$

Combining Equations 3.28,3.36 and 3.46 gives:

$$P_{cp} = P_L(s) - \Delta P(s) = V_L^2 K_b \left[\frac{s + \sigma\omega_{n2}}{s + \omega_{n2}} - (\frac{s + \sigma\omega_{n2}}{s + \omega_{n2}})^2 \right]$$

$$= V_L^2 K_b \left[\frac{(s + \sigma\omega_{n2})(1 - \sigma)\omega_{n2}}{(s + \omega_{n2})^2} \right] \tag{3.47}$$

Define

$$G_{cp}(s) = \frac{(s + \sigma\omega_{n2})(1 - \sigma)\omega_{n2}}{(s + \omega_{n2})^2} \tag{3.48}$$

Neglecting σ and normalizing above equation with ω_{n2} gives

$$G_{cp}(S) = \frac{S}{(S + 1)^2} \tag{3.49}$$

Then we can get

$$P_{cp}(s) = V_L^2 K_b G_{cp}(S) = V_L^2 K_b \frac{S}{(S + 1)^2} \tag{3.50}$$

A plot of the frequency response of $G_{cp}(S)$ is shown in Figure 3.9. We note that, both at low and high frequency, P_{cp} is near to zero or very small, which means the damp absorbs almost all the impact power. At the controlled natural frequency ω_{n2}, P_{cp} reaches its maximum value. Following Equation 3.50, it is easy to know that the power P_{cp} is proportional to the damping coefficient K_e when the controlled natural frequency ω_{n2} has a fixed value. Therefore, the impact power transmitted to the motor can be effectively reduced by decreasing K_e.

3.4 Comparison and Discussion

This section presents the comparison between SEA and SDA. From the analysis, the advantages and disadvantages of SDA will be highlighted.

Bandwidths of those two systems are very different. According to Equations 3.11 and 3.19, the bandwidth of SDA would be larger than that of SEA provided

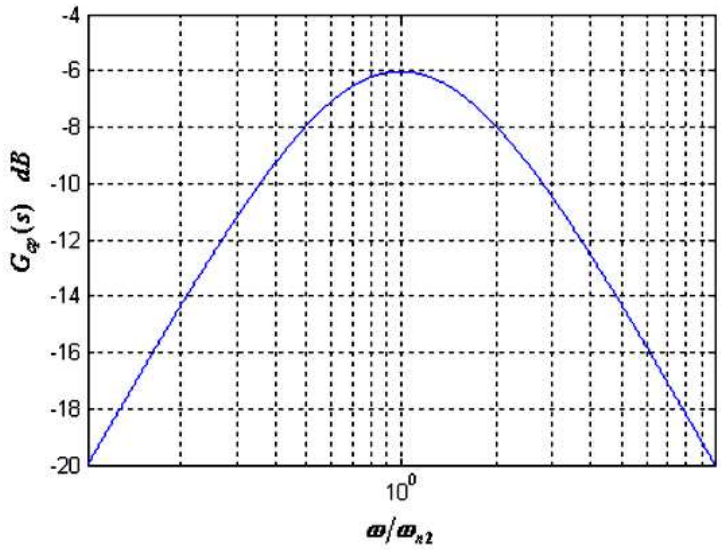

Figure 3.9: The frequency response of $G_{cp}(S)$.

the parameters for the two systems have similar design values. This conclusion also can be corroborated by the fact that SDA is a fist order system while the SEA system is second order. From the perspective of control engineering, the low order system is preferred for its better control qualities than the higher order system. For both systems, increasing the coefficients of the series components, K_e and K_b, and proportional control gains, K_{p1} and K_{p2}, can increase their bandwidths. However, we can not choose those parameters arbitrarily because of the problems like system trade-offs and hardware limitations. In fact, the bandwidth of a real SEA system is fairly low (Robinson, 1999; Zinn, 2002-1).

The **output impedance (at zero load)** of the two systems ideally approach zero at low frequency (Fig.3.7 and Fig.3.8). As the frequency increases, the output impedance of SEA converges to its spring constant K_e. However, the output impedance of SDA will go to infinity with the increasing of frequency. This means the SDA output end would be highly stiff for a high frequency impact. But at low frequency range, the output impedance of SDA is almost to be zero. Increasing the proportional gains,K_{p1} and K_{p2}, and reducing the series component constants, K_e and K_b, can reduce the output impedance for SEA and SDA respectively.

The **impact tolerance** property gives the actuators protection when the systems

are subjected to external impact. The impact tolerance ability of SEA and SDA can be increased effectively by decreasing the spring constant K_e and damper constant K_b respectively. Increasing the proportional controller gains, K_{p1} and K_{p2}, also can reduce the impact power, but this effect is secondary. In the SDA system, because of the power dissipation of the damper, the impact power transmitted to the motor is less than the power generated on the damper output end.

System efficiency is an important problem of the SDA system because of the power dissipation character of the damper. According to Equation 3.39, when the actuator is running with high output force and low output velocity, the system needs a high damping constant to maintain a certain efficiency. It is important to note that the system efficiency is decided not only by damper constant K_b and load force F_L, but also by load velocity V_L that is not under control. In other words, we could not guarantee a certain system efficiency under any condition and for all the time. Therefore, to decide the value of damper constant K_b, the criterion is to achieve a satisfactory average system efficiency in a certain time range. It should be noted here that if the damper constant K_b satisfies the Equation 3.37, the damper dissipation power ΔP is always within a permitted range, no matter what the system efficiency is. Obviously, from the view point of system efficiency, the larger damping constant the better. While in SEA system, the introduction of spring, ideally, has no influence on the system total efficiency.

It is important to mention here that the exact system characteristics are surely related to the specific design of the system controller. Dedicated controllers can give each of the systems a much better overall performance. Here we use a proportion control law just to highlight a few control characteristics of these two systems.

3.5 A General Controller for SDA

When we analyze the SDA system in previous sections, we assume a simple proportional controller so that some fundamental properties of the system can be clearly illustrated. To achieve a better force control performance, a PID control scheme is

used to control the SDA as shown below in Fig.3.10. Furthermore, two feedforward blocks based on the inverse dynamics model are employed for the reference force and load velocity, respectively. They are intended to improve the system transient response and reduce the effect of the load movement on the output force.

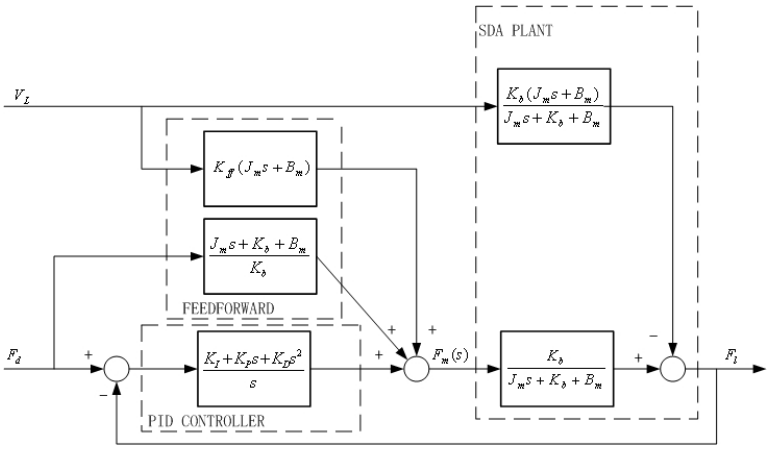

Figure 3.10: A general control scheme for series damper actuator system.

To achieve varying damping coefficient, we use a Magneto-Rheological (MR) fluid damper (rotary type) as the series damper component. Based on the Bingham viscoplastic model, the dynamics equation of MR damper can be represented as:

$$F = K_d\omega + [T_f + T(B)] \cdot sign(\omega) \tag{3.51}$$

where F is the overall torque; K_d is the damping coefficient when no field is applied; ω is relative angular velocity of the MR damper; T_f is frictional torque; $T(B)$ is the variable torque which is a function of the magnetic flux density B.

The problem with the MR damper is that it does not behave like a linear viscous damper when B is constant. To emulate a linear viscous damper (desirable for the SDA system), a special linearization algorithm is applied to the MR damper. Furthermore, the linearization algorithm can vary the damping coefficient according to the working conditions.

Assuming that $T_f << T(B)$ and $T(B)$ has a linear relationship with the absolute value of the input current for the MR damper, that is, $T(B) = K_a \cdot |I(t)|$, Eq.3.51

can be rewritten as:

$$F = K_d\omega + K_a \cdot |I(t)| \cdot sign(\omega) \tag{3.52}$$

where K_a is a constant whose value depends on the inherent property of the MR fluid damper. Applying following linearization algorithm:

$$I(t) = K_c\omega(t) \tag{3.53}$$

Eq.3.52 becomes:

$$F = K_d\omega(t) + K_aK_c\omega(t) = K_b\omega(t) \tag{3.54}$$

where K_c is the linearization algorithm constant, and

$$K_b = K_d + K_aK_c \tag{3.55}$$

When the linearization algorithm is executed, the MR damper behaves like a linear viscous type damper with F proportional to ω, and K_b is the effective damping coefficient. From Eq.3.55, since K_a and K_d are constants, the damping coefficient K_b of the series damper can modified by changing the value of K_c.

The main difference between SDA based force control implementation and the existing MR damper based force control implementation is that the latter assumes that the output force is not dependent on the input/output relative velocity of the damper. The drive unit is mainly used to supply a velocity source to one end of the MR fluid damper. The output force is only controlled by the current supply to the MR fluid damper.

For the SDA system, the force control is achieved by controlling the damper's input/output relative velocity. It can use a broad range of dampers, such as linear or nonlinear viscous damper, MR fluid damper, ER fluid damper or other types of dampers as long as their force output can be a function of the input/output relative velocity (either by virtue of their design or by software control).

From the calculation and analysis, we can see that the SDA system has similar characteristics to SEA system on bandwidth and impact tolerance. For both systems, there are trade-offs among system bandwidth, output impedance and impact tolerance when selecting the series component constants K_e and K_b for SEA and SDA, respectively. These two constants have similar influences on system characteristics.

In the design of SDA system, the damper constant K_b should be kept to a relative low range to achieve desired low output impedance and high impact tolerance, but, at the same time, the damper constant should still be large enough to give the system satisfactory bandwidth and efficiency. Choosing the damper constant to balance those trade-offs is just an optimal design process.

The main advantage of SDA is that the series damper has a linear response to motor velocity, rather than motor displacement as a spring does in the SEA system. The bandwidth of SDA is expected to be better than that of SEA and therefore the design trade-offs are eased. Furthermore, it is much easier to achieve variable damping coefficient than that of variable spring constant. For example, magneto-rheological fluid can be used for the damping component so that it has controllable damping coefficient. With such a feature, SDA can meet different system specifications such as high bandwidth and low output impedance in a broad output range.

3.6 Experimental Setup and Results

An experimental setup of the MR fluid damper based Series Damper Actuator (SDA) and its schematic diagram are shown in Fig.3.11 and Fig.3.12, respectively. In this experimental system, two angular encoders are used to obtain the series damper input angular velocity and output angular velocity, respectively. The relative angular velocity in the series damper, $\omega(t)$, is calculated from the difference between the two angular velocities.

The series damper component is a Magneto-Rheological Fluid damper (Lord

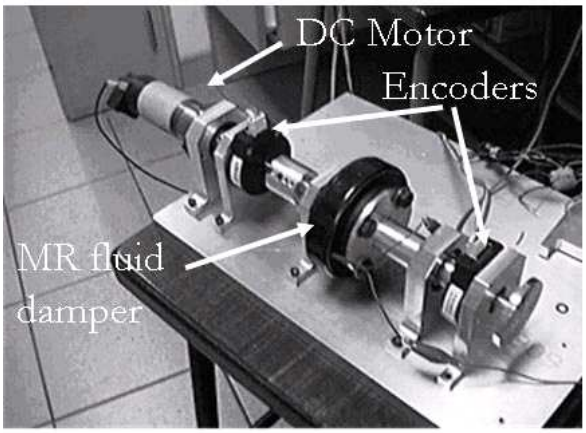

Figure 3.11: Photograph of the experimental Series Damper Actuator

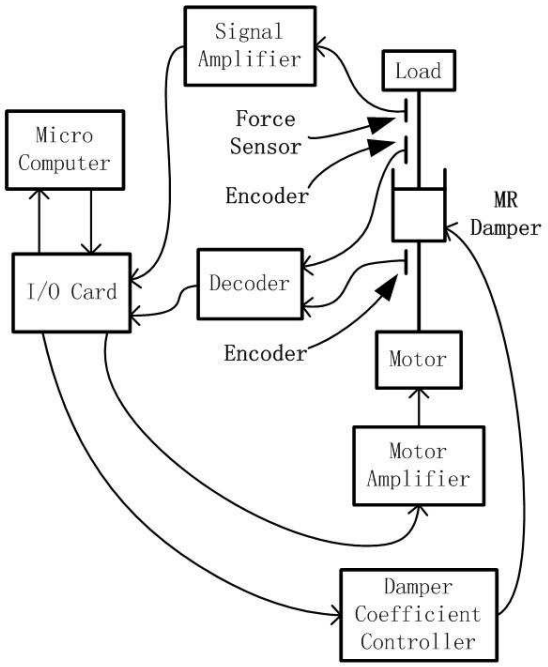

Figure 3.12: Schematic diagram of the experimental system

MRB-2107-3) which has a controllable damping coefficient as described in the previous section. A damping coefficient controller is used to control the damping coefficient of the series damper according to the damper's linearization law.

The main controller is implemented on a microcomputer system. It obtains the feedback signals from the two encoders and computes the motor drive signal according to the given control scheme so that the desired force can be achieved at the actuator output. To measure the actual system output torque, a torque sensor is mounted at the end of the actuator.

The results of the fixed end experiment are shown in Figs.3.13 to 3.16. Fig.3.13 and Fig.3.14 illustrate the system responses to sinusoidal and step references, respectively, when $K_b = 0.18Nms$. The results show that the experimental SDA system has no problem in achieving force control.

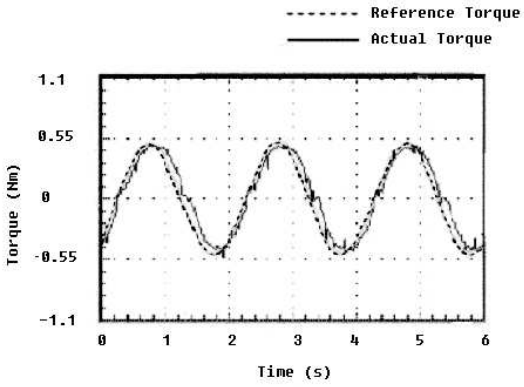

Figure 3.13: Force tracking following a sinusoidal reference when the damping constant $K_d = 0.18Nms$

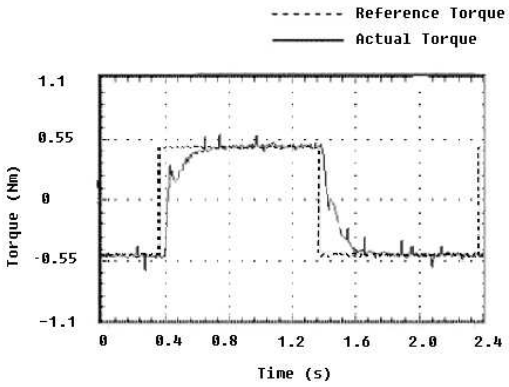

Figure 3.14: Force tracking following a step reference when the damping constant $K_d = 0.18Nms$

Variable damping coefficient is another advantage of the experimental SDA system. Fig.3.15 and Fig.3.16 shows the system responses for sinusoidal and step inputs, respectively, after the damping constant K_b has been doubled to $K_b = 0.36Nms$, while the amplitudes of the inputs were increased by four times.

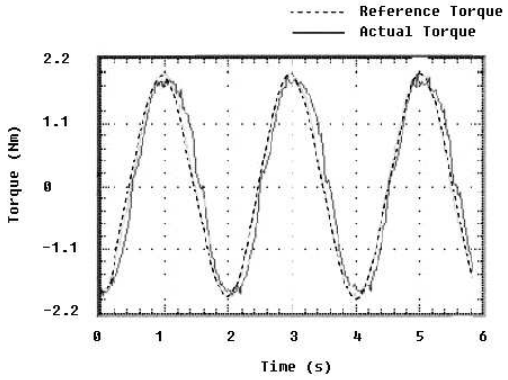

Figure 3.15: Force tracking following a sinusoidal reference when the damping constant $K_d = 0.36Nms$

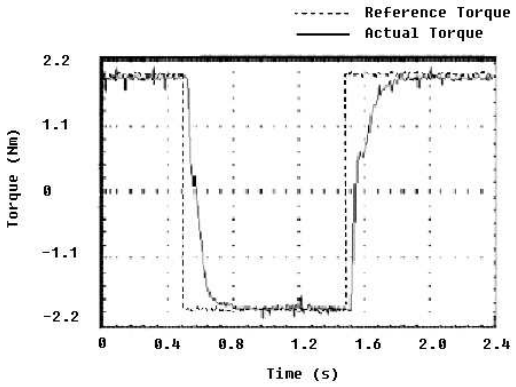

Figure 3.16: Force tracking following a step reference when the damping constant $K_d = 0.36Nms$

The results demonstrated that the experimental SDA system can maintain its force fidelity at different force ranges by varying the damping coefficient. For example, to achieve higher force output, the damping coefficient should be increased accordingly. This feature greatly eases the design trade-off encountered in the Series Elastic Actuator (SEA) system. In the SEA system, due to the fact that it is difficult to achieve variable series elastic component, one has to trade off between maximum force and bandwidth of the force control.

The experimental SDA system has a bandwidth of around 10 Hz (when the damp-

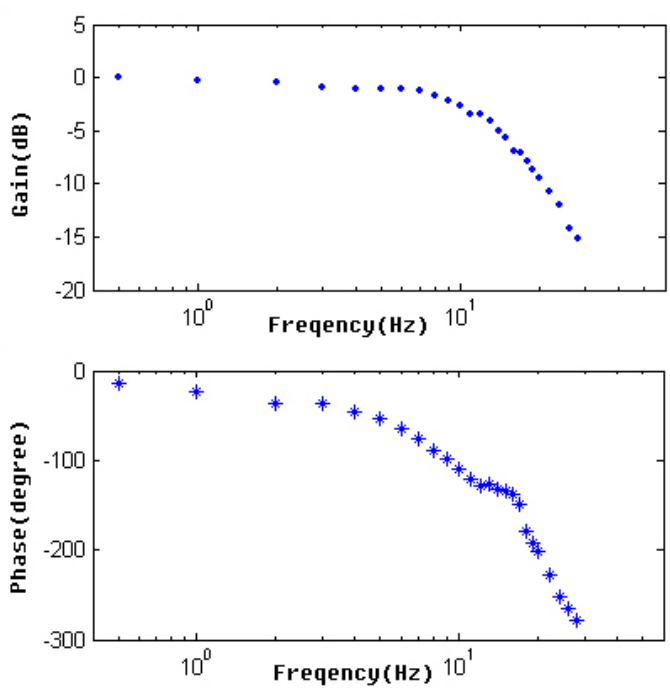

Figure 3.17: Frequency response of the experimental SDA system when the damping constant $K_d = 0.36Nms$

ing constant,$K_d = 0.36Nms$) as shown by the frequency response study (Fig.3.17). This is somewhat low compared to the theoretical analysis in previous sections. This problem is mainly contributed by the dynamics of the linearization algorithm which is applied to the MR fluid damper. The analysis of the SDA system is based on an ideal viscous damper whose force is proportional to the relative velocity between the input and output. In the physical experiment, the constitutive property of the MR damper is altered by the linearization algorithm so that it behaves like a linear viscous damper. However, the dynamics of the linearization effort which involves the dynamics of the electromagnetic and mechanical fluid domains is rather significant and it compromises on the bandwidth of the whole system. To achieve a better force bandwidth, we should compensate this extra dynamics in the controller or use a truly viscous damper to replace the MR fluid damper in the SDA system.

Some comments on this experimental SDA system should be given here. It is known from the analysis in previous section that the SDA system has shock absorption behavior which depends on the effective damping. If the effective damping

constant is high, the ability to absorb impact may be limited. However in this experiment, the MR fluid damper used has an inherent "fuse" torque which limits the torque transmission through it. This provides better impact resistance than the theoretical behavior.

In the experimental setup, we have adopted the digital encoder to indirectly measure the damper input and output velocities. From the two values, the relative velocity in the damper can be computed. Other types of velocity measurement devices can also be applied for SDA system, for example, tachometers, potentiometers, etc. If it is not necessary to measure both the input and output velocities of the damper, we can also have just one velocity sensor to directly measure the relative velocity of the damper.

The experimental results show a limited system bandwidth. It is suspected that it may be caused by the extra dynamics of the MR fluid damper, that has been neglected in the analysis by treating the MR fluid damper as linear viscous damper after linearization. Therefore, to clearly reveal the effect of this extra dynamics on SDA system properties, the SDA system will be analyzed, in the next chapter, with an assumption of higher oder dynamics for the series MR fluid damper to model this extra dynamics.

3.7 Summary

SDA system has been modelled and analyzed by comparing with the SEA system in terms of system bandwidth, output impedance, system efficiency, and impact tolerance ability. It was shown that the SDA system would have good force control fidelity, large bandwidth, low output impedance and high impact tolerance ability. Adopting variable damping coefficient, the SDA system can obtain broad output force range and ease the design trade-off.

Experimental setup has been built and MR fluid damper was employed as the series damper. A PID controller was proposed and variable damping coefficient was achieved with a damper linearization algorithm. Experimental results showed that

the SDA system has a high force control fidelity, low output impedance, large force range, and high impact tolerance ability.

Chapter 4

Series Damper Actuator Based on MR Fluid Damper

To achieve both good force fidelity and high compliance for walking robot actuator, a novel force control actuator called series damper actuator (SDA) was proposed in Chapter 3 and our previous work (Zhou, 2002; Chew, 2004-1). Property analysis has been conducted to show the characteristics of SDA actuator. The analysis was based on linear (Newtonian viscous type) damper, that is, the damping coefficient is a constant and therefore it does not increase the order of SDA system. Experimental results also showed that SDA actuator can give good force control performance and, at same time, has a low output impedance and large system bandwidth. However, some problems have also been observed, such as the phase delay of the system output and, therefore, the low system bandwidth. It was suspected that these problems may be caused by the extra dynamics of the MR fluid damper. This dynamics has been neglected, in our previous work presented in Chapter 2, by treating the damper as a perfect linear damper. Intending to solve those problem, we investigate, in this chapter, the effect of this extra dynamics of MR fluid damper on the SDA system performance in terms of system bandwidth and output impedance.

4.1 Introduction

A typical SDA system consists of, as shown in Fig.4.1, a control module and two hardware modules - a motor (with or without gear transmission) and a viscous damper. The system is designed to effectively control the relative velocity in the damper to achieve the desired the force given the damping coefficient. The controlled output force of SDA can be known from the following damping force equation:

$$F = F(V) \tag{4.1}$$

where the F is damper output force and V is the relative velocity in the damper.

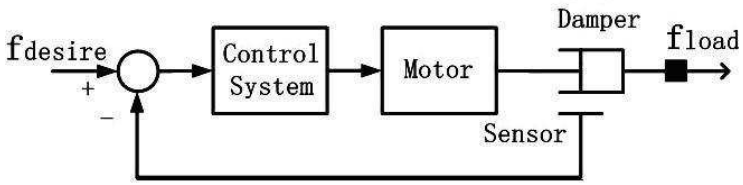

Figure 4.1: Schematic diagram of Series Damper Actuator

The damper output force F is a function of the damper relative velocity V . The damping coefficient K is the first derivative of the function F with respect to the relative velocity V, that is,

$$K = \frac{dF(V)}{dV} \tag{4.2}$$

The damping coefficient K can be either a constant or a function of relative velocity V. As long as the function is known a priori, SDA system output force F can be achieved by realizing the desired damper relative velocity V. If K is a constant, then the damper is called the Newtonian viscous (linear) damper.

Property analysis of SDA based on Newtonian viscous damper has shown that such a SDA system has relatively large bandwidth and low output impedance. If the damper can achieve varying damping coefficient, then the system can further obtain good force fidelity at both low and high output range.

To achieve varying damping constant and extend the capacity of the SDA actua-

tor, Magneto-Rheological (MR) fluid damper was proposed to be the series damper in SDA system. However, the employment of MR damper introduces high order dynamics into the SDA system. The effects of MR fluid damper dynamics on system properties, especially the bandwidth and output impedance, should be investigated before the design of the SDA system based on MR fluid damper.

The properties and control problems of MR fluid damper have been widely carried out in recent years (Carlson, 1996; Spencer, 1997; Dyke, 1997; Chiharu, 2003). In most cases, the MR fluid damper is used as a semi-active control devices in the field such as, seismic prevention and suspension system. They are not meant for force control. Some researchers have also proposed MR fluid damper actuator, in which the MR fluid damper works actively and output force is effectively controlled (Takesue, 2001, 2002, 2003; Kim, 2002). However, in those work, the dynamics of MR damper velocity has been neglected and the force control properties of such actuators are still unknown.

To reveal the effect of the dynamics of the MR fluid damper on the overall system, the fixed end bandwidth and output impedance for the series MR damper actuator (SMRDA) system and the series Newtonian viscous damper actuator (SNVDA) system are studied and compared.

In this chapter, the system properties, in terms of system bandwidth (fixed end) and system output impedance, is investigated for the SMRDA and compared with the SNVDA to show the effect of MR fluid dynamics on the SDA system bandwidth and output impedance. This chapter will provide important information for the design and control of the SDA system, especially the SMRDA system. In Section 4.3, the models of the SMRDA and the SNVDA are presented. System properties are analyzed and simulation results are given in Section 4.4. At the end of this chapter, the discussion and conclusion are made.

4.2 Magneto-Rheological (MR) Fluid Damper

4.3 System Model

4.3.1 Model of MR Fluid Damper

Numerous models for MR fluid damper have been proposed (Spencer, 1997). In this paper a simple Bingham visco-plastic model is employed for the SMRDA system model which is as shown in Fig.4.2(a). In this model the dynamics of the MR damper can be expressed as (Kim, 2002):

$$F = K_\eta V_d + F_\tau(I) * sign(V_d) \tag{4.3}$$

where F is the output torque/force of the MR damper; F_τ is the magnetic field dependent torque/force; I ($I > 0$) is the input damper current used to generate the magnetic field; K_η is the damping coefficient when no input current I is applied; and V_d is the damper velocity.

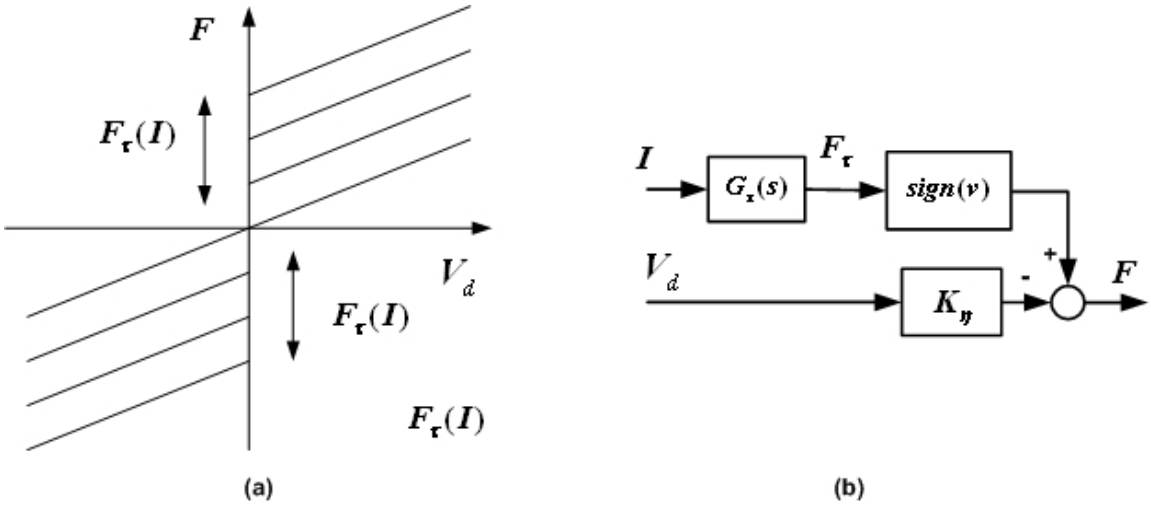

Figure 4.2: Bingham visco-plastic model of MR fluid damper. (a) Force F vs damper velocity Vd diagram;. (b) Damper model block diagram

The block diagram of this MR damper model is shown in Fig.4.2(b). This is a static model and valid only for applications which do not require fast response. Since fast response is desirable for the SDA system, the dynamics of the MR damper

has to be considered in the model. The dynamics of the MR damper is mainly due to the response of the magnetic field dependent torque/force F_τ with respect to the input current I. It is assumed to be a first order dynamics as given by the following transfer function (Takesue, 2001):

$$G_\tau(s) = \frac{F_\tau(I)}{I} = K_\tau \frac{\omega_\tau}{s + \omega_\tau} \tag{4.4}$$

where K_τ and ω_τ are constants, representing the gain and bandwidth of the dynamics, respectively.

4.3.2 Model of SMRDA System

SMRDA plant comprises of two components, viz.: an electrical motor and a MR fluid damper. The model of SMRDA plant is illustrated graphically in Fig.4.3, where F_m is the torque on the motor's rotor; J_m is the rotor inertia; V_m is motor rotor velocity, V_L is the load velocity and F_L is the load force (output force). The dynamics of the motor is mainly due to the rotor inertia J_m as shown in Fig.4.3(a). The block diagram of SMRDA plant is shown in Fig.4.3(b).

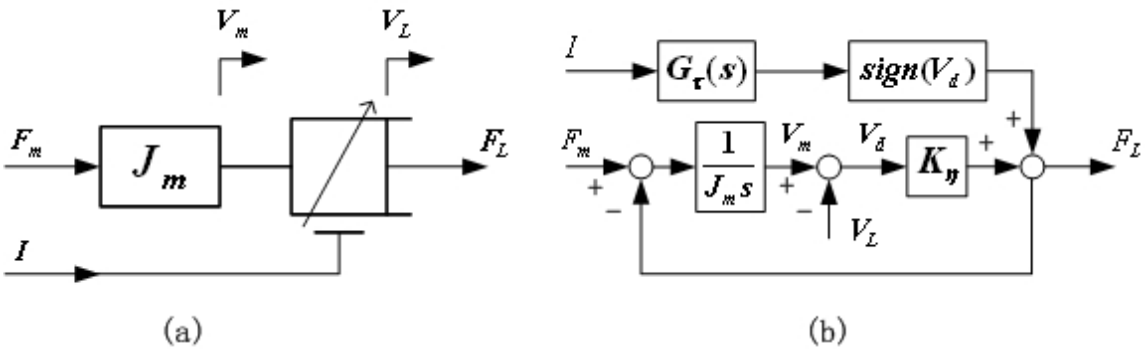

Figure 4.3: Series MR fluid damper actuator. (a) Schematic diagram of SMRDA structure. (b) SMRDA model block diagram

To achieve force control in the SDA system, the damper is desirable to have linear constitutive property, that is, the force/torque being proportional to the damper velocity V_d. This is achieved by using the following expression for I:

$$I = V_d \tag{4.5}$$

which yields

$$F = K_\eta V_d + G_\tau(s) V_d = (K_\eta + G_\tau) V_d \tag{4.6}$$

The resulting SDA plant is controlled by a proportional control law with unity feedback as shown in Fig.4.4. The reason for using the simple control law is to clearly illustrate the properties of the force control for the SDA system.

According to the above model, the transfer function of the SMRDA system is given as:

$$F_L = \frac{K_p(G_\tau + K_\eta)}{J_m s + (G_\tau + K_\eta)(K_p + 1)} F_R - \frac{J_m s(G_\tau + K_\eta)}{J_m s + (G_\tau + K_\eta)(K_p + 1)} V_L \tag{4.7}$$

Substituting Equation 4.4 into the transfer function of SMRDA, Equation 4.7 yields:

$$F_L = \frac{K_p K_\eta s + K_p \omega_\tau (K_\tau + K_\eta)}{J_m s^2 + (J_m \omega_\tau + K_\eta + K_p K_\eta) s + (K_p + 1)(K_\tau + K_\eta)\omega_\tau} F_R$$

$$- \frac{K_\eta J_m s^2 + J_m \omega_\tau (K_\tau + K_\eta) s}{J_m s^2 + (J_m \omega_\tau + K_\eta + K_p K_\eta) s + (K_p + 1)(K_\tau + K_\eta)\omega_\tau} V_L \tag{4.8}$$

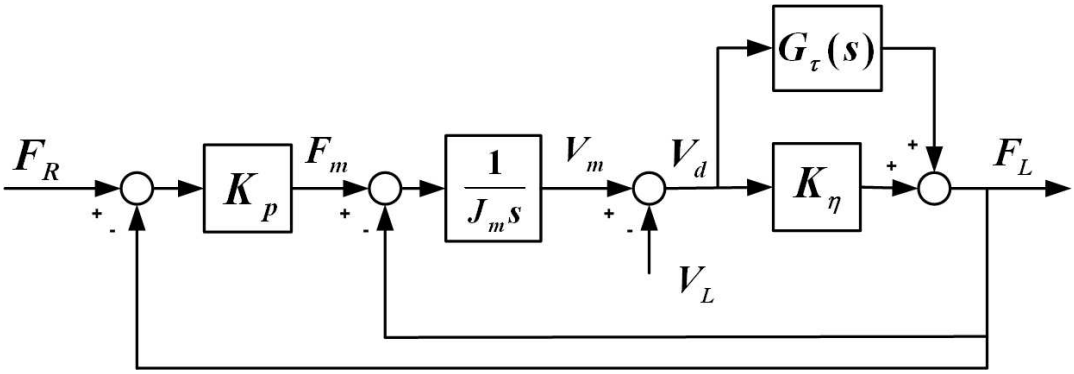

Figure 4.4: The block diagram of the SMRDA system with proportional controller and unity feedback

4.3.3 Model of SNVDA System

The model of the SNVDA system is as shown in Fig.4.5. It is different from the model of the SMRDA system in that there is no parallel component $G_\tau(s)$ for the damper dynamics. Therefore, the transfer function of SNVDA can be easily derived from that of the SMRDA system by taking $G_\tau(s)$ to be zero and substituting K_η

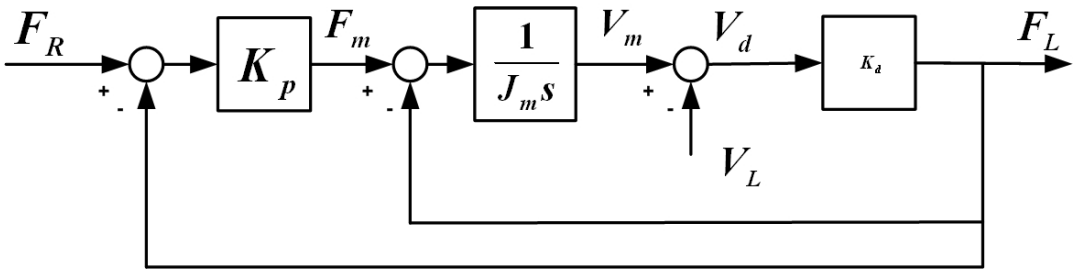

Figure 4.5: The block diagram of the SNVDA system with unit feedback and proportional controller

with K_d in Equation 4.7. The SNVDA system transfer function can be written as:

$$F_L = \frac{K_p K_d}{J_m s + K_d(K_p + 1)} F_R - \frac{K_d J_m s}{J_m s + K_d(K_p + 1)} V_L \tag{4.9}$$

4.4 Property Analysis

In this section, SMRDA was compared with SNVDA model in terms of the system bandwidth (fixed end) and the output impedance. The parameter values used for the simulations are listed in Table 4.1. To make these two systems comparable, we assumed that $K_\eta + K_\tau = K_d$. In the simulations, K_τ, K_η and ω_τ are varied to show their effects on the system properties.

Table 4.1: The parameter values used in the simulations

Parameter	Value	Units
J_m	0.02	kgm^2
K_p	18.5	–
K_d	0.385	Nms
K_τ	$0 \sim 0.385$	Nms
K_η	$0 \sim 0.385$	Nms
ω_τ	$10 \sim Inf.$	rad/s

4.4.1 System Bandwidth

- **Bandwidth of SNVDA System**

  According to Equation 4.9, the transfer function of SNVDA, when the output

end is fixed, can be written as:

$$\frac{F_L}{F_R} = \frac{K_p K_d}{J_m s + K_d(K_p + 1)} \tag{4.10}$$

That is, SNVDA can be described by a first order model. Note that, the introduction of the Newtonian viscous damper does not increase the order of the actuator system. Rewriting Equation 4.10 gives:

$$\frac{F_L}{F_R} = K' \frac{\omega_1}{s + \omega_1} \tag{4.11}$$

where

$$K' = \frac{K_p}{K_p + 1} \tag{4.12}$$

$$\omega_1 = \frac{K_d(K_p + 1)}{J_m} \tag{4.13}$$

For a first order system described by Equation 4.11, ω_1 is the bandwidth of this actuator system. The Bode magnitude plot of Equation 4.10 is shown in Fig.4.6.

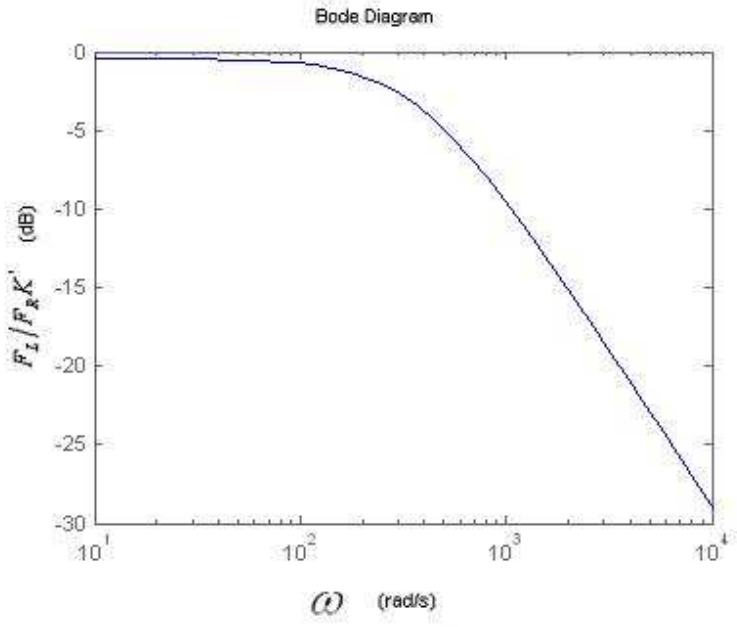

Figure 4.6: Bode magnitude response of the SNVDA actuator system

- **Bandwidth of SMRDA System**

According to Equation 4.8, the transfer function of SMRDA can be expressed as:

$$\frac{F_L}{F_R} = \frac{K_p K_\eta s + K_p \omega_\tau (K_\eta + K_\tau)}{J_m s^2 + (J_m \omega_\tau + K_p + K_p K_\eta) s + (K_\tau + K_\eta)(K_p + 1)\omega_\tau} \tag{4.14}$$

Note that the dynamics of the MR fluid damper increases the order of the actuator system. K_η and K_τ are the gains of Newtonian viscous component and field dependant component in the MR damper dynamics, respectively, as described in Equations 4.4 and 4.6.

To know their effects on the property of the SDA system, two extreme conditions are analyzed. The first is achieved by setting $K_\eta = K_d$ and $K_\tau = 0$. The other is achieved by setting $K_\eta = 0$ and $K_\tau = K_d$.

Case A: $K_\eta = K_d$ and $K_\tau = 0$

Under this condition, the Equation 4.14 can be further simplified as follows:

$$\frac{F_L}{F_R} = \frac{K_p K_\eta}{J_m s + K_\eta (K_p + 1)} \tag{4.15}$$

In this case, the transfer function is identical to that of SNVDA, Equation 4.10. So the bandwidth of SMRDA should be equal to Equation 4.13. This is because the MR fluid damper behaves like a Newtonian viscous damper when there is no magnetic field dependent component in Equation 4.3 (when $K_\tau = 0$).

Case B: $K_\eta = 0$ and $K_\tau = K_d$

In this case, Equation 4.14 can be modified as:

$$\frac{F_L}{F_R} = \frac{K_p K_\tau \omega_\tau}{J_m s^2 + J_m \omega_\tau s + K_\tau (K_p + 1)\omega_\tau} \tag{4.16}$$

The system transfer function is rewritten as follows:

$$\frac{F_L}{F_R} = K' \frac{\omega_2^2}{s^2 + 2\zeta\omega_2 s + \omega_2^2} \tag{4.17}$$

where

$$K' = \frac{K_p}{K_p + 1} \tag{4.18}$$

$$\omega_2 = \sqrt{\frac{K_\tau (K_p + 1)\omega_\tau}{J_m}} \tag{4.19}$$

$$\zeta = \frac{1}{2}\sqrt{\frac{J_m \omega_\tau}{K_\tau (K_p + 1)}} \tag{4.20}$$

In this case, the model is a typical second order system. Here, ω_2 and ζ are the natural frequency and the damping coefficient, respectively, of this system. The system bandwidth is dependant on both parameters. Now the effect of ω_τ on the system bandwidth is considered. It is easy to see, when $\omega_\tau \to 0$, the system bandwidth goes to zero. If $\omega_\tau \to \infty$, Equation 4.16 can rewritten as:

$$\frac{F_L}{F_R} = \frac{K_p K_\tau}{(J_m/\omega_\tau)s^2 + J_m s + K_\tau (K_p + 1)} \cong \frac{K_p K_\tau}{J_m s + K_\tau (K_p + 1)} \tag{4.21}$$

This transfer function equals to that of SNVDA. When ω_τ approaches infinity, the current input response dynamics of the MR damper, Equation 4.4, behaves like a zero order system with constant gain K_τ.

The Bode plot of the SMRDA system is shown in Fig.4.7. It is observed that the bandwidth of the SMRDA system increases with the increase of ω_τ when ω_τ is low. As ω_τ is large, the bandwidth of the SMRDA system approaches that of the SNVDA system as defined in Equation 4.13. If ω_τ is large enough, the high order dynamics introduced by the MR fluid damper into the SDA system can be neglected. However, the typical value of ω_τ for the MR damper is much lower than the bandwidth of the SNVDA system described by Equation 4.13. That is, the introduction of the MR damper in the SDA system will inevitably reduce the bandwidth of overall system.

The two cases discussed above are extreme conditions. Fig.4.8 shows the simulation results of the SMRDA systems with different proportions of Newtonian viscous component K_η and field dependant component K_τ, when $K_\tau + K_\eta \equiv K_d$ and $\omega_\tau = 20 rad/s$($20 rad/s$ is a typical value for the MR damper used). It is

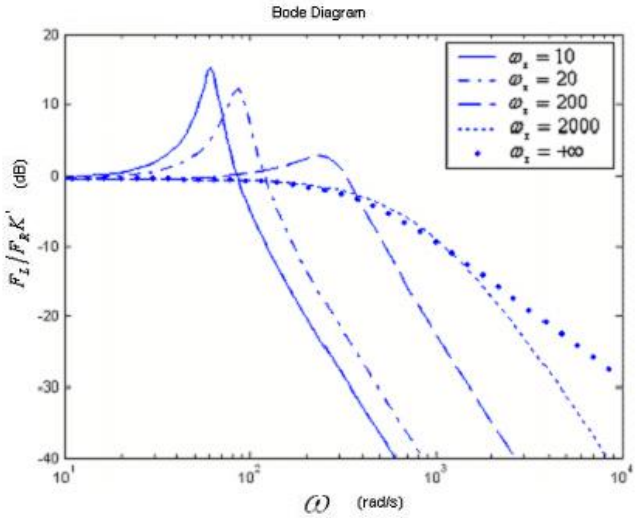

Figure 4.7: Bode magnitude plot of the SMRDA system with different value of ω_τ, when $K_\eta = 0$ and $K_\tau = K_d$

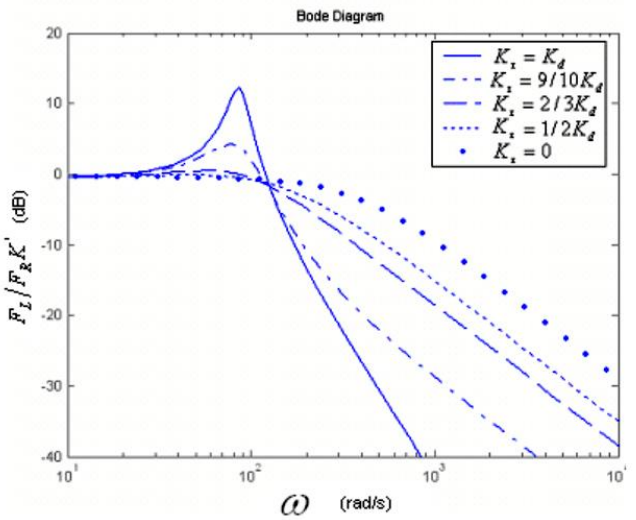

Figure 4.8: Bode magnitude plot of SMRDA system with different value of K_τ, when $\omega_\tau = 20rad/s$

shown that the transfer function and, therefore, the bandwidth of the physical SMRDA system is always between the first order system described by Equation 4.15 and the second order system described by Equation 4.16. If the ratio of K_τ over K_η increases, the system model approaches the second order system and the bandwidth reduces. On the contrary, if the ratio of K_τ over K_η decreases, the system model approaches the first order system and the bandwidth increases.

4.4.2 Output Impedance

The output impedance, sometimes also called the mechanical impedance, is defined as

$$Z(s) = \frac{F_e(s)}{V_L(s)} \tag{4.22}$$

where V_L represents the velocity at the load end, $F_e(s)$ ($F_e(s) = -F_L(s)$) represents the external force exerted on the output end of the actuator due to the load movement.

Low output impedance is a desirable property for the SDA system. In this section, the output impedances of the SNVDA system and the SMRDA system are analyzed to study the effect of the MR damper dynamics on this property.

- **Output Impedance of SNVDA System**

  From Equation 4.9, the output impedance of the SNVDA system is:

$$Z(s) = \frac{K_d J_m s}{J_m s + K_d(K_p + 1)} \tag{4.23}$$

  Normalizing the equation with the damping constant K_d, we have:

$$Z'(s) = \frac{F_e}{V_L K_d} = \frac{J_m s}{J_m s + K_d(K_p + 1)} = \frac{s}{s + \omega_1} \tag{4.24}$$

  The output impedance of SNVDA system is plotted against the frequency in Fig.4.9. It is observed that the output impedance at low frequency is ideally

low. When the frequency is higher than the SNVDA system's bandwidth ω_1, the output impedance approaches the damping constant K_d.

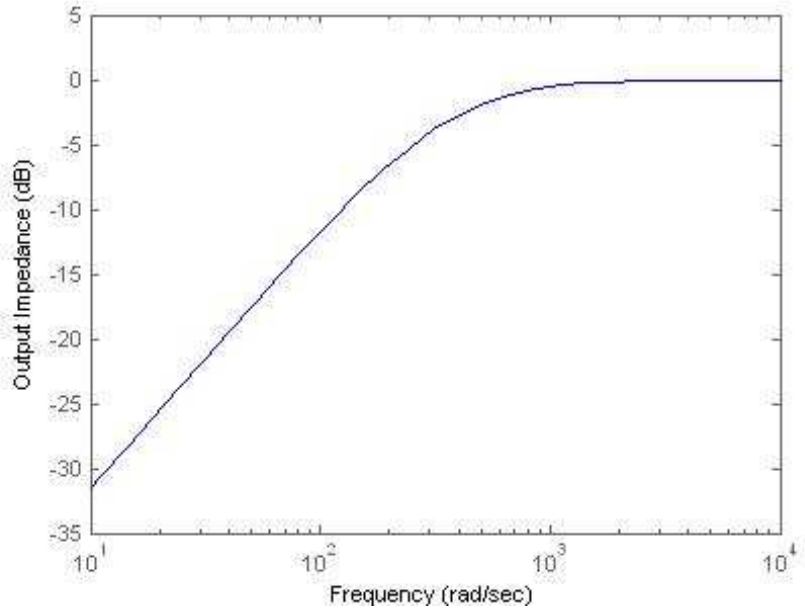

Figure 4.9: The output impedance of the SNVDA system

- **Output Impedance of SMRDA System**

From Equation 4.8, the output impedance of the SMRDA system is:

$$Z(s) = \frac{K_\eta J_m s^2 + J_m \omega_\tau (K_\tau + K_\eta) s}{J_m s^2 + (J_m \omega_\tau + K_\eta + K_p K_\eta) s + (K_p + 1)(K_\tau + K_\eta)\omega_\tau} \tag{4.25}$$

To compare with the SNVDA system, the output impedance equation is normalized with the damping coefficient $(K_\tau + K_\eta)$ as follows:

$$Z'(s) = \frac{F_e}{V_L(K_\tau + K_\eta)}$$

$$= \frac{\frac{K_\eta}{(K_\tau + K_\eta)} J_m s^2 + J_m \omega_\tau s}{J_m s^2 + (J_m \omega_\tau + K_\eta + K_p K_\eta) s + (K_p + 1)(K_\tau + K_\eta)\omega_\tau} \tag{4.26}$$

As in the previous subsection, two extreme cases are considered here: $K_\eta = K_d$, $K_\tau = 0$; and $K_\eta = 0$, $K_\tau = K_d$.

Case A: $K_\eta = K_d$ and $K_\tau = 0$

In this case, Equation 4.26 can be written as:

$$Z'(s) = \frac{J_m s}{J_m s + K_\eta(K_p + 1)} \tag{4.27}$$

The result function is identical to that of the SNVDA system expressed in Equation 4.23 because the SMRDA system behaves like a SNVDA system when $K_\eta = K_d$ and $K_\tau = 0$.

Case B: $K_\eta = 0$ and $K_\tau = K_d$

In this case, the output impedance Equation 4.26 can be written as:

$$Z'(s) = \frac{J_m \omega_\tau s}{J_m s^2 + J_m \omega_\tau s + K_\tau(K_p + 1)\omega_\tau} \tag{4.28}$$

To consider the effect of ω_τ on $Z'(s)$, the output impedance was plotted against ω_τ as shown in Fig.4.10. Similar to the SNVDA system, the output impedance of the SMRDA system is also low when the frequency is low. The output impedance magnitude reaches its peak value around the system high cutoff frequency. However, being different from the SNVDA system, the output impedance reduces continuously and maintains low value when the frequency approaches infinity. In other words, the system seems to be more compliant to the load velocity in both the low and high frequency range. The position of the peak value is depended on the value of ω_τ.

Fig.4.11 shows the output impedance for different values of K_η and K_τ when $\omega_\tau = 20 rad/s$. It is observed that that the final value of the output impedance described in Equation 4.25 approaches rather than as in the case of the SNVDA system when the frequency approaches infinity.

4.5 Conclusion

In this chapter, the analysis showed that the introduction of the MR damper into the series damper actuator (SDA) system increases the order of the system. Low bandwidth, ω_τ, of the MR damper response to the input current would compromise

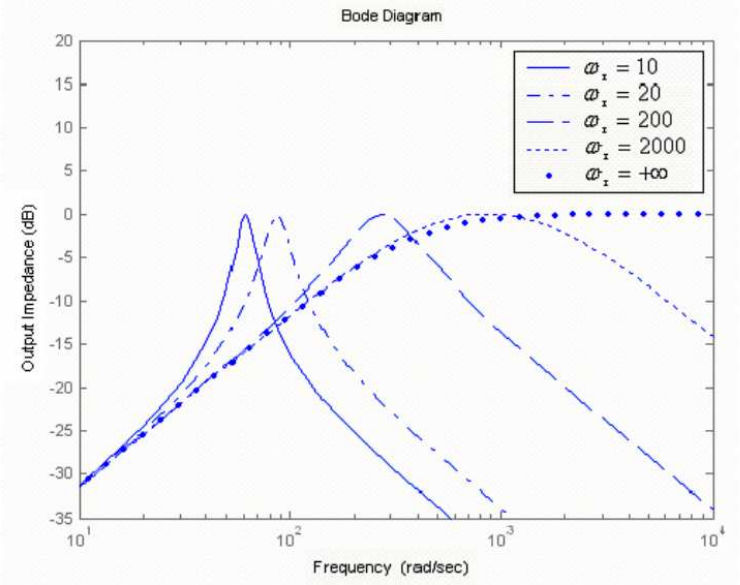

Figure 4.10: Output impedance of the SMRDA system with different value of ω_τ when $K_\eta = 0$ and $K_\tau = K_d$

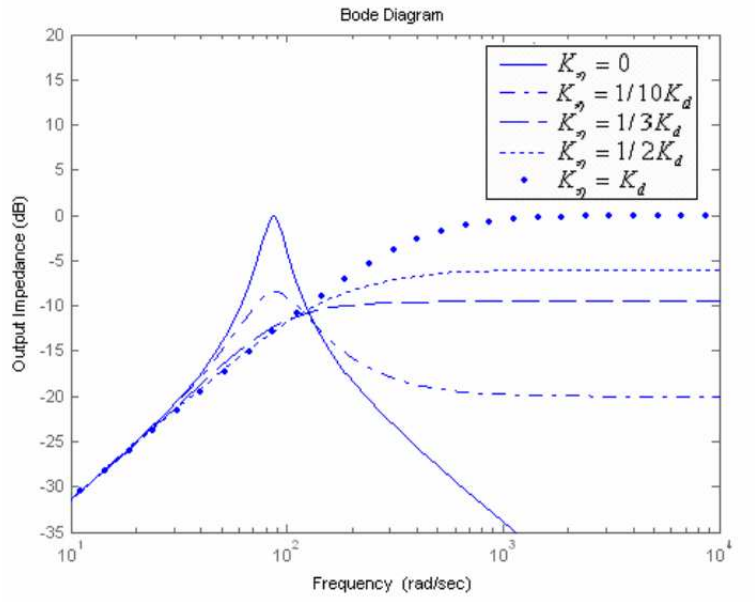

Figure 4.11: Output impedance of the SMRDA system with different values of K_η and K_τ when $\omega_\tau = 20 rad/s$.

the bandwidth of the SDA system. The overall system bandwidth will reduce with the value of ω_τ. Therefore, to achieve large bandwidth for the SMRDA system, a large value for ω_τ is desirable.

In the analysis section of Chapter 3, the extra dynamics of MR fluid damper, $G(s)$, is neglected by treating the damper with a linear dynamics, that is, $G(s) = K_\tau$ or $\omega_\tau = \inf$. However, in practise the extra dynamics of MR fluid damper has a finite value of ω_τ, which is not neglectable. From above analysis, therefore, it can be known that the extra dynamics, $G(s)$, would delay the system response and hence reduce the bandwidth of the SDA system. That is just the explanation of the unexpected low bandwidth observed in the experimental results of Chapter 3.

It was also shown that the dynamics of the MR damper causes the output impedance of SDA system to be low at both low and high frequency range. The output impedance reaches the maximum value around the system high cutoff frequency. When the frequency approaches infinity, the output impedance of the SMRDA system approaches the value of K_η, the Newtonian viscous component of the MR damper. To reduce the output impedance at high frequency, a small K_η is desirable. However, a small K_η, which usually means a large ratio of K_τ to K_η, makes the SMRDA system more susceptible to the dynamics of the MR damper especially when the value of ω_τ is low.

The models and the analysis were based on a simple proportional feedback controller and the assumption that the MR damper has a first order dynamics. The results may be different with different controllers and MR models. However, these assumptions helped to simplify the modelling and analysis, yet still able to provide much important information on the system basic properties. The information will be useful for the design of the SMRDA system.

Now, the negative effect of MR fluid damper extra dynamics on system response and bandwidth has been revealed. In the next chapter, a delicate controller will be designed, which is intended to compensate this extra dynamics and therefore reduce the system response lagging and, consequently, increase the system bandwidth.

Chapter 5

Controller Design of Series Damper Actuator Based on MR Damper

Compared with the SEA system, one of the advantages of SDA is that the damping coefficient of the damper can easily be varied by adopting an appropriate damper design. The damping coefficient can then be adjusted according to the environment conditions. For example, at high force and low force range, the damping coefficient can be increased and decreased respectively to allow a proper corresponding relative velocity in the damper. This endows the system with higher force fidelity at both high and low force range. In an experimental setup of the SDA system, Magneto-Rheological (MR) fluid damper is used to emulate a viscous damper with variable damping coefficient.

Due to the nonlinear dynamics property of the MR fluid damper, the controller design becomes critical to achieve variable damping coefficient and obtain a satisfactory force fidelity with the SDA system based on MR fluid damper. In Chapter 4, the analysis results have shown that the extra dynamics of MR fluid damper is not neglectable and would cause response delay and reduce system bandwidth. Hence, a more advanced controller should be developed to replace the simple controller

proposed in Chapter 3 and therefore give system better force fidelity and larger bandwidth.

Although modelling and control of MR fluid damper has been intensively investigated in recent years (Dyke, 1997; Spencer, 1997; Pan, 2000; Li, 2004), for most cases, the MR fluid damper is studied as a semi-active device in the field, such as, seismic response reduction and suspension system. So far no research work is for the purpose of active force control as it would be in SDA actuator system. Furosho has proposed a kind of series MR damper actuator, in which output of the MR fluid damper was assumed to be independent from the damper velocity(Takesue, 2000, 2001, 2003). Therefore, the control problem of MR fluid damper was not investigated intensively in his work. In our previous work (Chew, 2004-2), although a simple linearization controller for the MR fluid damper has been implemented to control the SDA system, there is still a lot of space to increase the system performance in terms of the output force fidelity and the system bandwidth.

Note that although our actuator system based on the MR damper has a similar physical structure as the MR damper actuator proposed by Furusho's group, the approach adopted by our system for force control is different from theirs. The main difference is that the latter assumes that the output force is not dependent on the input/output relative velocity of the damper. The drive unit (motor) mainly acts as a velocity source to one end of the MR damper. The output force of their actuator system is controlled mainly by varying the current supply to the MR fluid damper, which will in turn alter the Coulomb friction behaviour for the damper. The function of the MR damper is more like a force clutch. For our SDA system, the target damper is desirable to be of viscous type whose damping force is dependent on the damper's input/output relative velocity. A force sensor is not necessary to implement closed-loop feedback control. If the constitutive property of the damper is known, the output force can be indirectly controlled by controlling the damper's input/output relative velocity. That is, the damper is partially acting as a force sensor. The MR damper in our actuator system is mainly used to emulate a viscous damper. In fact, the system can use a broad range of dampers, such as linear or nonlinear viscous

damper, MR fluid damper, ER fluid damper, or other types of dampers, as long as their force output can be made to be a function of the input/output relative velocity (either by virtue of their designs or by software control).

In this chapter, we propose the inverse dynamics control approach for the SDA which is based on MR fluid damper. In Section 5.1, a modified Bingham model will be presented and compared, in Section 5.2, with two well-known MR fluid models, Bingham model and Bouc-Wen model, in terms of model accuracy and model invertibility. In Section 5.3, inverse dynamics control schemes for the MR damper based SDA system will be proposed. In Section 5.4, the experiment setup will be introduced and experimental results will be presented and discussed.

5.1 Models of MR Fluid Damper

In this section, a modified Bingham model is proposed for the MR fluid damper. To show the performance of this proposed model, it is compared with two popular MR fluid dynamics models, Bingham model and Bounc-Wen model.

5.1.1 Bingham Model

Bingham viscoplastic model (Pan, 2000) is often used to describe the behavior of MR fluid dampers. Based on this model, Stanway proposed a mechanical model to represent MR fluid damper, called Bingham model. The model consists of a Coulomb friction element placed in parallel with a viscous damper, as shown in Fig.5.1.

The output force of the MR fluid damper is given by

$$F = f_0 sgn(v) + c_0 v \tag{5.1}$$

$$f_0 = f_a + f_b I \tag{5.2}$$

$$c_0 = c_a + c_b I \tag{5.3}$$

where f_0 is the frictional force, c_0 is the damping coefficient, I is the current applied

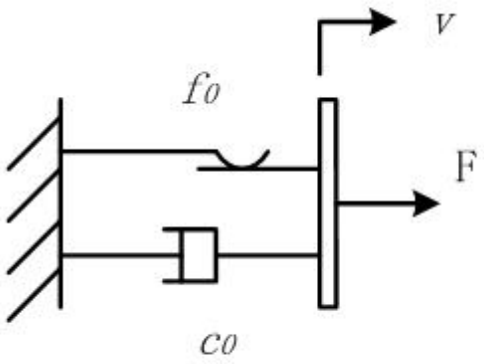

Figure 5.1: Bingham model of MR fluid damper

to the damper, c_a and f_a are constant values and equal to the frictional force and damping coefficient, respectively, when there is no current applied, c_b and f_b are coefficient with the damper input current I.

5.1.2 Bouc-Wen Model

Fig. 5.2 presents a basic mechanism of Bouc-Wen model which is quite often adopted in the analysis of non-linear hysteresis behavior(Spencer, 1997). The damping force of MR damper can be given by:

$$F = c_0 v + d_0 z \tag{5.4}$$

where internal state variable z is governed by:

$$\dot{z} = -\gamma z|v||z|^{n-1} - \beta v|z|^n + Av \tag{5.5}$$

z is an evolutionary variable that accounts for the history dependence of the response. The model parameters depend on the current I applied on the damper as follows:

$$c_0 = c_a + c_b u \qquad d_0 = d_a + d_b u$$

where u is given as the output of first-order filter:

$$\dot{u} = -\eta(u - I) \tag{5.6}$$

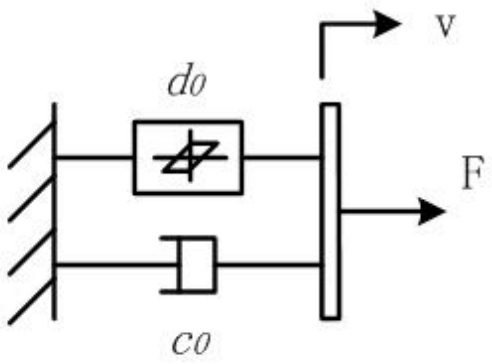

Figure 5.2: Bouc-Wen model of MR fluid damper

5.1.3 Modified Bingham Model

To find a model which is more suitable for inverse dynamics control of MR damper for an SDA system, a modified Bingham Model is also proposed in this section. Based on the Bingham model, the modified model we propose can be described by following equations:

$$F = f_0(1 - e^{-\beta|v|})sgn(v) + c_0 v \tag{5.7}$$

$$f_0 = f_a + f_b u \qquad c_0 = c_a + c_b u \tag{5.8}$$

$$\dot{u} = -\eta(u - I) \tag{5.9}$$

Comparing to Bingham Model, the modified model has two main changes. One is the velocity factor $(1 - e^{-\beta|v|})$. It is supposed to reduce the model error when damper proceeds into hysteresis region and therefore gives a more accurate result for model parameter identification. The other is Eq.5.9, a first order filter. Eq.5.9 is necessary to model the dynamics involved in reaching equilibrium and driving the electromagnet in the MR damper.

To compare the three models, let's denote Model 1, Model 2 and Model 3 for

Bingham Model, Bouc-wen model and modified Bingham model respectively. Model parameters are identified using Nonlinear Least Square Method.

5.2 Model Comparison

To show the ability for implementing inverse dynamics control, the proposed MR fluid damper model is compared with the other two models in terms of model accuracy and model invertibility. For model accuracy, the models are input with damper velocity and damper current and outputs prediction force (Fig.5.3). Model accuracy is evaluated by considering the prediction force error. For model invertibility, inverse models are input with desired damper force and desired damper velocity and outputs predicted damper current (Fig.5.4). The model invertibility is evaluated considering the stability of the output current.

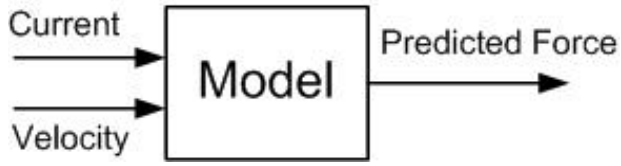

Figure 5.3: Evaluation for model accuracy

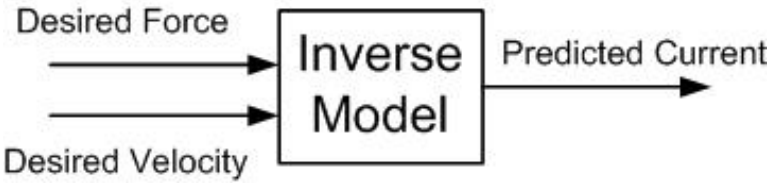

Figure 5.4: Evaluation for model invertibility

5.2.1 Model Accuracy

Fig.5.5 shows the torque prediction results of these three models when the damper velocity and current are both varying. It is observed from the figure that Model 2 and Model 3 are more accurate, while the prediction of Model 1 has a certain phase leading to the actual value and therefore model 1 obviously has larger error than the other two models. The reason is that the slow response of the MR damper to

input current, which is not included into Model 1, has been modelled in Model 2 and Model 3 by first order filter (Eq.5.6 and Eq.5.9). Between Model 2 and Model 3, there is no much difference in terms of the prediction error.

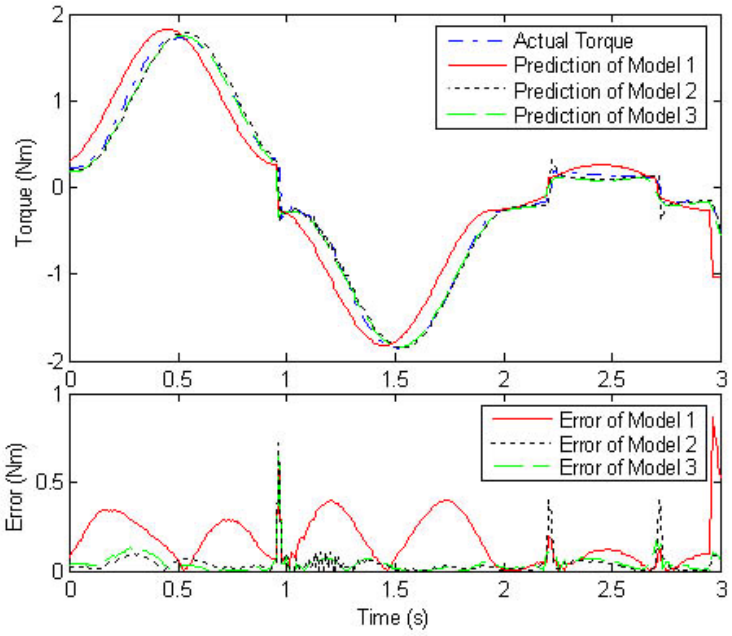

Figure 5.5: Comparison between the experimental output torque and predicted output torque based on three models

Another difference between Model 1 and Model 3 is the velocity factor of the proposed modified Bingham model, $(1 - e^{-\beta|v|})$. This velocity factor is supposed to reduce the model error in the hysteresis region (small area around zero velocity) of the MR fluid damper and therefore give a better result for model parameter identification. To show the function of this velocity factor, models response are compared when damper input current is kept constant as shown in Fig.5.6. Models error are shown in Fig.5.7. When current I is a constant, the low pass filter (Eq.5.9) in the Model 3 actually has no effect on model dynamics. In this case, the difference between Model 1 and Model 3 comes from the velocity factor. It is shown that the Model 3 is more accurate than Model 1. Especially, out of the hysteresis area, the error of Model 3 is quite small.

It is easy to understand that the velocity factor only functions around zero velocity. When damper velocity, v, is large, this factor actually has no effect on model

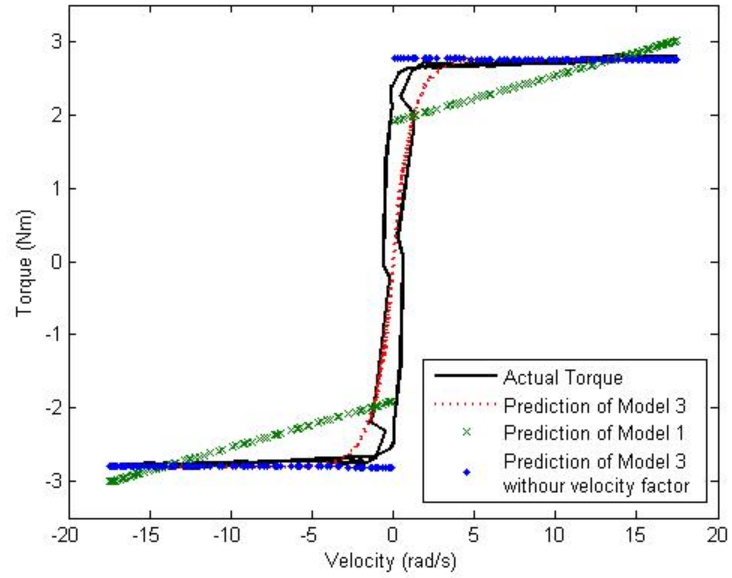

Figure 5.6: Models response comparison when damper current is constant

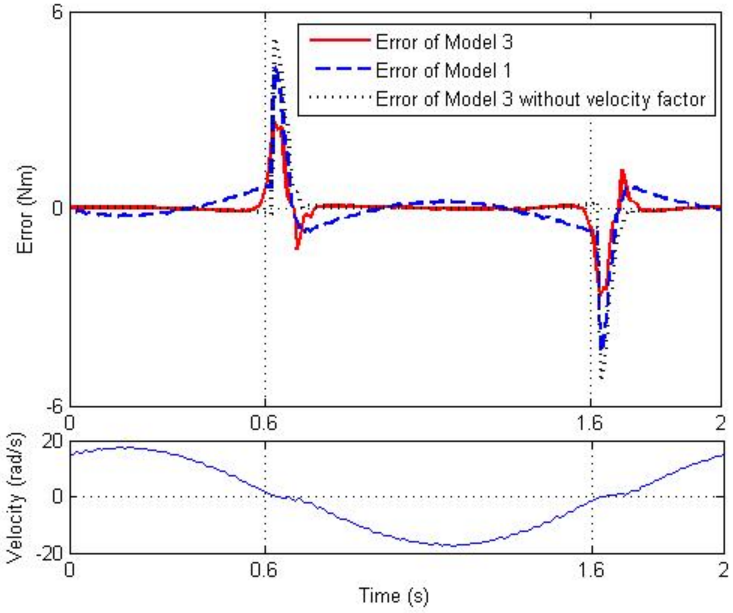

Figure 5.7: Models error when damper current is constant

dynamics because the value of velocity factor approaches to one. Therefore, as shown in Fig.5.7, removing the velocity factor from Model 3 (after parameter identification) only increases the model peak error in the hysteresis region and doesn't reduce the model accuracy out of this region. But large peak error would give a poor result for model parameter identification due to the error equal distribution effect of the Least Square Method, as it does for Model 1. Consequently, comparing with Model 3 after removing velocity factor, Model 1 has a smaller peak error in the hysteresis region, but the error out of the hysteresis area becomes fairly large because of the improperly identified model parameters. According to Fig.5.7, Model 3 has the smallest peak error. The introduction of multiply velocity factor $(1 - e^{-\beta|v|})$ reduces the model peak errors in the hysteresis region of the MR fluid dynamics and, therefore, gives the model a more accurate parameter identification when the Nonlinear Least Square Method is carried out. That is why Model 3 is more accurate than Model 1 even if the velocity factor is removed after parameter identification.

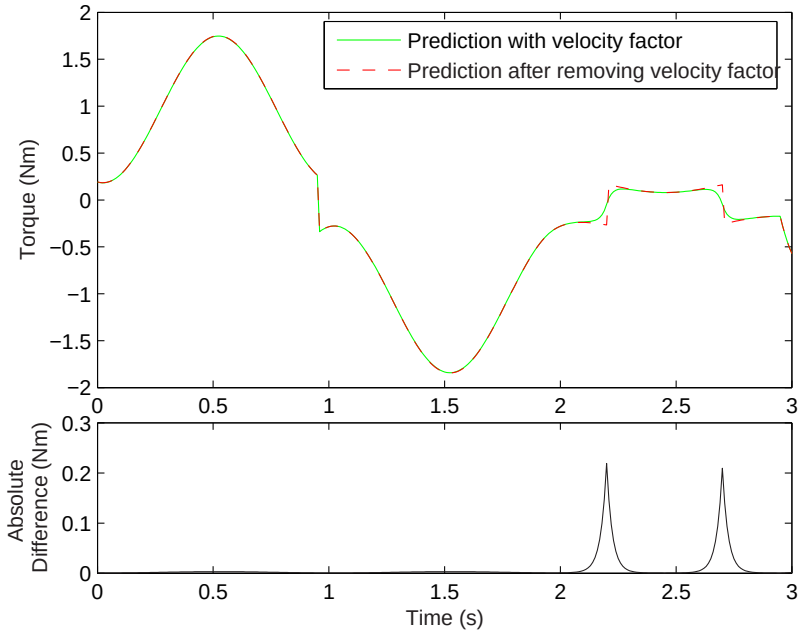

Figure 5.8: Comparison of the predicted output of Model 3 with and without the velocity factor after model parameter identification

In fact, after the model parameters are identified, the multiply velocity factor $(1 - e^{-\beta|v|})$ in Model 3 can be removed form the inverse dynamics equations without

much effect on the model accuracy. Fig.5.8 shows the prediction results of Model 3 with and without the velocity factor with varying damper velocity and damper current. There is only a small difference between the two model outputs when the damper goes into hysteresis region. However, without the velocity factor, Model 3 would be simpler and easier to be inverted.

Model 2, Bouc-Wen model, is a very popular model of MR fluid to describe hysteresis behavior. However, in this case, the hysteresis effect of MR damper is not dominant so that Model 2 can not show better results than that of Model 3 with respect to the model accuracy.

5.2.2 Model Invertibility

According to the MR fluid damper models as shown in Subsection 5.1, the inverse models can be expressed in following equations for these three models respectively

- For the Bingham model (model 1):

$$I = \frac{F_d - f_a sgn(v_d) - c_a v_d}{f_b sgn(v_d) + c_b v_d} \tag{5.10}$$

- For the Bouc Wen model (model 2):

$$I = u + \frac{\dot{u}}{\eta} \tag{5.11}$$

$$u = \frac{F_d - c_a v_d - d_a z}{c_b v_d + d_b z} \tag{5.12}$$

$$\dot{z} = -\gamma |v| z |z|^{n-1} - \beta v |z|^n + Av \tag{5.13}$$

- For the proposed model (model 3):

$$I = u + \frac{\dot{u}}{\eta} \tag{5.14}$$

$$u = \frac{F_d - f_a sgn(v_d) - c_a v_d}{f_b sgn(v_d) + c_b v_d} \tag{5.15}$$

Model 1, the Bingham model, is the simplest model and all parameters are linear and therefore it can easily be inverted. For Model 3, the velocity factor has been removed after model parameter identification. Therefore, comparing with the inverse Model 1, the inverse model of Model 3 is only different from it with an inverse of a first order low pass filter. The inverse of low pass filter in Eq.5.14 contains the derivative of internal variable u and therefore it would generate peak current output for the inverse model if the curve of the internal variable u is not smooth. But this peak current output can be mitigated by setting a boundary for the predicted current of the inverse model.

It is easy to see that the inverse model of Model 2 is the most complex with nine system parameter and a complicated internal state variable z (Eq.5.13). In Fig.5.9, the prediction current based on these three inverse models is shown. Because of the introduction of low pass filter in Model 2 and Model 3, the output damper current of inverse model has some noise like peaks when the desired force or velocity profile goes across zero. Furthermore, according to Fig.5.10, due to the presence of internal state variable z, Eq.5.5, the output of inverse Model 2, when there is sudden change, e.g. a step input, with the inverse model input of desired force or desired velocity, may have some oscillation before it goes to a steady value. In fact, it has been observed in the experiments that the output of inverse Model 2 may be instable with certain desired velocity and desired force profiles. The analysis results show that Model 1 and Model 3 has better invertibility than Model 2. In general, the more complex a MR damper model, the worse the invertibility of the model.

From the above two subsections, it can be concluded that the modified Bingham model and the Bouc-Wen model have a better model accuracy than Bingham model, but the invertibility of the Bouc-Wen model is inferior to the other two models. Considering both the model accuracy and invertibility, the proposed modified Bingham model,Model 3, is the best choice to implement inverse dynamics control for series damper actuator based on MR damper.

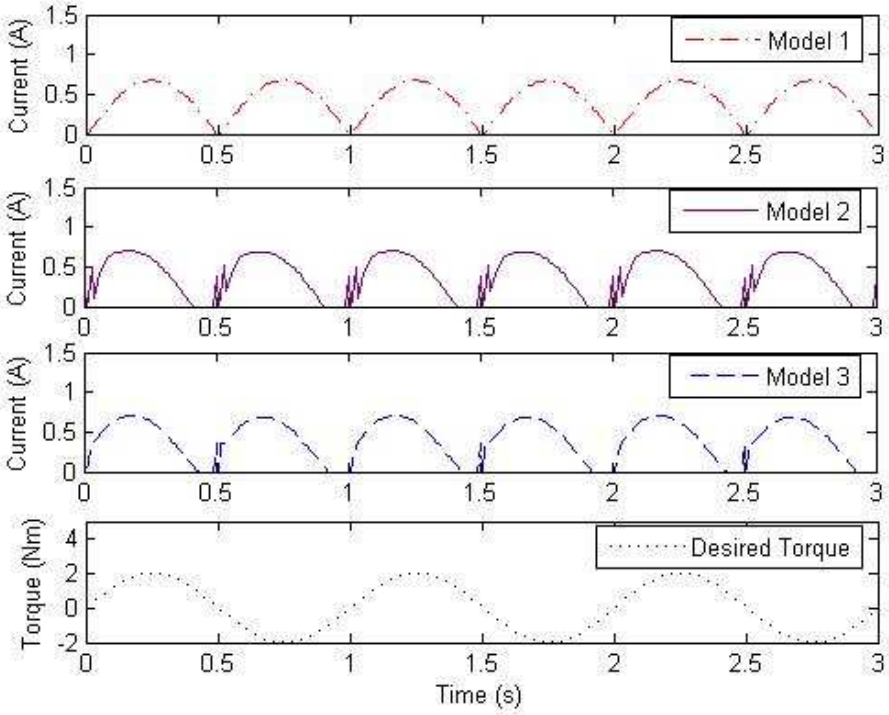

Figure 5.9: Output of three inverse models when the desired torque is sinusoidal wave

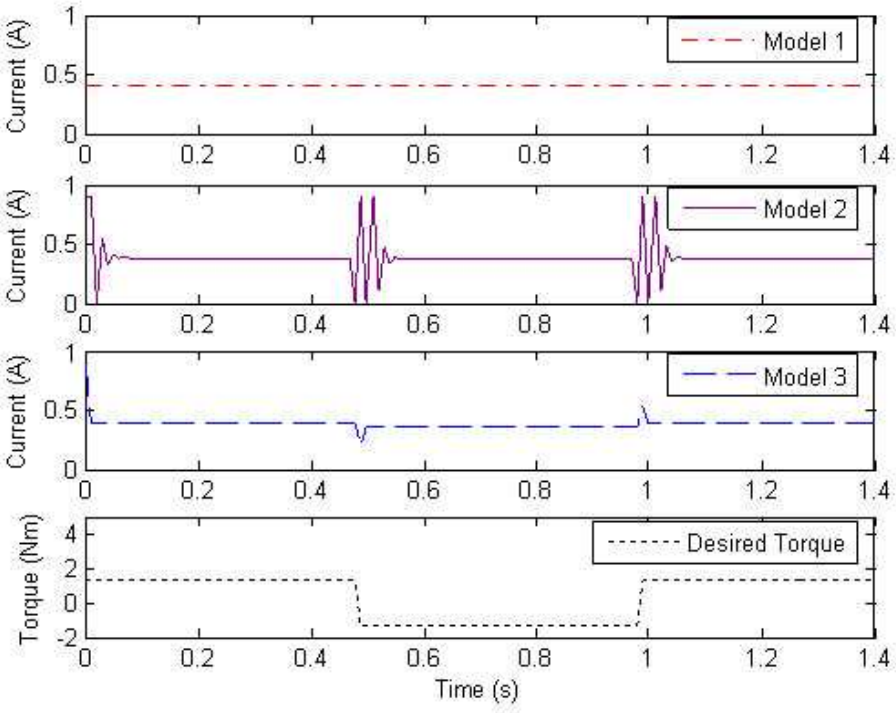

Figure 5.10: Output of three inverse models when the desired torque is square wave

5.3 Control Schemes

Inverse dynamics compensation is an intuitive way to linearize hysteresis behavior. The control scheme for inverse dynamics control of MR damper is shown in Fig.5.11 (Scheme 1), where F_d is desired damping force/torque, v_d is desired damper velocity, k_d is desired damping coefficient and $F_d = k_d \cdot v_d$, v_m is motor velocity and v_L is load velocity.

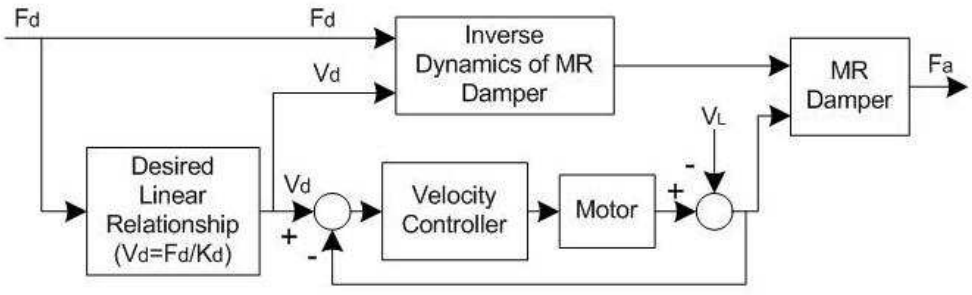

Figure 5.11: Inverse dynamics control scheme without force feedback loop

Due to the inevitable model error, there would be some error between the output force of MR damper, F_L, and the desired output force,F_d. One way to reduce this error is to implement a force feedback loop. Fig.5.12 shows a control scheme with force feedback closed-loop (Scheme 2). In this scheme, there are two control loops. One is the motor velocity control loop to control the damper velocity. The other control loop is the damper current control loop. In the experiments, a PD controller and a P controller are used for the velocity loop and current loop respectively. By achieving the desired damping force F_d and the desired damping velocity v_d with these two closed loop control, the desired virtual damping constant k_d is obtained in the series damper. Hence the variable damping coefficient can be implemented just by changing the desired value of k_d in the control scheme.

Different to semi-active control for most applications of MR fluid damper, in which the damping velocity is dependant on external environment rather than driven by a motor, in this control scheme both damper velocity and damper current are actively controlled with two closed-loops.

It should be noted here that, as long as the force control performance based on

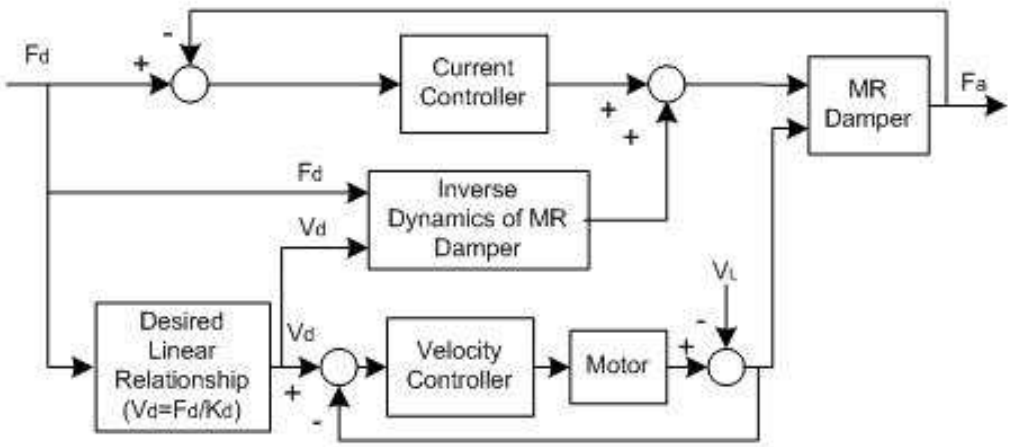

Figure 5.12: Inverse dynamics control scheme with force feedback loop

control scheme 1 is satisfactory, feedback loop based on output force information is no necessary, as mentioned in Section 2.

5.4 Experimental Results

An experimental setup of the MR fluid damper based Series Damper Actuator (SDA) and its schematic diagram have been shown in Fig.3.11 and Fig.3.12 respectively and described in Chapter 3.

To show the effect of modified Bingham model, the inverse dynamics compensation results are compared between Model 1 and Model 3. The MR damper output under control scheme 1 for sinusoidal and step force are shown in Fig.5.13 and Fig.5.14. It can be shown that damper output with inverse Model 3 has a better phase matching and faster step response. Due to the larger model identification error, Model 1 has an inferior performance than Model 3. It can be seen from Fig.5.15, MR damper after linearization (scheme 1) with inverse Model 3 has a better linearity than that with inverse Model 1, although there still exists some hysteresis like error.

Low bandwidth of the MR fluid damper reported in Chapter 3 is one of the main problems we want to be solved in this chapter. Fig.5.16 shows the bandwidth of MR damper after inverse dynamics compensation based on Model 1 and Model 3. The bandwidth was tested with control scheme 1. It shows that the MR fluid damper

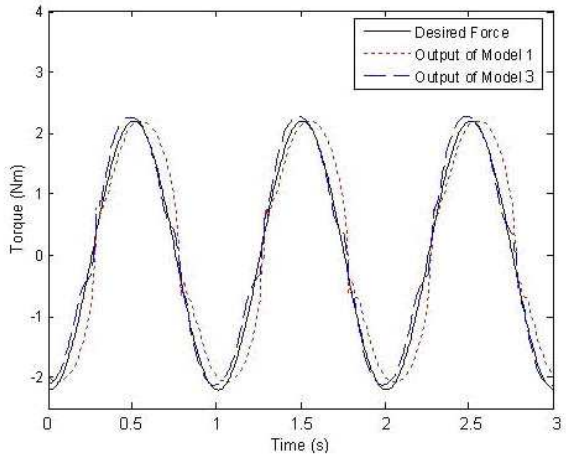

Figure 5.13: Output of MR fluid damper for sinusoidal wave with the control scheme 1 based on the Model 1 and the Model 3

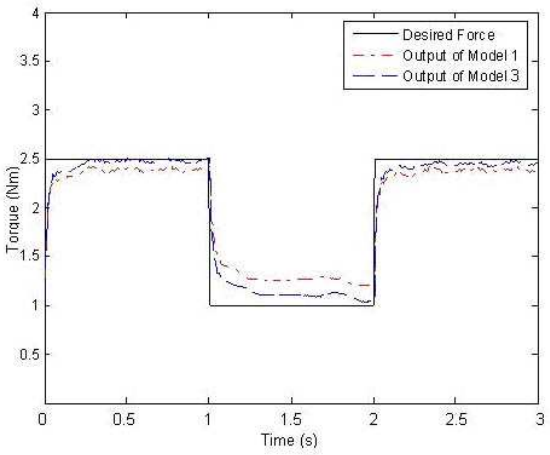

Figure 5.14: Output of MR damper for square wave with control scheme 1 based on Model 1 and Model 3

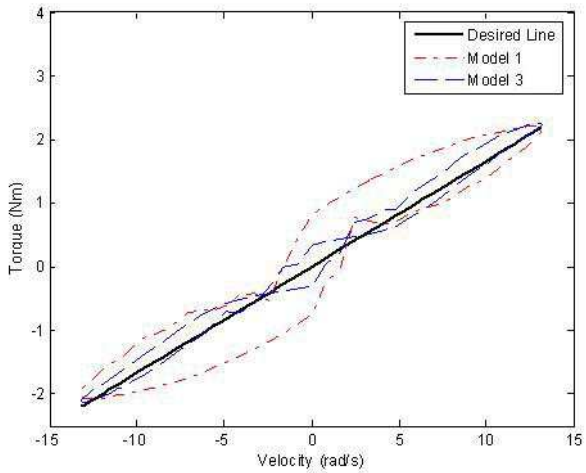

Figure 5.15: Linear properties of MR damper after inverse dynamics compensation (scheme 1) Based on Model 1 and Model 3

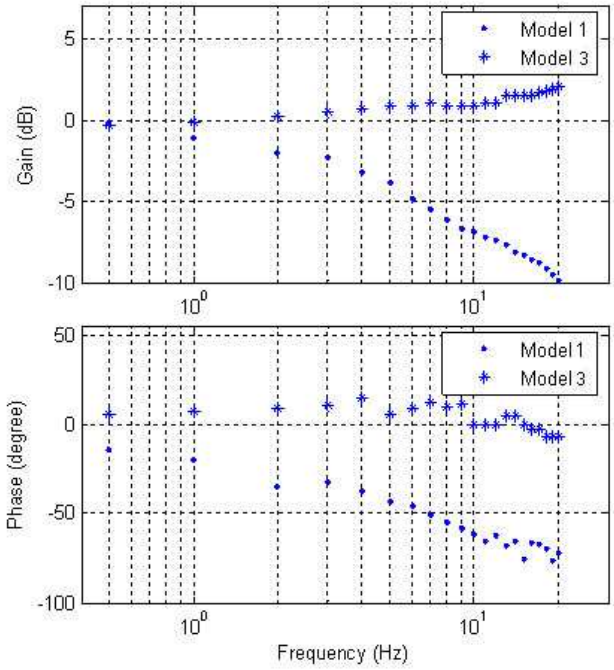

Figure 5.16: Bode plots of MR fluid damper after linearization based on Model 1 and Model 3

after linearization with the inverse of Model 3 has a larger bandwidth than that with Model 1. The larger bandwidth comes from the fact that Model 3,with the first order low pass filter in its model (Eq.5.9), can successfully capture the dynamics delay of MR damper to the input current and, therefore,effectively compensate it.

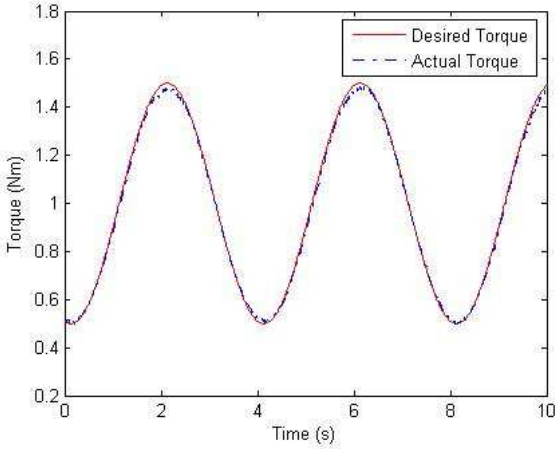

Figure 5.17: Torque tracking following a sinusoidal reference when the damping constant $k_d = 0.17Nms$

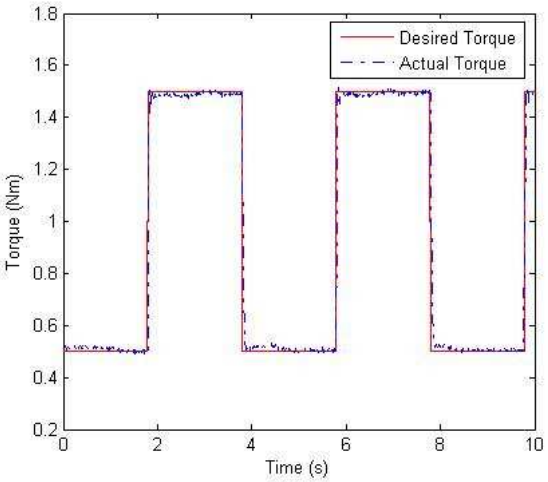

Figure 5.18: Torque tracking following a step reference when the damping constant $k_d = 0.17Nms$

The output force fidelity can be furtherly increased with force feedback loop. Based on Model 3, the performance of the experimental SDA system with the force feedback inverse dynamics control scheme (scheme 2) is also tested. The results of the fixed end experiment are shown in Figs.5.17 to 5.20. Fig.5.17 and Fig.5.18 illustrate

the system responses to sinusoidal and step references, respectively, when $k_d = 0.17Nms$. The results show that the experimental SDA system achieves force control with a quite high fidelity. Comparing with the outputs, (Fig.5.13 and Fig.5.14),of SDA under the control scheme without force feedback (scheme 1), the force tracking error is reduced with the force feedback control loop.

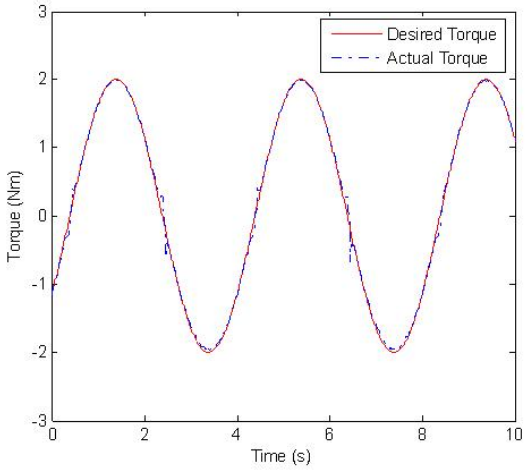

Figure 5.19: Torque tracking following a sinusoidal reference when the damping constant $k_d = 0.34Nms$

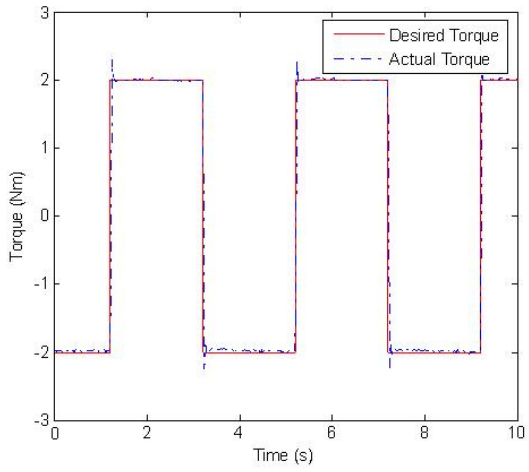

Figure 5.20: Torque tracking following a step reference when the damping constant $k_d = 0.34Nms$

Variable damping coefficient is another advantage of the experimental SDA system. Fig.5.19 and Fig.5.20 shows the system responses for sinusoidal and step inputs, respectively, after the damping constant k_d has been doubled to $k_d = 0.34Nms$ while

the amplitudes of the inputs were increased by four times.

5.5 Summary

In this chapter, the control problems of SDA system were investigated. A general controller for SDA system was proposed. It can be used as high level controller for SDA system, in which the damping coefficient of the series damper is assumed to be a constant (viscous type).

For the SDA system based on MR fluid damper, the controller was different due to the nonlinear dynamics property of MR fluid damper. For such SDA system, inverse dynamics control schemes were developed for the linearization of the MR fluid damper. To achieve this kind of controller, a modified Bingham model for the MR fluid damper was proposed and compared with the two very popular MR fluid models, Bingham model and the Bouc-Wen model. Model comparison was done in terms of model accuracy and model invertibility. Simulation and experimental results showed that the proposed model is more suitable to implement inverse dynamics control for such a SDA system. With the proposed control schemes, higher force fidelity and larger system bandwidth had been achieved comparing with the results shown in Chapter 3.

Chapter 6

Plant Design of Series Damper Actuator

SDA system design includes plant (hardware) design and controller (software) design. In the pervious chapters and our past work (Chew, 2004-2; Zhou, 2005-1), the controller design has been extensively investigated and satisfactory results had been reported. In the patent application file (Chew, 2004-1), a rough design of SDA system, including system architecture, plant mechanical structure, and so on, has been presented. However, the core of the SDA hardware (plant) design, the design or selection of series damper and the DC motor, is still unrevealed. The purpose of this chapter is to provide a standard design procedure of the damper and motor selection and optimization for the SDA system. By simply following these procedures with a set of given particular system performance requirements or parameters, a satisfactory SDA design result can be achieved.

In this chapter, the design process of our experimental SDA system (based on MR fluid damper) was used as the example to illustrate the design procedures. In the first part of this chapter (Section 6.1), the design steps for damper and motor selection was introduced. The motor optimized selection was carried out using Mechatronic Design Quotient (MDQ) method. In the second part of this chapter (Section 6.2), a novel compact MR fluid damper was designed and tested.

6.1 Component Selection for SDA System

In general, the SDA plant includes a series damper, a motor, sensors and motor driver, if any. The SDA hardware design should begin with the selection or design of the series damper and the motor, because the selection of other hardware components, such as sensors and micro-controller usually should refer directly or indirectly to the selected damper, motor and their attachments. Between the damper and motor, the former should be decided first, since the suitable dampers are quite limited, while available motors are versatile.

First, the initial design parameters should be given. In most cases, the original requirements for a designed system are given in the terms of specified system performances, such as the rise time, over shoot, steady state errors, etc. Those considerations are usually used for controller design. Therefore, more freedom can be given for the initial of the hardware design process.

Here following three parameters are given from design specifications or assumption.

- Maximum output force F_{L_max}
- Maximum load velocity V_{L_max}
- Minimum system bandwidth ω_{min}

6.1.1 Damper Selection

The series damper in the SDA system can either be linear or rotary. Furthermore, there are different choices for the damper, such as viscous damper, MR fluid damper, ER fluid damper, variable orifice viscous damper, eddy current damper, powder clutch, etc.

The selection of damper should be based on the output force, operating speed, damping coefficient, stroke range, size, weight, cost, etc. Different design considerations or methods may give different initial design requirements. In this case, two

damper parameters should be determined, the maximum variable damping coefficient B_{max} and, the maximum damper relative velocity V_{D_max}.

Step1. Maximum variable damping coefficient B_{max}

The series damper in the SDA system is required to have a variable damping coefficient. Therefore, determining the range of variable damping coefficient is necessary to select a suitable damper. If there is no explicit requirement for the range of damping coefficient, the maximum damping coefficient can be determined by considering the efficiency problem.

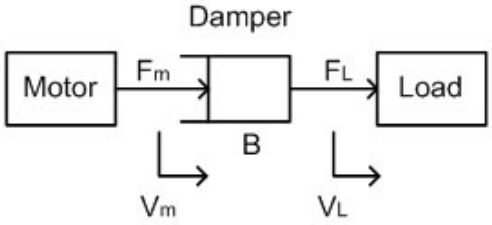

Figure 6.1: General model of SDA actuator plant

A general model of SDA actuator plant, a damper series connected between a motor and load, is shown in Fig.6.1, where F_m is the motor output force, V_m is the motor output velocity, F_L is the actuator output force (load force), V_L is actuator output velocity (load velocity), and B is the damping coefficient. When SDA actuator system works actively, power will be transmitted from the motor to the load through the series damper. According to the plant model, the following equations can be obtained.

Damper input end power P_m:

$$P_m = F_m \cdot V_m \tag{6.1}$$

Damper output end power P_L:

$$P_L = F_L \cdot V_L \tag{6.2}$$

Neglecting the inertia force of the damper, we have:

$$F_m = F_L \tag{6.3}$$

and

$$F_L = BV_D \tag{6.4}$$

where V_D is the damper relative velocity and $V_D = V_m - V_L$.

The power dissipated in the damper (P_D) is:

$$P_D = P_m - P_L = F_L(V_m - V_L) = F_L V_D = \frac{F_L^2}{B} \tag{6.5}$$

The efficiency (η) for the power transmitted through the series damper is:

$$\eta = \frac{P_L}{P_m} = \frac{P_L}{P_L + P_D} \tag{6.6}$$

Solving B from the above equations yields:

$$B = \frac{\eta F_L}{(1-\eta)V_L} \tag{6.7}$$

It is assumed that, when the maximum damping coefficient B_{max}, maximum output force F_{L_max}, and maximum load velocity V_{L_max} are achieved in the series damper, a certain efficiency η_m ($0 < \eta_m < 1$) is also obtained. Therefore, it can be written that:

$$B_{max} = \frac{\eta_m F_{L\_max}}{(1-\eta_m)V_{L\_max}} \tag{6.8}$$

Step2. The maximum damper relative velocity V_{D_max}.

Theoretically, the damping coefficient B can vary from 0 to B_{max}. However, there should be a certain range limit of damping coefficient B for any certain output force F_L, considering the damper relative velocity limitation. For example, with a certain output force F_L, if the damping coefficient B is set to be vary small, say close to zero, as result, an impracticably high damper relative velocity will be required

according to Eq. 6.4.

Therefore, it can be assumed that, when maximum output force F_{L_max} is achieved, the allowable range of varying damping coefficient is $\beta B_{max} \sim B_{max}$ (β is called varying range factor and $0 < \beta < 1$). Here we define that the maximum damper relative velocity V_{D_max} is achieved when output force is maximum (F_{L_max}) and required damping coefficient is minimum (βB_{max}).

Therefore, the maximum damper relative velocity V_{D_max}:

$$V_{D\_max} = \frac{F_{L\_max}}{\beta B_{max}} \tag{6.9}$$

Step3.The minimum damper bandwidth ω_D

With damper relative velocity V_D as the input and damping force F_L as the output, the series damper has a transfer function defined as

$$G_D(s) = \frac{F_L}{V_D} \tag{6.10}$$

The bandwidth is the frequency, at which the system frequency response (gain) has declined $3dB$ from it low-frequency value (Dorf, 2004).

For a viscous damper, the constitutive equation can be written as

$$F_L = BV_D \tag{6.11}$$

where B is constant damping coefficient.

Therefore, the transfer function for such a viscous damper is

$$G_D(s) = \frac{F_L}{V_D} = B \tag{6.12}$$

Obviously, it is a zero order system (constant gain), and therefore the bandwidth is infinity since the response gain keeps constant with the frequency. It may be true for a truly viscous damper, for which the bandwidth is very high and can be viewed as infinity.

However, infinite bandwidth may not be true for other series damper solutions of SDA system, such as Magneto-Rheological (MR) fluid damper. To emulate a viscous damper defined in Eq. 6.11, the MR fluid damper is controlled by a linearization algorithm to give a virtual constant damping coefficient B. This linearization process introduces some extra dynamics into the series damper, such as the electromagnetic response of the MR fluid. Therefore, the bandwidth of such virtual viscous damper is lower than that of a truly viscous damper.

To consider the bandwidth property of series damper, a first order model is used to represent the damper dynamics (Zhou, 2005-1):

$$G_D(s) = \frac{F_L}{V_D} = B\frac{\omega_D}{s+\omega_D} \tag{6.13}$$

where ω_D is the bandwidth of the model. If ω_D is infinite, Eq. 6.13 is equivalent to Eq. 6.12. To ensure the overall bandwidth of SDA plant, the bandwidth of the series damper should be checked.

Statement 1: To ensure a minimum overall bandwidth ω_{min} for the SDA plant, the damper bandwidth ω_D should satisfy following requirement:

$$\omega_D \geq \frac{1}{0.64}\omega_{min} \tag{6.14}$$

The proof of Statement 1 is shown in Appendix A.

Equation 6.14 defines the minimum damper bandwidth requirement to guarantee the SDA system a certain overall bandwidth. Damper bandwidth can be experimentally measured using frequency response method to ensure that it satisfies the minimal requirement, especially for those virtual viscous dampers.

Now the damper can be chosen by fulfilling the above three criteria: damping coefficient varying range, maximum damper relative velocity and minimum bandwidth. Furthermore, other requirements, if any, should also be satisfied, such as, stroke range, size, weight, cost, etc. If the damper would be designed rather than selected, the damper thermal balance between damper energy dissipation and damper

heat dissipation for continuous operation should also be considered. Heat sink may be used, if necessary.

6.1.2 Motor Selection

A motor should be selected to match the selected damper. DC motors are suitable for applications requiring continuous operation at high levels of torque and speed. DC motors are suitable to work in harsh environment and need minimal maintenance. For applications that require high torques and low speeds, suitable speed reducers may be employed.

The series dampers of SDA system have two different types: linear or rotary dampers. The motor should match with the series damper. Therefore, to work with the linear damper, a linear stage may be needed for the motor. One option is to use a lead screw or ball screw. Another option is to use linear motor.

When selecting a DC motor for a particular application, consideration must be given to the requirements of power, speed, torque, bandwidth, size, weight, and cost. A suitable speed transmission device (harmonic drive, gear unit, lead screw, etc) may have to be chosen as well, depending on the application.

Follows are nine steps to select a suitable DC motor based on the design requirements and selected series damper.

Step1. The maximum motor output velocity V_{m_max}

The maximum motor output (after gear reduction, if any) velocity V_{m_max} can be calculated as follow:

$$V_{m\_max} = V_{D\_max} + V_{L\_max} \tag{6.15}$$

To give some margin for motor output velocity, the maximum motor output velocity V_{m_max} can be written as

$$V_{m\_max} = (1 + \alpha)(V_{D\_max} + V_{L\_max}) \tag{6.16}$$

where α is velocity margin factor and $0 < \alpha < 1$.

Step2. The maximum motor acceleration A_{max}

Since the motor velocity V_m equals to the summation of the damper relative velocity V_D and load velocity V_L. Therefore, the maximum motor acceleration A_{max} can be obtained from following equation:

$$A_{max} = \frac{dV_m}{dt}|_{max} = (\frac{dV_D}{dt} + \frac{dV_L}{dt})|_{max} = A_{D\_max} + A_{L\_max} \tag{6.17}$$

where A_{D_max} is the maximum damper's relative acceleration and A_{L_max} is the maximum load's acceleration. The values of A_{D_max} and A_{L_max} can be obtained from the design specifications.

Step3. Output power of motor P_m

If the efficiency of motor transmission is neglected, the motor output force F_m is equal to the summation of the damper's inertia force and the actuator output force (load force). Usually, the damper's inertia force is negligible compared with the load force. Hence the required motor output power can be approximated as:

$$P_m = F_{L\_max} * V_{m\_max} \tag{6.18}$$

Step4. Selecting a motor based on the power requirement

Here, we choose a motor which can deliver the required output power. Considering overloading, wear, and malfunction issues, the motor should not be operated continuously at its peak power. The peak power should be at least twice of the power requirement for continuous operation. This power margin also helps to achieve better efficiency.

Step5. Gear Reduction N

After the motor is selected, the maximum rotor output torque M_{e_max} and the maximum rotor speed n_{e_max} will be used to determine the required gear reduction.

The minimal required gear ratio should be calculated based on the required

maximum motor output torque F_{L_max}.

$$N_{min} = \frac{F_{L\_max}}{M_{e\_max}} \tag{6.19}$$

While the maximum gear ratio can be calculated based on the required maximum motor output speed V_{max}.

$$N_{max} = \frac{n_{e\_max}}{V_{m_max}} \tag{6.20}$$

We have to check and ensure that the calculated N_{max} should be larger than N_{min}. If this is not true, the motor selected is not suitable and another alternative should be sourced (go back to Step4). Otherwise, the suitable gear reduction should be between N_{min} and N_{max}.

After the gear box is selected, the efficiency problem should be checked first to ensure that the output torque still meets the design requirement by fulfilling following mathematic relationship

$$M_{e\_max} \cdot N \cdot \eta_g \geq F_{L\_max} \tag{6.21}$$

where N is gear reduction and η_g is the efficiency of the selected gear box.

If this not satisfied, the gear box should be changed or go back to Step4 to select another suitable motor.

Following above steps, the resulted motor and gear reduction would ensure that the required maximum output torque and output speed is within the motor continuous operation area.

Step6. Motor bandwidth $\omega_{m'}$

The motor's (with gear reduction) open loop bandwidth (voltage input and velocity output) should be larger than required value.

Statement 2: To ensure a minimum overall bandwidth ω_{min} for the SDA plant, the DC motor (free end) bandwidth $\omega_{m'}$ should satisfy following requirement:

$$\omega_{m'} \geq \frac{J_m + J_D/N^2}{0.64 J_m} \omega_{min} \tag{6.22}$$

where J_m is the motor inertia and J_D is the damper input end inertia.

The proof of Statement 2 is shown in Appendix A.

Equation 6.22 defines the minimal bandwidth requirement of the DC motor. After the motor is selected, the motor bandwidth should be tested. If Eq. 6.22 can not be satisfied, the motor and/or gear reduction should be changed.

Step7. Motor inertia J_m

In the SDA system, the load is separated from motor by the series damper. The output shaft of the motor is connected to the input end of the series damper. Therefore, for the consideration of inertia matching, the motor inertia J_m should not be too small compared to the damper input end inertia J_D. If gear reduction (N) is used to increase the motor output capacity, the damper input end inertia reflected on the motor shaft will be reduced by N^2 times to J_D/N^2. For most cases, the reflected input end inertia of damper, J_D/N^2, is much smaller than the motor inertia, J_m. If it is not true, a larger gear reduction or a motor with larger inertia should be used.

Step8. Required motor torque F_{max}

The required motor torque is given by:

$$F_{max} = \frac{1}{N}\left(F_{L\_max} + A_{max}(J_D + N^2 J_m)\right) \tag{6.23}$$

Check and ensure that $F_{max} \leq M_{e\_max}$. Otherwise, go back to Step4 to change the selected motor.

Step9. Required motor current I_{max}

The motor current, I_{max}, required to generate the maximum rotor torque, F_{max}, is given by

$$I_{max} = \frac{F_{max}}{k_m} \tag{6.24}$$

where k_m is the torque constant of the motor.

Check and ensure that I_{max} is smaller than the motor rated current. Otherwise, go back to Step4 to change the selected motor.

The above two subsections describe how to select a suitable damper and a motor for the SDA system. Most of the time, the design procedure needs some iterations before a satisfactory plant can be achieved. Furthermore, the SDA plant component design/selection steps described above are based on some design specifications. Different initial design specifications or requirements would result in different design considerations and, consequently, different design steps. But the general steps described above can give the basic idea and guideline on how to design the SDA plant and help them to proceed to some specific design cases.

6.2 Case Study

An example of SDA plant design is shown in this section. The initial design specifications are given in Table 6.1.

Table 6.1: Specifications for SDA plant design

Actuator type	Rotary
Maximum output force (F_{L_max})	$3Nm$
Maximum load velocity (V_{L_max})	$4rad/s$
Minimum system bandwidth (ω_{min})	$7Hz$
Damping varying factor (β)	50%
Motor velocity margin factor (α)	50%
Maximum motor acceleration (A_{max})	$50rad/s^2$

Following the design steps described in the last section, an MR brake (MRB-2107-3, Lord Corporation) and a DC motor (3863A024C, Faulhaber) are chosen as the series damper and motor for the SDA system. The specifications of the selected MR fluid damper (MRB-2107-3) and the DC motor (3863A024C) are shown in Table 6.2 and Table 6.3. A setup of the designed SDA system was built and a picture is shown in Fig. 6.2. In this setup, besides the motor and series damper, there are two encoders mounted to measure the damper input velocity and output velocity respectively. The relative velocity of the damper is obtained from the difference between the readings from these two encoders. This SDA system also had been tested and good results had been reported in (Chew, 2004-1; Zhou, 2005-1).

Table 6.2: Typical data of MRB-2107-3 MR brake

Maximum torque	$5.6Nm$
Damping coefficient varying range (virtual)	$0 \sim \infty Nms$ (theoretically)
Bandwidth	$25Hz$
Maximum operating speed	$1000RPM$ $(105rad/s)$
Input end inertial (J_D)	$1600gcm^2$
Diameter	$92.2mm$
Length	$36.6mm$
Weight	$1410g$
Operating temperature range	-30^oC to 70^oC

Table 6.3: Specifications of two suitable DC motor solutions

	Motor Solution 1 (Faulhaber 4490H024B)	Motor Solution 2 (Faulhaber 3863A024C)
Nominal voltage	24 V	24 V
Output power	201 W	220 W
Weight (excluding gear box)	750 g	400 g
Rotor inertia (J_m)	130 gcm^2	110 gcm^2
Speed up to	16000 RPM	8000 RPM
Torque up to	191.8 mNm	110 mNm
Current up to	8.62 A	3.8 A
Gear reduction (N)	23	43
Gear reduction efficiency (η_g)	0.8	0.7

It should be noted that, the suitable motor got through the described procedures above would not be unique since there are many motors from different companies with different types, parameters, performances and costs. For example, besides the mentioned Faulhaber 3863A024C (Motor Solution 2), another motor Faulhaber 4490H024B (Motor Solution 1) is also a suitable solution with the design requirements as shown in Table 6.3. Since the possible solution is not unique, it generates the problem of optimization. In the next section, the motor optimized selection using Mechatronic Design Quotient (MDQ) is presented.

6.2.1 Design Optimization Using Mechatronic Design Quotient (MDQ)

As a mechatronic system design involves many issues, the process can be very complex. In this section the Mechatronic Design Quotient (MDQ), proposed by C.W.

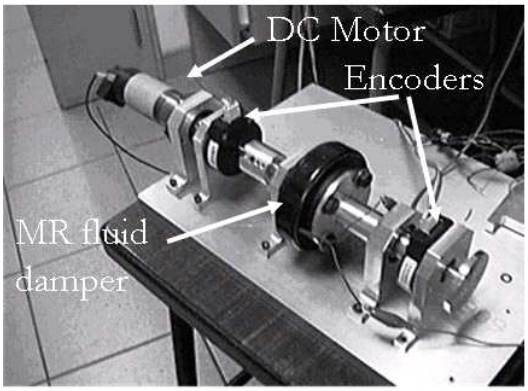

Figure 6.2: Photograph of the designed Series Damper Actuator plant

de Silva(Silva, 2004, 2005), is applied to choose an optimal design from a set of solutions. MDQ is particularly useful for a complex electro-mechanical system design. A MDQ approach would include the following steps (Lu, 2005):

- Identify the relevant design issues including the understanding the design goals, identifying the basic performance, tasks, requirements for the desired system, and figuring out what issues come under multiple design criteria.

- Establish the MDQ aspects and quantify the requirements. In this step, one should distinguish those criteria that are considered to be very important in the design, such as cost, reliability, bandwidth, weight, size, etc. After establishing the MDQ aspects, the pertinent requirements have to be quantified, and a table of target specifications should be formed.

- Establish a database for feasible designs. This step includes identifying design solutions which would roughly satisfy the basic performance requirements. All feasible solutions together form a feasible solution space.

- Assign MDQ index to each feasible design. According to each MDQ aspect, there will be a separate design index, which is a measure of the degree to which the particular design solution satisfies the design criterion. Each MDQ index also includes the importance weighting factor which indicates the importance of that particular attribute in the overall design.

- Compute the aggregate MDQ index. In this step, one incorporates all indi-

vidual design indices and associated weighting factor to obtain the value of overall MDQ index. A final decision is made by selecting the design with the highest MDQ value.

Following the steps described above, we apply the MDQ on motor selection. Motor selection is a rather complex issue. For SDA system the key design criteria include size, weight, cost, bandwidth and speed.

The flowchart of the MDQ procedures is illustrated in Fig.6.3. The requirements for the target specification has been quantified and tabulated in Tab.6.4.

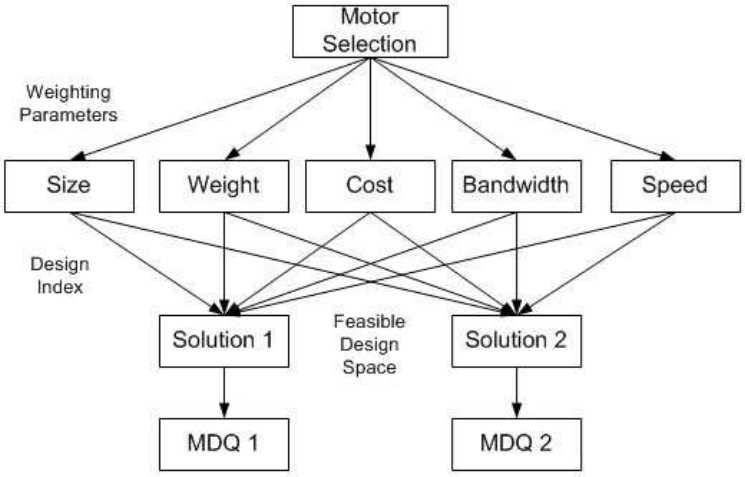

Figure 6.3: MDQ flowchart for the motor selection

Table 6.4: Target specifications for motor selection

Maximum Size	$\o 50mm \times 200mm$
Maximum Weight	$1000g$
Maximum Cost	\$ 500
Minimum Bandwidth	$11Hz$
Minimum Speed	$6000rpm$

The next step is to find the information of available commercial products and establish a database for the feasible solution space. Selecting suitable motors for the solution space would follow the nine steps described in the previous section. For simplification, only two suitable motors are used for the feasible solution space to illustrate the idea of MDQ on motor selection. The two suitable motors are

Faulhaber 3863A024C and 4490H024B as mentioned before. Then the solution space for MDQ aspects is shown in Tab.6.5.

Table 6.5: Solutions database

MDQ Aspects	**Solution 1**	**Solution 2**
Size	$ø44mm \times 168mm$	$ø38mm \times 107mm$
Weight	$750g$	$400g$
Cost	\$ 400	\$ 290
Bandwidth	$20Hz$	$13Hz$
Speed	$16000rpm$	$10000rpm$

These candidate solutions satisfy the five requirements (MDQ aspects) to different extents. We assign one index I_{mn} to each MDQ aspect to indicate the degree to which a particular solution satisfies the design criterion. m is an integer number from 1 to 5 representing these five MDQ aspects. n is an integer number of 1 or 2 representing the two candidate motors of the solution space. Furthermore, a weighting factor W_m is assigned for each MDQ aspect. In this case, we assign $W_1 = 25\%$, $W_2 = 25\%$, $W_3 = 20\%$, $W_4 = 15\%$, and $W_5 = 15\%$ to indicate size and weight are more important attributes, while bandwidth and speed are less important attributes. The total weighting factors sum up to 100%.

The MDQ indices values are assigned as shown in Tab.6.6. The important consideration is to make sure that the relative performance of each solution for each aspect is properly reflected by the relative magnitudes of the indices. To compute the MDQ index M_j for solution j, simply incorporate all the design indices and weighting factors according to following equation:

$$M_j = \frac{\sum_{i=1}^{5} W_i I_{ij}}{\sum_{i=1}^{5} W_i I_{im}} \tag{6.25}$$

Note that $0 < M_j \leq 100\%$. The results of the calculated M_j are shown in Tab.6.6.

The last step is to select the solution with the highest MDQ value as the final decision. Therefore, the second solution, that is Faulhaber 3863A024C, is the best selection among the feasible motor solutions.

Table 6.6: MDQ indices values

Design Index	**Solution 1**	**Solution 2**	**Maximum Value I_{im}**	**Weighting Parameter**
Size Index (I_1)	50%	80%	80%	25%
Weight Index (I_2)	40%	80%	80%	25%
Cost Index (I_3)	60%	80%	80%	20%
Bandwidth Index (I_4)	80%	65%	80%	15%
Speed Index (I_5)	80%	50%	80%	15%
MDQ Value (M)	73.13%	91.56%	N.A.	N.A.

In Section 6.1, a general procedure for the series damper and motor selection for the SDA plant design has been presented. It has described how we can determine, with given design requirements, the key parameters of the SDA plant, such as the damping coefficient range, component bandwidth, motor power, gear ratio, etc. Thereafter, the series damper and motor can be selected accordingly. As an example, an experimental SDA system has been successfully developed in the case study. Noted that it impossible to generate a universal standard design procedure, which is valid for every design case for SDA system. Different design case has different requirements and initial conditions. Hence, the design procedures would be different for each SDA design case. Nevertheless, the design procedures described in this section can always provide some basic guidelines for the SDA plant design. In the second half of this section, Mechatronic Design Quotient (MDQ) method is employed to optimize motor selection. MDQ provides an integrated approach for mechatronic system design. It quantifies the evaluations for all candidature solutions and therefore eases the optimization process. In fact, the application of MDQ can be extended to the design of the whole SDA system, rather than the motor selection only.

6.3 Design of A Compact MR Fluid Damper

To get a MR fluid damper, which can fit our Series Damper Actuator system, a new MR fluid damper was design and manufactured recently. In this section, the MR fluid damper design procedures were introduced in detail. FEA analysis was

employed to determine the damper's mechanical structure and parameters according to the given design targets. The damper testing experiments would be described and results were presented and discussed at the end of this section.

Magneto-Rheological (MR) fluids is one class of intelligent materials, which response to applied magnetic field with fast, continuous and reversible change in their rheological behavior. MR fluids have attracted extensive research interests recently because they can provide simple, quiet, fast-response interface between electronic control and mechanical system (Jolly, 1998). A lot of work has been done on the MR fluid property investigation, and the modeling and control of MR dampers (Lita, 2004; Spencer, 1997; Li, 2004). A wide range of MR dampers have also been investigated for their potential applications in various systems, such as, semi-active suspension systems, shock absorbers, vibration control, seismic response reduction (Dyke, 1997; Pan, 2000; Kavlicoglu, 2002; Dyke, 1996).

MR fluid damper has also been used in actuators due to its distinguished force control and power transmission features (Takesue, 2000; Stanway, 1995). In our previous work, MR fluid brake was employed to emulate a viscous damper in our proposed force control actuator system, series damper actuator (SDA) (Chew,2004-1,2004-2). By applying a proper control effort, virtual viscous damping with large varying range could be achieved with the MR fluid brake. The SDA system requires the MR fluid brake to have high transmitted torque, be compact in size, be light weight, allow 360 degree rotation, allow good connectivity, and so on. The properties of MR fluid brake determine the performance of the SDA system.

Currently there are a lot of solutions for MR fluid brake design. Some MR fluid brakes have been developed and commercialized with attractive properties, such as high yield stress and stable behavior (Lord Corporation, http://www.lord.com). Furthermore, there are also a lot of research works on the design and implementation issues of MR fluid brake, as well as its counterparts - ER brake. Carlson (Carlson, 1998) developed a controllable brake based on MR fluid. A rotary type

MR damper using valve mode was introduced by Kim (Kim, 2002). Li (Li, 2003) had designed and fabricated a high-efficiency MR brake with a simple structure. Kavlicogu (Kavlicoglu, 2002) had presented a high-torque MR fluid clutch design with double plates. A multiple discs ER brake has been proposed by Papodopoulous in (Papadopoulos, 1998). The objective of this work is to design and develop a novel MR fluid brake with high transmitted torque, compact size, light weight and good connectivity. In this thesis, a novel MR fluid brake structure with double shearing discs was presented, and the general design procedures were described. FEA simulation was performed to analyze the magnetic circuit and obtain optimized parameters for the structure. A prototype of the proposed MR fluid brake was fabricated and tested. Experimental results were presented and discussed at the end of this section.

6.3.1 Damper Structure Design and Analysis

6.3.1.1 Damper Structure

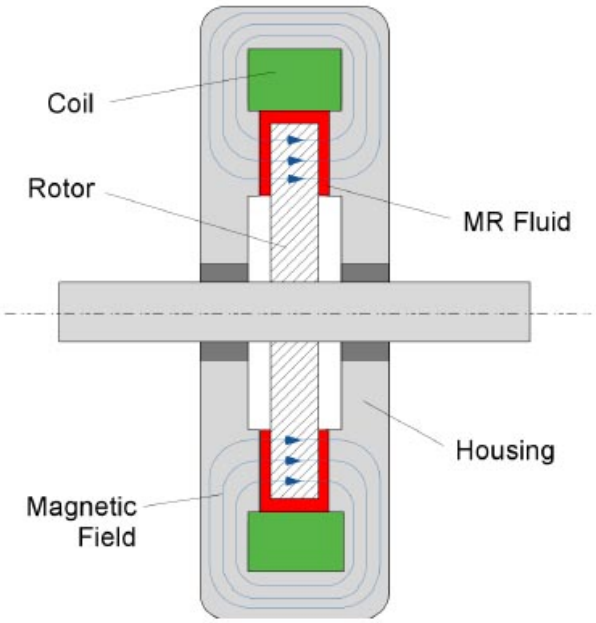

Figure 6.4: A typical structure for MR brakes (Lord Corp.)

The main objective of this design is to achieve high brake torque for a given size.

Most current solutions of MR fluid brake design come with either small transmitted torque or large size. A typical structure of MR fluid brake is as shown in Fig. 6.4. It is of a single disc type and is operated in shear mode. The electromagnet is located on the edge of the brake, and generates magnet flux penetrating the shearing disc and the MR fluid in the gap. Such configuration often results in a large radial dimension if high transmitted torque is to be achieved.

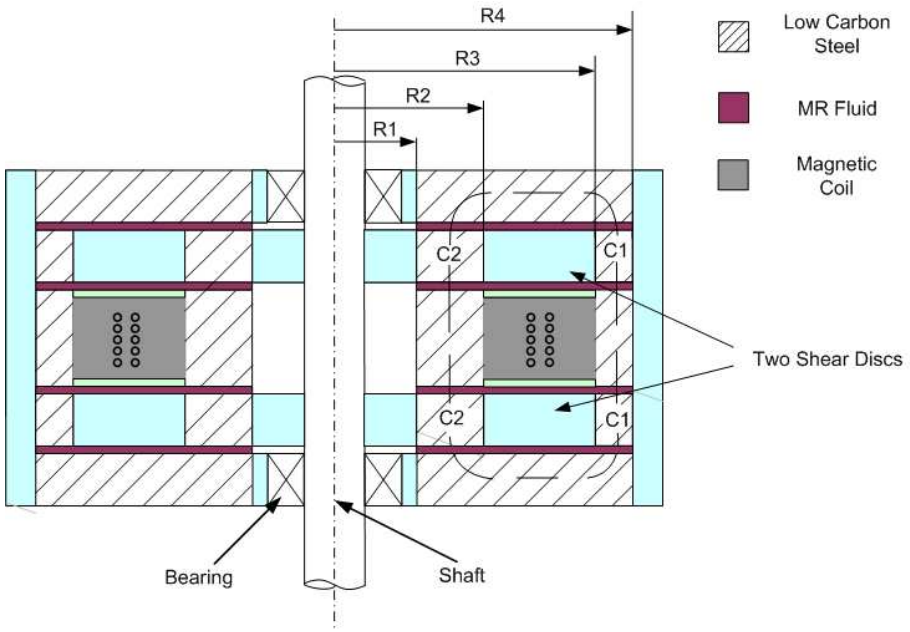

Figure 6.5: A schematic drawing of proposed MR brake structure

In Fig.6.5, a schematic of our proposed MR fluid brake structure is shown. To reduce the size of brake in this design, the electromagnet coil is shifted closer to the axis of rotation and located on one side of the shear disc. To increase the torque transmission capacity, another shear disc is added on the other side of the electromagnet coil, forming a symmetrical structure. Such a design can fully utilize the radial dimension to generate high transmitted torque. The dash line represents the magnetic flux path generated by the electromagnet coil. There are two active shear zones for each disc. They are the outer and inner shear zones, labeled by C_1 and C_2, respectively. Since each disc has two shear surfaces, there are altogether eight shear areas in the system.

6.3.1.2 Bingham Viscoplastic Model and Shear Mode Torque

MR fluid has a magnetic field dependent rheological property. The magnetic field can dramatically change the viscosity of the fluid. For example, the rheological and magnetic properties of a commercial MR fluid (MRF-241ES from Lord Corp.) are shown in Fig.6.6.

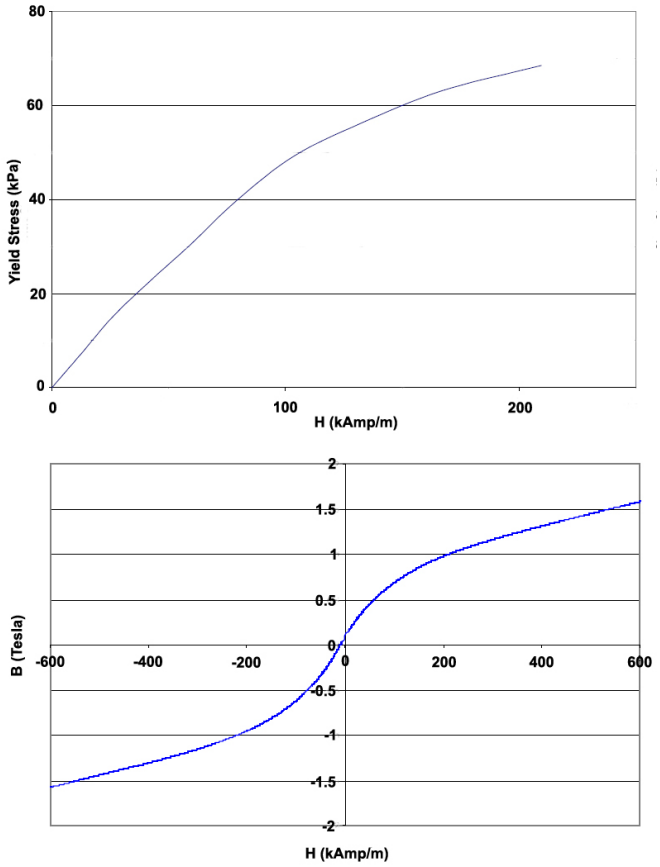

Figure 6.6: Rheological and magnetic properties of MR fluid (MRF-241ES from Lord Corp.) (a) Yield stress versus magnetic field strength (b) flux density versus magnetic field strength

The behavior of MR fluid is often represented by Bingham viscoplastic model (Spencer, 1997). The constitutive equation for the model is as follows:

$$\tau = \tau_y(H)sgn(\dot{\gamma}) + \eta\dot{\gamma} \tag{6.26}$$

where τ is shear stress, τ_y is field dependent yield stress of the MR fluid (Fig.6.6a), H

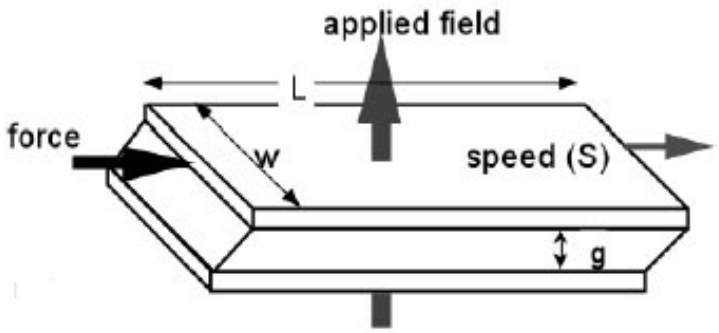

Figure 6.7: The direct shear mode of MR fluid devices

is magnetic field strength, $\dot{\gamma}$ is the shear rate, η is the plastic viscosity (i.e. viscosity at $H = 0$.)The first part of the RHS of Eq.6.26 is the yield stress produced by the magnetic field and the second part is the shear stress obtained from the fluid viscosity.

The designed brake is operated in direct shear mode as shown in Fig.6.7. In this operation mode, the force developed, F, is:

$$F = \tau_y A sgn(S) + \frac{\eta S A}{g} \tag{6.27}$$

where S is the relative shear speed, A is the shear area, and g is the gap between the two shear surface.

In this brake design as shown in Fig.6.5, there are two shear discs with two shear areas (C_1 and C_2) on each. The active shear area on one disc is shown in Fig.6.8, where ω is the angular velocity of each disc with respect to the structure, dF is the shear force generated in the small circular area with radius r and small radial increment dr, R_1 and R_2, and R_3 and R_4 are inner and outer radii of the two shearing zones C_1 and C_2 respectively. According to Eq.6.27, the generated torque can be written as:

$$T = \int_{C_1+C_2} r dF = 2\pi \int_{C_1+C_2} (\tau_y r sgn(\omega) + \frac{\omega \eta r^2}{g}) r dr \tag{6.28}$$

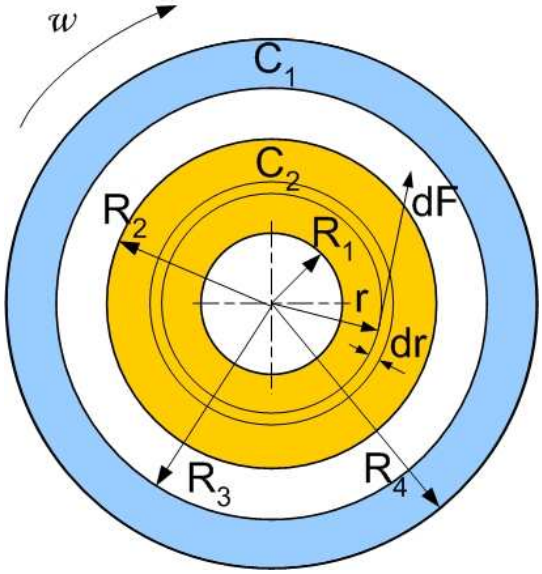

Figure 6.8: Active shear area on the shearing disc

Noted that the yield stress τ_y in the two shear area, C_1 and C_2, may not be equal. Assume that the yield stress in C_1 and C_2 are τ_{y1} and τ_{y2} respectively. Eq.6.28 can be rewritten as:

$$T = \frac{2}{3}\left[\tau_{y1}(R_2^3 - R_1^3) + \tau_{y2}(R_4^3 - R_3^3)\right] sgn(\omega) + \frac{\pi\omega\eta}{2g}\left[(R_2^4 - R_1^4) + (R_4^4 - R_3^4)\right] \tag{6.29}$$

Eq.6.29 is the shear torque generated on one surface of a shear disc. In this design, there are two shearing discs and hence four shear surfaces. That is, the effective torque for such a brake design is given by $4T$.

6.3.1.3 Magnetic Circuit Design

In our design, the electromagnetic coils are located between the two shear discs. By applying current through the coils, magnetic flux is generated along a closed path (dash line) as shown in Fig.6.5. The flux penetrates the gaps along the flux path, and therefore changes the yield stress of the MR fluid in those gaps. The target of magnetic circuit design is to determine the magnetic field excitation, amp-turns (NI), which can give desired yield stress (τ_y) of the MR fluid in the gaps. The general steps for magnetic circuit design are described as follows.

Step 1. The operation point (H_f,B_f) of MR fluid

The operation point of MR fluid is defined as the magnetic field strength (H_f) and flux density (B_f) of MR fluid in the shear gap, when the desired shear stress is obtained. According to this definition, H_f can be found from the $\tau_y - H$ curve of the MR fluid (Fig.6.6a), given the desired yield stress τ_y. Thereafter, the flux density B_f can be determined from $B - H$ curve of the MR fluid (Fig.6.6b). Alternatively, if a linear relationship between B and H is approximated for the material, the flux density can be calculated as:

$$B = u_0 u_r H \tag{6.30}$$

where u_0 is the vacuum permeability and u_r is the relative permeability of flux path material.

Step 2. The operation point (H_s, B_s)of steel

According to the principle of continuity of magnetic flux and assuming no flux leakage, it can be known that

$$\Phi_s = \Phi_f \tag{6.31}$$

where Φ_s are Φ_f are the magnetic flux in steel path and fluid gap, respectively; and,

$$\Phi_s = B_s A_s \tag{6.32}$$

$$\Phi_f = B_f A_f \tag{6.33}$$

where B_s and B_f are flux density in steel path and fluid gap, respectively; A_s and A_f are cross section area of steel path and fluid gap, respectively.

Therefore, the flux density in steel path B_s can be expressed as:

$$B_s = \frac{B_f A_f}{A_s} \tag{6.34}$$

Thereafter the magnetic field strength in the steel path, H_s, can be found from the $B - H$ curve of the steel material or from Eq.6.30. A typical curve of steel is shown in Fig.6.9.

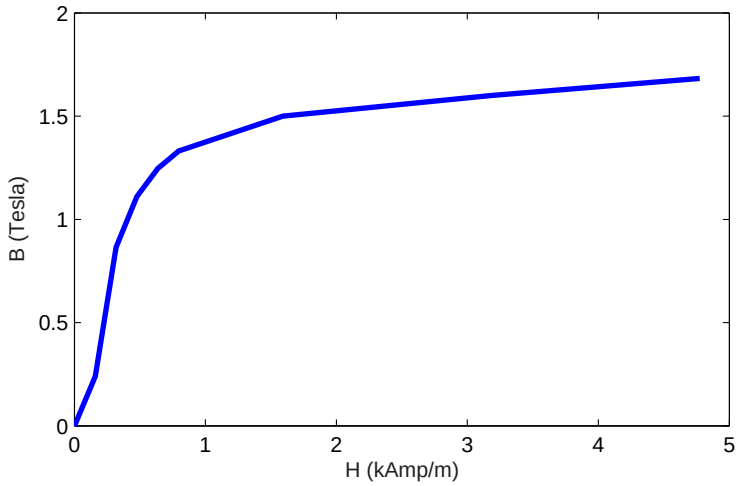

Figure 6.9: A typical $B-H$ curve of steel

Step 3. Magnetic circuit excitation, amp-turns (NI)

Applying the magnetic circuit Kirchhoff's Law gives that:

$$NI = H_f g + H_s L \tag{6.35}$$

where N is the number of coil turns; I is the coil current; g is the gap length; and L is the length of the steel path.

If there are n MR fluid gaps and m steel path sections series connected in the closed magnetic circuit, then Eq.6.35 can be written as:

$$NI = \sum_{i=1}^{n} H_{if} g_i + \sum_{j=1}^{m} H_{js} L_j \tag{6.36}$$

where H_{if} is the H_f in ith fluid gap and H_{js} is the H_s in jth steel path.

Because the relative permeability (u_r in Eq.6.30) of steel is far larger than that of MR fluid, the magnetic field strength in steel H_s is usually much lower than that in MR fluid gap H_f, that is $\sum_{j=1}^{m} H_{js} L_j$ can be neglected in Eq.6.36. Then it gives that

$$NI = \sum_{i=1}^{n} H_{if} g_i \tag{6.37}$$

If all MR fluid gaps have same gap length g and magnetic field strength H_f, the

above equation can be further simplified as:

$$NI = nH_f g \tag{6.38}$$

The above equations enable the designers to estimate the required magnetic field excitation, NI (amp-turns), given required magnetic field strength and certain flux path dimensions. However getting an accurate magnetic circuit design using the method described above is very difficult due to the nonlinear properties of materials (see Fig.6.6 and Fig.6.9) and some other nonidealities, such as flux leakage, and flux path dimension uncertainties. Finite element analysis software is used to aid the optimization process of the magnetic design. The three steps of the magnetic circuit design described above should be performed before the FEA analysis and optimization. Although the calculated magnetic excitation NI may not be accurate, it can be used as an initial condition for the FEA analysis and then adjusted accordingly.

6.3.1.4 FEA analysis and design optimization

Electromagnetic finite element analysis is performed in this work to assist the electromagnetic circuit design and optimize the brake's structural parameters. The FEA simulation software used in this work is the 2D Maxwell from ANSOFT.

The FEA 2D model geometry (in the RZ plane of a cylindrical coordinate system) is shown in Fig.6.10. The model is actually a 3D axisymmetric object. The 2D diagram represents a 3D structure that has been revolved around the axis of symmetry (Z axis). 2D Maxwell analyzes the 2D geometry as a cross-section of the model and generates a solution for that cross-section.

An example of the FEA simulation result is shown in Fig.6.11. The flux density (the closed curves) and the gap magnetic field strength (scaled color) are displayed in the result. The magnetic path is clearly indicated by the flux curves and some flux leakage can also be observed. From the simulation result, the magnetic field strength in MR fluid gap (H_f) can be obtained for all the eight gaps in the closed magnetic path. Then, the generated shearing torque can be calculated according

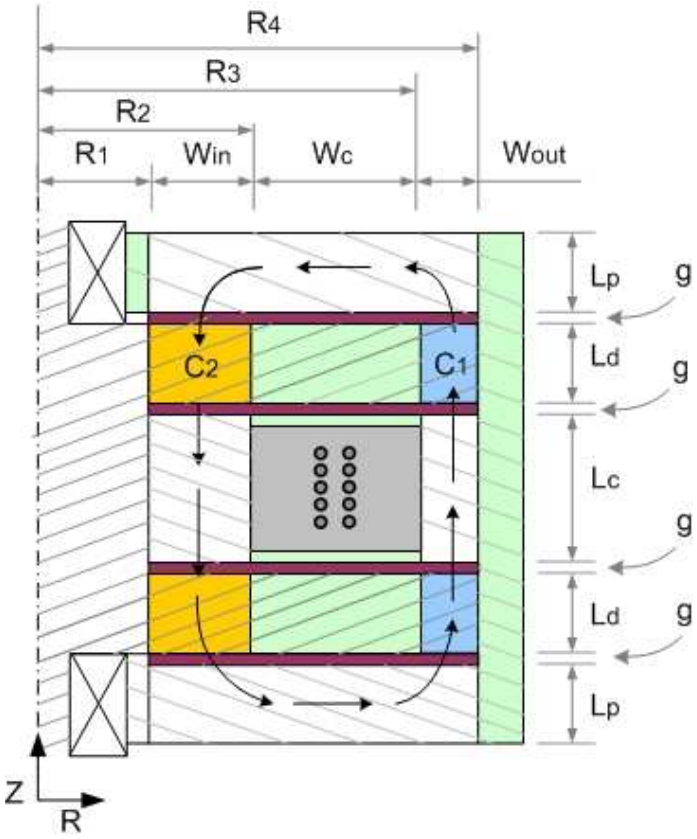

Figure 6.10: The 2D FEA model of the designed double discs MR fluid brake

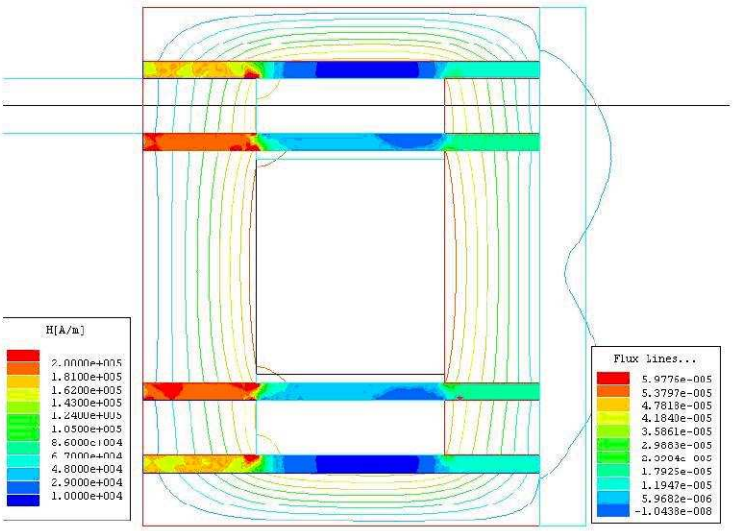

Figure 6.11: An example of FEA simulation results

to Eq.6.29. The simulation results, therefore, can be used to evaluate the magnetic circuit design described in the previous subsection. The magnetic circuit excitation NI can be adjusted till satisfactory yield stresses in these gaps are obtained. Furthermore, the FEA analysis results can also be used to evaluate the brake structural design and optimize its dimensional parameters.

Important parameters have also been indicated in Fig.6.10, where

R_1, R_2, R_3, R_4 are inner and outer radii of two shearing area C_1 and C_2 respectively,
L_p is the thickness of side steel path,
L_d is the thickness of shearing disc,
L_c and W_c are length and width of magnet coil respectively,
W_{in} and W_{out} are the width of inner and outer steel path,
g is the MR fluid gap length.
R_4 and R_1 decide the active shear area of the MR fluid. Therefore, to obtain large torque transmission capability, large R_4 and small R_1 is always preferred. R_4 can be determined according to the maximum permitted brake size, usually, from the design requirements. R_1 can be determined from the minimum shaft size required from the aspects of component strength, manufacturing and assembling, and so on. Satisfying the disc strength and manufacturing requirements, the thickness of shearing disc, L_d, should be as small as possible to reduce the weight and size of brake and lower the flux strength loss in the steel path. L_c and W_c can be determined from the coil size by considering the wire diameter and number of turns.

The optimization of the structure parameters, g, L_p, W_{in} and W_{out} is briefly discussed below.

- *Gap Length g*

According to Eq.6.36, it can be known that the gap length g is known to significantly affect the magnetic field strength (H). A simulation result of the relationship between the gap length and the magnetic field strength in this gap is shown in Fig.6.12. It can be seen that a smaller gap gives a larger magnetic field strength. Generally, a larger magnetic field strength will result in a larger yield stress for MR fluid and, consequently, generate a larger transmitted torque. If MR fluid operation points are given, smaller gap always means smaller requirement for amp-turns, NI. In this sense, a smaller gap will be better. However, the gap cannot be too small, considering the manufacturing and assembling errors. And the smaller the gap is, the more sensitive the magnetic field strength H is to gap errors (see Fig.6.12). Usually, the gap length is between 0.25mm to 2mm for ease of manufacture and assembly (Li, 2003; Yoo, 2002). In this design, the gap is set to 1mm.

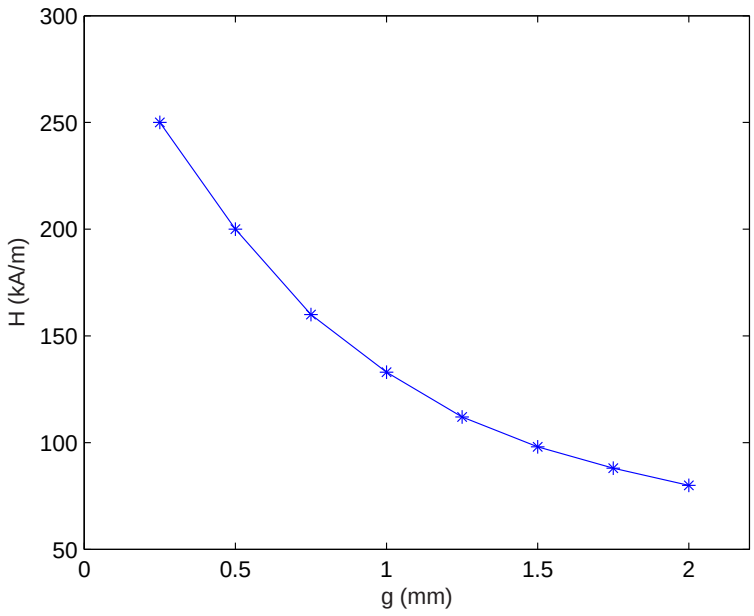

Figure 6.12: A simulation result for the gap length (g) versus the magnetic field strength (H) in this gap

- *Width of inner and outer flux path W_{in} and W_{out}*

W_{out} and W_{in} are the radial width of shear areas C_1 and C_2, respectively. They also represent the width of outer and inner flux path, respectively. When R_1, R_4 and W_c are given, the summation of W_{in} and W_{out} will be fixed because:

$$W_{in} + Wout = R_4 - R_1 - W_c \tag{6.39}$$

Therefore, increasing W_{in} will decrease W_{out}, and vice versa. W_{in} and W_{out} will determine the area of the two shear region C_1 and C_2. Large area of C_1 may be preferred since it is at larger radius than C_2 and therefore may result in higher transmitted torque. However, large W_{out} will result in a small shear area for C_2. Furthermore, a small W_{in} may result in magnetic saturation in the steel path. When magnetic path is saturated, the path flux density would not have significant response to the change of magnetic circuit excitation, and consequently the magnetic field strength in the MR fluid gap would be limited to a relatively low level. Therefore, to achieve large transmitted torque, the optimal values for W_{in} and W_{out} should be found from FEA simulation.

A simulation result is presented in Fig.6.13, which shows the effect of different values of W_{in} and W_{out} on the transmitted brake torque. In this example, $W_{in} + W_{out} = 11mm$ according to Eq.6.39, where R_1, R_4 and W_c are given as 9mm, 30mm and 10mm, respectively. The brake torque is simulated with (W_{in}, W_{out}) varying from ($4mm$, $7mm$) to ($10mm$, $1mm$). On the horizontal axis, from left to right, the W_{in} increases from $4mm$ to $10mm$, and W_{out}, correspondingly, decreases from $7mm$ to $1mm$. It can be seen in Fig.6.13 that, if $W_{in} < 5mm$ or $W_{in} > 9mm$, the brake generated torque T will be relatively low. The generated torque reaches maximum value when (W_{in}, W_{out}) is ($6mm$, $5mm$) and decreases slowly when W_{in} increases. That is, (W_{in}, W_{out}) = ($6mm$, $5mm$) would be optimal in terms of maximum toruqe. However, parameter sensitivity should also be considered. It can be seen from Fig.6.13,

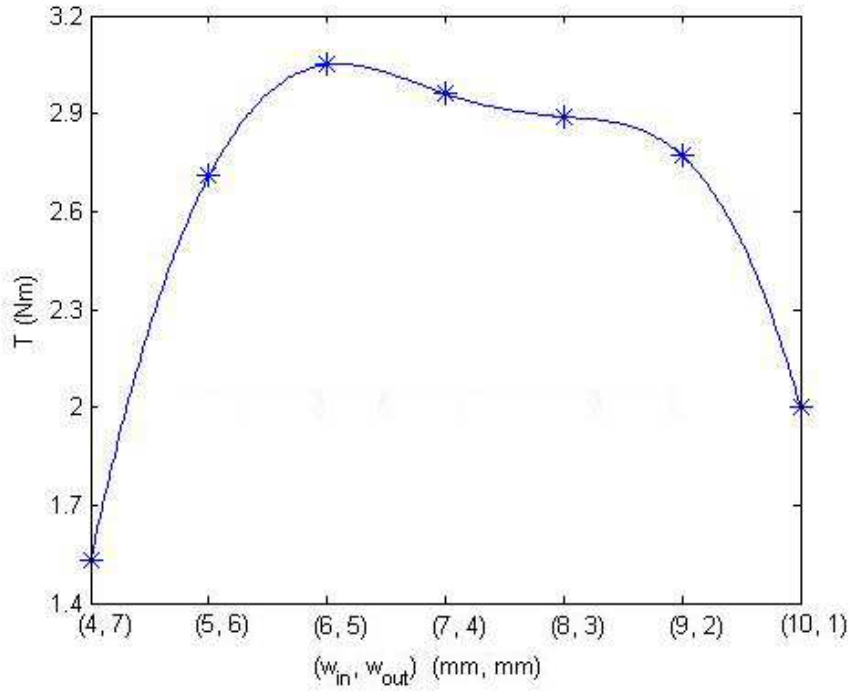

Figure 6.13: The brake transmitted torque T with different inner flux path width W_{in} and outer flux path width W_{out}

when $W_{in} < 6mm$, the generated torque drops sharply with the reducing of the W_in and therefore has large sensitivity to the dimension error. Whereas, when $6mm < W_{in} < 7mm$, the curve is relatively flat and less sensitive to the changes of W_{in} and W_{out}. Therefore, (W_{in}, W_{out}) is preferred to be between $(6mm, 5mm)$ and ($7mm$, $4mm$).

after W_{in} and W_{out} are decided, R_2 and R_3 can be computed as follows:

$$R_2 = R_1 + W_{in} \tag{6.40}$$

$$R_3 = R_4 - W_{out} \tag{6.41}$$

- *Side steel path thickness L_p*

  To reduce the weight and size of the brake, the thickness of side steel path, L_p, is expected to be as small as possible. However, if the thickness is too small, it will cause magnetic saturation and consequently reduce the magnetic

field strength in both shear areas, C_1 and C_2. Therefore, the optimal L_p is the smallest value where the magnetic saturation does not happen.

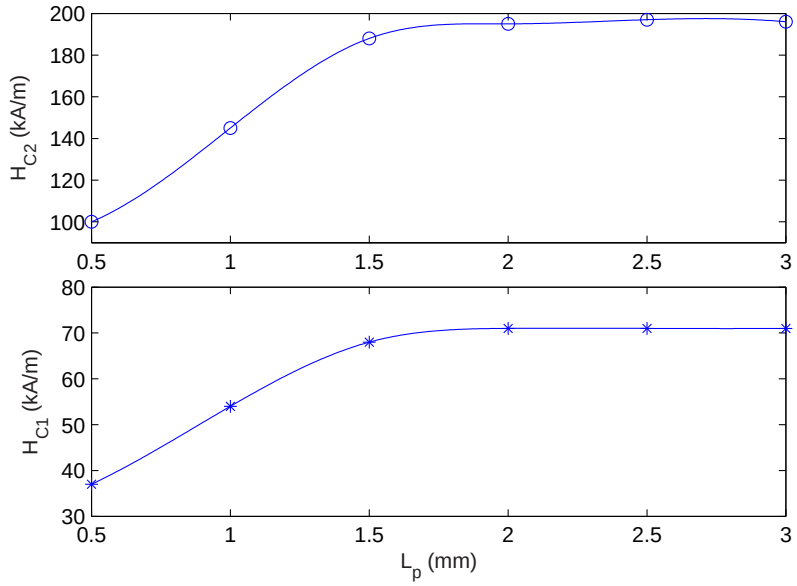

Figure 6.14: Magnetic field strength (H) at shear area C_1 and C_2 versus the thickness of side steel path (L_p)

A simulation study of the particular design example which shows how the magnetic field strength at shear areas varies with L_p is shown in Fig.6.14. From the study, it is observed that, when $L_p < 1.5mm$, the magnetic field strength in MR fluid gaps will drop significantly with decreasing L_p. Therefore, to reduce weight and at the same time avoid magnetic saturation, a value between 1.5mm and 2mm for L_p would be optimal for this particular design example.

The Above analysis gives a general description of the brake design and the parameters optimization with the assistance of FEA analysis. Note that the parameters optimizations are not conducted in sequence. Some design iterations are needed before the most optimal result can be obtained.

6.3.2 Design Results and Experimental Setup

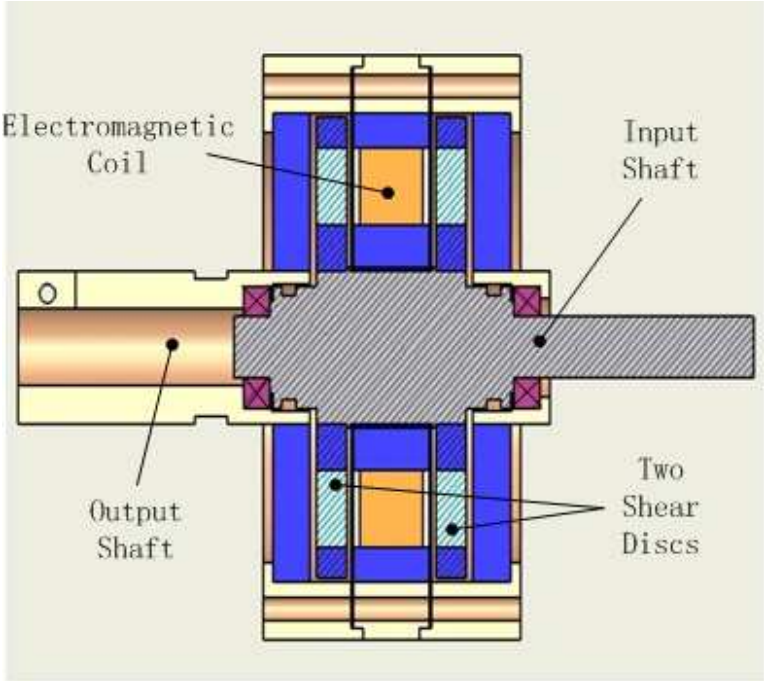

Figure 6.15: A sectional view of the designed MR brake

A CAD drawing of the final design of the MR fluid brake is shown in Fig.6.15. There are an input and an output shafts in the design. The input and the output shafts can rotate independently. Two shearing discs are connected to the input shaft. The transmitted brake torque is passed to the output shaft through the body of the brake. The magnetic coil is placed between the two shear discs to reduce the radial size. Double shear discs also result in more shear area than that of a single one. This design results in higher torque transmission capacity of the brake. The key specifications of the MR fluid brake prototype are shown in Table 6.7.

An experimental setup as shown in Fig.6.16 is also built to test the MR fluid brake prototype. A DC motor is connected to the input shaft of the MR fluid brake to provide the input angular velocity. An encoder is attached to the motor to measure this angular velocity. This will be the shearing angular velocity if the output shaft is stationary. A torque sensor is mounted at the output shaft to measure the transmitted torque. A micro-computer (PC104) is used to control the DC motor

Table 6.7: The key specifications of the MR fluid brake prototype

Maximum output	$3.5Nm$
Mechanical Dimension	$\oslash 76mm * 40mm$
Weight	$910g$
Wire diameter	$\oslash 0.315mm$
Number of turns	700
Shear gap	$1mm$
Effective fluid volume	$12ml$
MR fluid	Water based MR fluid (MRF-241ES)
Magnetic material	Low carbon steel (AISI-1018)
Non-magnetic material	Aluminum Alloy
Sealing	O-ring (rubber)

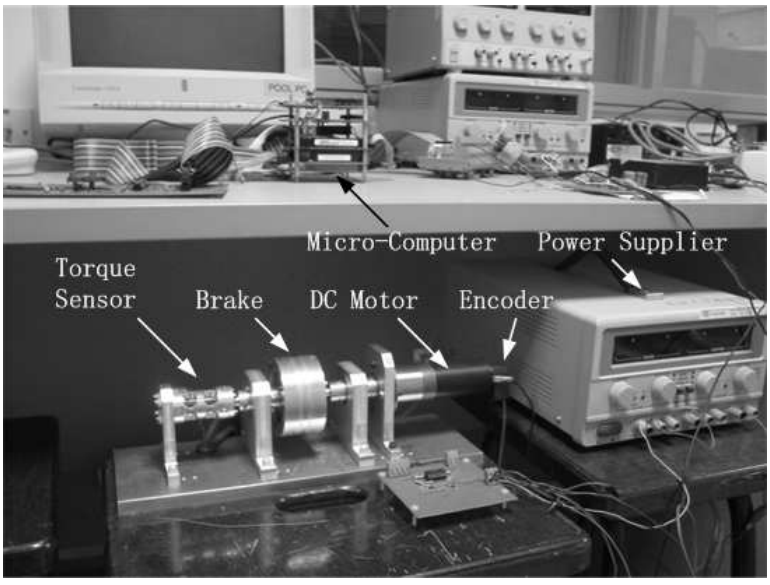

Figure 6.16: A picture of the experimental system

based on the feedback from the encoder; read and record the transmitted brake torque from the torque sensor. A DC power supply is used to provide the input current to magnetic coil of the MR fluid brake.

6.3.3 Test Experiments and Results

Two experiments were conducted for the MR fluid brake prototype. In the first experiment, the brake velocity was kept constant and the transmitted torque was measured with different current applied to the magnetic coil of the brake. This experiment was to show the relationship between the brake's transmitted torque and input current. Two velocities (3rad/s) were used while the input current varied from 0 to 0.8A. The negative velocity was used to show the asymmetric property of the brake's transmitted torque.

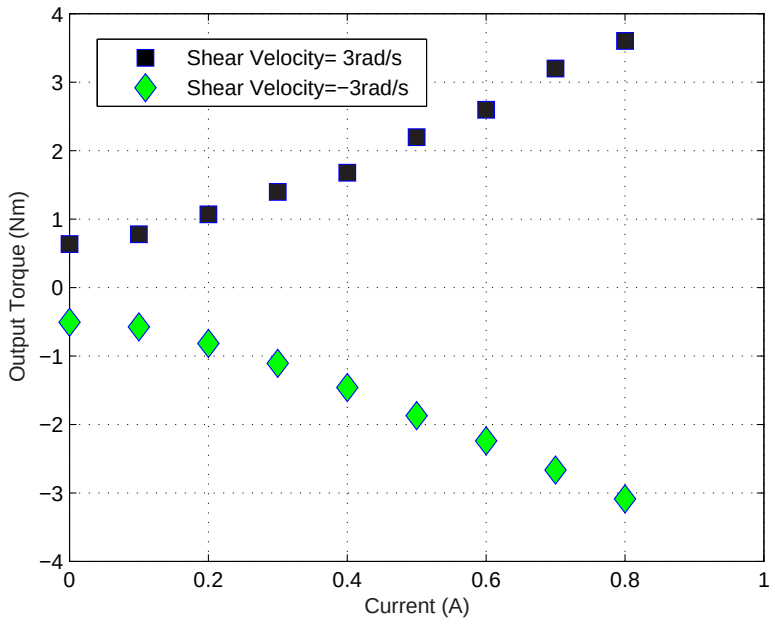

Figure 6.17: The output torque of MR damper with different constant damper velocity and different constant current

The experimental results are shown in Fig. 6.17. From Fig.6.17, it can be observed that the maximum transmitted torque is around 3.5 Nm when the applied

current is 0.8A. The brake has good linear relationship between the transmitted torque and the input current, especially when the current is larger than 0.1A. The transmitted torque also behaves rather symmetrically. That is, its magnitude remains the same if the velocity of the brake changes its sign (from 3 rad/s to -3 rad/s). When there is no current applied to the brake, the transmitted torque is around 0.55 Nm, which is about 15.7% of the maximum brake torque. This residual torque is mainly attributed to several sources. One of which is the residual shearing torque due to the residual viscosity of the MR fluid. Another important source is due to the friction in the sliding contacts in the brake, for example, at the location where the rubber o-ring used for MR fluid sealing is situated. Some of these friction sources can be reduced by changing the materials. For the case of the o-ring, as the rubber has relatively large friction coefficient when rubbed against another material, it may be better to use another sealing material such as polymer, which has significantly reduced friction coefficient.

In the second experiment, the brake's current was kept constant while a sinusoidal brake velocity was maintained. During the experiment, the transmitted torque was recorded. This experiment was used to study the properties of the MR fluid brake prototype, such as the hysteresis effect, the fluid viscous property, etc.

The sinusoidal brake velocity had amplitude of 4 rad/s and frequency of 0.5Hz. The applied currents were 0.2A, 0.4A, 0.6A and 0.8A. The experimental results are presented in Fig.6.18. The results show the typical hysteresis behavior of the MR fluid brake. The hysteresis region is within +/-1 rad/s. The hysteresis comes from the inherent property of MR fluid brake. It is also observed that the brake torque, beyond the hysteresis region, is nearly constant and not dependent on the brake velocity. This means that the viscous component in the dynamics of the MR fluid brake can be neglected.

In Section 6.3, a novel MR fluid brake with double shearing discs was proposed, designed and tested. The brake structure was introduced and Bingham model was used to predict the brake transmitted torque. General steps for the magnet circuit

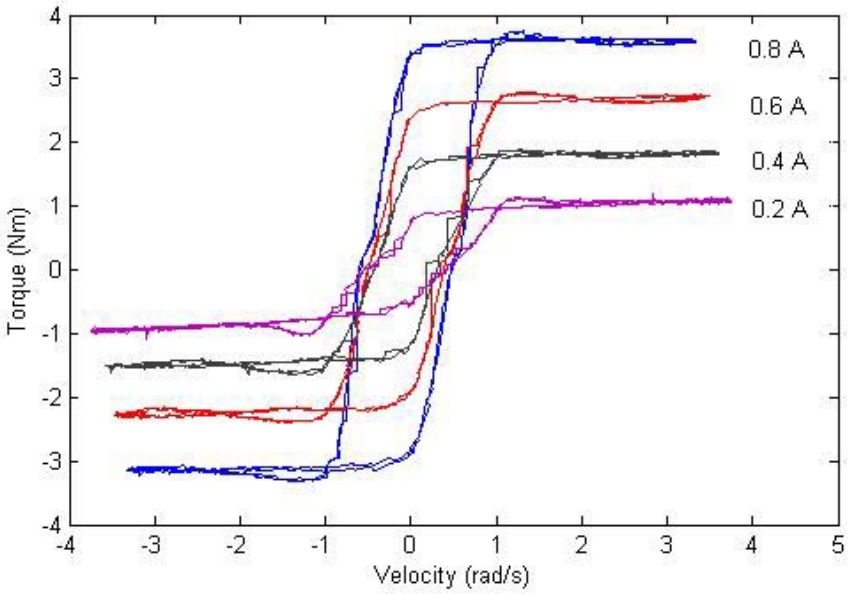

Figure 6.18: The output torque of MR damper with sinusoidal damper velocity and different constant current

design were described. Brake's structural parameters, such as the width of the inner and outer flux path, the thickness of the side steel path, etc., were optimized with the assistance of FEA analysis simulation. A MR fluid brake prototype was manufactured and a testing system was built to evaluate the performances of the brake. Experimental results show that a compact MR fluid brake with high transmitted torque was successfully developed.

6.4 Summary

This chapter mainly investigated the hardware design problems of SDA plant, including component selections, optimization and the design of a compact MR fluid damper.

In the first section of this chapter, the SDA design procedures for the damper and motor selections are described. Then, the motor optimized selection is carried out based on Mechatronic Design Quotient (MDQ).

The second section of this chapter introduced in detail the design process of a

novel MR fluid damper with a compact size. A prototype had been built and tested. The experimental testing results of the new MR fluid damper were presented to show its properties and performances.

Chapter 7

Conclusion

The overall objective of this thesis was to design, analyze, and develop force control actuator system - Series Damper Actuator (SDA) to obtain good force fidelity, low output impedance and high system bandwidth and, at same time, ease the design tradeoffs that existed in the Series Elastic Actuator (SEA) system.

7.1 Summary of Results

In this thesis a novel force control actuator, Series Damper Actuator (SDA) was proposed. In Chapter 3, SDA system has been modelled and analyzed by comparing with the SEA system in terms of system bandwidth, output impedance, system efficiency, and impact tolerance ability. It was shown that the SDA system would have good force control fidelity, large bandwidth, low output impedance and high impact tolerance ability. Adopting variable damping coefficient, the SDA system can obtain broad output force range and ease the design trade-off. Experimental setup has been built and Magneto-Rheological (MR) fluid damper was employed as the series damper. A PID controller was proposed and variable damping coefficient was achieved with a damper linearization algorithm. Experimental results showed that the SDA system has a high force control fidelity, low output impedance, large force range, and high impact tolerance ability. However, the bandwidth observed from experiments were lower than that from theoretical analysis.

To reveal the reason, in Chapter 4, the SDA model was rebuilt by considering the extra dynamics introduced by the MR fluid damper. In the analysis, Bingham model was employed to represent the basic dynamics of MR damper and a first order model was adopted to model the current response dynamics of MR damper. The analysis results showed that the extra dynamics of MR damper increased the order of SDA system, and consequently limited the bandwidth of SDA system, especially when the current response of MR damper was slow. It explained the low bandwidth reported in Chapter 3.

With the knowledge of the SDA based on MR fluid damper we had obtain from the above work, a more advanced controller was designed, in Chapter 5, to compensate the extra dynamics of MR fluid damper and therefore give the SDA system a better force control performance. Inverse dynamics control schemes were developed for the linearization of the MR fluid damper. To implement this kind of controller, a modified Bingham model for the MR fluid damper was proposed and compared with the two very popular MR fluid models, Bingham model and the Bouc-Wen model. Model comparison was done in terms of model accuracy and model invertibility. Simulation and experimental results showed that the proposed model is more suitable to implement inverse dynamics control for the MR fluid damper based SDA system. With the proposed control schemes, higher force fidelity and larger system bandwidth had been achieved comparing with the results shown in Chapter 3.

Chapter 6 addressed on the hardware design of the SDA system, including plant component selections, optimization and the design of a compact MR fluid damper. The SDA design procedures for the damper and motor selections are described. Then, the motor optimized selection is carried out based on Mechatronic Design Quotient (MDQ). Thereafter, the design process of a novel MR fluid damper with a compact size was introduced. Damper double-disc structure was presented and optimized with the FEA analysis results. A prototype had been built and tested. The experimental testing results of the new MR fluid damper were presented to show its properties and performances.

7.2 Future Works

There are several interesting directions for the further work related to this research. In this thesis, both viscous damper and MR damper were proposed to serve as the series damper in the SDA system. The damper used in the experimental systems was a MR fluid damper. And the design of a MR fluid damper was also introduced. But viscous damper structure design was not covered in this thesis. Most of the available viscous dampers in current market, especially the rotary type viscous dampers, are not suitable for SDA system due to some problems such as low output force range, and relative position limitation. In the SDA system, the damper is required to have a compact size, large output force/torque and no relative position limitation for rotary type damper. These requirements are quite challenging for the damper design. However, a novel damper design can potentially increase the capacity and performance of SDA system and extend its potential applications in a variety of fields, such as micro-robots and telesurgery operation.

In the thesis, the controller design has been discussed, a general controller for SDA system was presented and an inverse dynamics controller was proposed for the MR damper based SDA system using a modified Bingham model. Although Bingham model is a very popular model to describe the dynamics of MR fluid damper, it doesn't include the hysteresis effect, which is prevalent for MR fluid dampers and sometimes dominant, especially when frequency is high. Therefore models, such as Luge model and Bouc Wen model, in which the hysteresis effect is considered, can be adopted to implement the proposed inverse dynamics control and may give better results. Furthermore, other advanced control theories may be applied to control MR fluid damper. Adaptive control and robust control have been reported for the semi-active control of MR damper. The application of these advanced control theories for the fully active control of the MR damper based SDA system would be relatively complex but seems quite promising in terms of obtaining better performance. Therefore this application gives a possible direction for research on force control actuators.

The applications of SDA system for force control are quite broad as described in the beginning of this thesis. This thesis only focuses on the development of SDA system rather than the applications of such system. However, the application of SDA system to replace SEA or other conventional force control methods in the system, such as Micro Macro Motor Actuator system, needs more investigations to determine the overall performance of the system in terms of bandwidth, impact tolerance ability and output impedance. Due to the clutch function of the MR fluid damper, the SDA system can be used to achieve force/position hybrid control with a promising force/position switch performance. Furthermore, the SDA system has a virtual damping coefficient and therefore can be used to build a stable haptic system based on passive theory, in which effective system virtual damping control is necessary and important to guarantee the system stability and obtain desired performance.

At the end of our project, another novel concept of force control actuator, called Series Component Actuator (SCA), was proposed. Instead of the spring and the damper as the series component in SEA and SDA system respectively, the SCA uses other kind of material as the series component, such as rubber or elastomer, which has both the elastic and damping properties. The new series component in the SCA system is equivalent to a parallel connection of a spring and a damper in modelling. General analysis has showed a lot of compromising properties of such actuator system. However, a systematical work should be done on system modelling and analysis, controller design, experimental setup building and testing and so on. Therefore, the SCA system would be another area worthy of the future research on force control actuators.

References

Abidi K., Sabanovic A. and Yesilyurt S. *Sliding-Mode Based Force Control of a Piezoelectric Actuator.* IEEE International Conference on Mechatronics, Istanbul, Turkey, pp: 104-108, 2004.

Antonelli G., Chiaverini S. and Sarkar N. *External Force Control for Underwater Vehicle-Manipulator Systems.* IEEE Transactions on Robotics and Automation, Vol. 17, No. 6, pp: 931-938, 2001.

Anderson R.J. and Spong M.W. *Hybrid Impedance Control of Robotic Manipulators.* IEEE Journal of Robotics and Automation, Vol. 4, No. 5, 1988.

Bojan N. and Leon Z. *Force Control of Redundant Robots in Unstructured Environment.* IEEE Transactions on Industrial Electronics, Vol. 49, No. 1, pp: 233-240, 2002.

Ben-Dov D. and Salcudean S.E. *A Force-Controlled Pneumatic Actuator.* IEEE Transactions on Robotics and Automation, Vol. 11, No. 6, pp: 906-911, 1995.

Budiman E.S. and Tomizuka M. *Position/Force Control with a Frequency-Based Switch for Robots Interacting with a Compliant Environment.* IEEE/ASME International Conference on Advanced Intelligent Mechatronics, Atlanta, USA, pp: 973-978, 1999.

Caldwell D.G., Tsagarakis N., Artrit P., Canderle J., Davis S. and Medrano-Cerda G.A. *Biomimetic and Smart Technology Principles of Humanoid Design.* IEEE/ASME International Conference on Advanced Intelligent Mechatronics, Como, Italy, pp: 965-970, 2001.

Carignan C.R. and Cleary K.R. *Closed-Loop Force Control for Haptic Simulation of Virtual Environments.* Haptics-e, Vol. 1, No. 2, February 23, 2000.

Carlson J.D., Catanzarite D.M. and Clair K.A. St. *Commercial Magneto-Rheological Fluid Devices.* International Journal of Modern Physics B, pp: 2857-2865, 1996.

Carlson J.D., LeRoy D.F., Holzheimer J.C. and Marjoram R.H. *Controllable Brake.* United States Patent, Patent Number: 5842547, 1998.

Cetinkunt S. and Wu S. *Tip Position Control of a Flexible One Arm Robot with Predictive Adaptive Output Feedback Implemented with Lattice Filter Parameter Identifier.* IEEE International Conference on Robotics and Automation, Cincinnati, USA, pp: 1620-1625, 1990.

Chew C.-M., Hong G.-S. and Zhou W. *Damper System.* US Patent Application. Application No.: 10/845787, 2004.

Chew C.-M., Hong G.-S. and Zhou W. *Series Damper Actuator: A Novel Force/Torque Control Actuator.* IEEE-RAS/RSJ International Conference on Humanoid Robots, Los Angeles, CA, USA, pp:533-546, 2004.

Chew C.-M., Hong G.-S. and Zhou W. *Series Damper Actuator System Based on MR Fluid Damper.* Robotica, Vol. 24, No. 6, pp:699-710, 2006.

Chiharu S., Hiromitsu O. and Akira S. *Modeling of MR Damper with Hysteresis for Adaptive Vibration Control.* Proceedings of the 24nd IEEE Conference on Decision and Control, Hawaii, USA, pp: 3840-3845, 2003.

Cho C., Kim M. and Song J.B. *Direct Control of a Passive Haptic Device Based on Passive Force Manipulability Ellipsoid Analysis.* International Journal of Control, Automation, and Systems, Vol. 2, No. 2, 2004.

Colgate E. and Hogan N. *An analysis of Contact Instability in Terms of Passive Equivalents.* IEEE International Conference on Robotics and Automation, Scottsdale, USA, pp:404-409, 1989.

Cortesao R., Koeppe R., Nunes U. and Hirzinger G. *Explicit Force Control for Manipulators with Active Observers.* Proceedings of the 2000 IEEE/RSJ International Conference on Intelligent Robots and Systems, Takamatsu, Japan, pp: 1075-1080, 2000.

Dieter V. and Oussama K. *Design and Development of High-Performance Torque-Controlled Joints.* IEEE Transactions on Robotics and Automation, Vol. 11, NO. 4, 1995.

Dorf R.C. and Bishop R.H. *Modern Control Systems.* Pearson Education, Eighth Edition, 2004.

Dyke S.J., Spencer B.F., Sain M.K. and Carlson J.D. *Modeling and Control of Magnetorheological Dampers for Seismic Response Reduction.* Smart. Materials and Structures, Vol. 5, pp: 565-575, 1996.

Dyke, S.J. and Spencer, B.F. *A Comparison of Semi-Active Control Strategies for the MR Damper.* Proceedings of Intelligent Information Systems, IIS'97, Grand Bahama Island, Bahamas, pp: 580-584, 1997.

Erika O., Maria T. and Marco C. *Grasp Force Control in Two-Finger Grippers with Pneumatic Actuation.* Proceedings of 2000 IEEE Internatinal Conference on Robotics and Automation, San Francisco, USA, pp: 1976-1981, 2000.

Gene F. Franklin, J. David Powell and Michael Workman. *Digital Control of Dynamic Systems.* Addison-Wesley, 1998.

Gevarter W. B. *Basice Relations for Control of Flexible Vehicles.* AIAA Journal, Vol. 8, No. 4, 1970.

Goldsmith P.B., Francis B.A. and Goldenberg A.A. *Stability of Hybrid Position/Force Control Applied to Manipulators with Flexible Joints.* International Journal of Robotics and Automation, Vol. 14, No. 4, 1999.

Gorinevsky D.M., Formalsky A.M. and Schneider A.Y. *Force Control of Robotics System*. CRC Press, New York, 1997.

Goswami A. and Peshkin M.A. *Implementation of Passive Force Control with Redundant Manipulators*. IEEE International Conference on Systems, Man and Cybernetics, Charlottesvill, USA, pp: 949-954, 1991

Goswami A. and Peshkin M.A. *Mechanical Computation for Passive Force Control*. IEEE International Conference on Robotics and Automation, Atlanta, USA, pp: 476-483, 1993

Grant D. and Hayward V. *Constrained Force Control of Shape Memory Alloy Actuators*. Proceedings of 2000 IEEE Internatinal Conference on Robotics and Automation, San Francisco, USA, pp: 1314-1320, 2000.

Hogan N. *Impedance Control: An Approach to Manipulation: Part I - Theory, Part II - Implementation, Part III - Applications*. Journal of Dynamics Systems, Measurement and Control, pp: 1-24, 1985.

John S. Bay. *Fundamentals of Linear State Space Systems*. McGraw-Hill, 1999.

Jolly M.R., Bender J.W. and Carlson J.D. *Properties and Applications of Commercial Magnetorheological Fluids*. SPIE 5th International Symposium Smart Structures and Materials, San Diego, USA, pp: 262-275, 1998.

Jong H.P. and Hoam C. *Hybrid Control for Biped Robots Using Impedance Control and Computed-Torque Control*. IEEE International Conference on Robotics and Automation, Detroit, USA, pp: 1365-1370, 1999.

Katsuhiko Ogata. *Modern Control Engineering*. Fourth Edition, Prentice Hall, 2002.

Kavlicoglu B.M., Gordaninejad F., Evernsel C.A., Cobanoglu N., Liu Y., Fuchs A. and Korol G. *A High-Torque Magneto-Rheological Fluid Clutch*. SPIE Conference on Smart Materials and Structures, San Diego, USA, pp: 393-400, 2002.

Kazanzides P., Bradley N.S. and Wolovich W.A. *Dual-drive force/velocity control: implementation and experimental results*. IEEE International Conference on Robotics and Automation, Scottsdale, USA, pp: 92-97, Vol.1, 1989.

Kazerooni H. *Pneumatic Force Control for Robotic Systems*. IEEE International Conference on Mechatronics, Istanbul, Turkey, pp: 231-236, 2004.

Kim J.H. and Oh J.H. *Design and Analysis of Rotary MR Damper Using Permanent Magnet*. Proceedings of 2nd IFAC Conference on Mechatronic Systems,Berkeley, USA, pp: 899-903, 2002.

Kuntze H.B., Jacubasch A., Hirsch U., Richalet J., Arber C. *On the Application of a New Method for Fast and Robust Position Control of Industrial Robots*. IEEE International Conference on Robotics and Automation, Philadelphia, USA, pp: 1574-1580, 24-29 April 1988.

Lee D.Y. and Cho H. *Precision Force Control via Macro/Micro Actuator for Surface Mounting System*. IEEE International Conference on Intelligent Robotics and System, Vol.3, Lausanne, Switzerland, pp: 2227-2232, 2002.

Li W.H. and Du H. *Design and Experimental Evaluation of a Magnetorheological Brake*. International Journal Manufacture Technology, Vol. 21, pp: 508-515, 2003.

Li H.N. and Chiang Z.G. *Intelligent Algorithm Based Semi-Active Control for MR Damper for Structure*. Fifth World Congress on Intelligent Control and Automation, Hangzhou, China, Vol.3, pp: 2428-2432, 2004.

Lita M., Popa N.C., Velescu C. and Vekas L.N. *Investigations of a Magnetorheological Fluid Damper*. IEEE Transactions on Magnetics, Vol.40, pp: 469-472, 2004.

Lonnie J.L. and Wayne J.B. *Force Reflecting Teleoperation with Adaptive Impedance Control*. IEEE Transaction on Systems, Man, and Cybernetics - Part B: Cybernetics, Vol. 34, No. 1, pp: 159-165, 2004.

Lu R.X.J., Silva C.W. de, Ang Jr. M.H, Poo J.A.N. and Corporaal H. *A New Approach for Mechatronic System Design: Mechatronic Design Quotient*. International Conference on Advanced Intelligent Mechatronics. Monterey, California, USA, pp: 911-915, 2005.

McBean J. and Breazeal C. *Voice Coil Actuators for Human-Robot Interaction - An Exploration of the use of Electromagnetic Voice Coils as Compliant, Force-Controlled Actuators in Direct-Drive Robots for Visual and Tactile Interaction with Humans*. IEEE International conference on Intelligent Robots and Systems, Sendai, Japan, pp: 852-858, 2004.

Morrell J.B. and Salisbury J.K. *Parallel Coupled Actuators for High Performance Force Control: A Micro-Macro Concept*. IEEE International conference on Intelligent Robots and Systems, Pittsburgh, USA, pp: 391-398, 1995.

Morrell J.B. *Parallel Coupled Micro-Macro Actuators*. PhD thesis, Massachusetts Institute of Technolog, USA, 1996.

Niksefat N. and Sepehri N. *Designing Robust Force Control of Hydraulic Actuators Despite System and Environmental Uncertainties*. IEEE Control Systems Magazine, pp: 66-77, April 2001.

Nitish M. and Shahram P. *Force Control Strategies for Compliant and Stiff Contact: An Experimental Study*. IEEE International conference on Systems, Man, and Cybernetics, San Antonio, USA, pp: 1285-1290, 1994.

Pan G., Matsuhisa H. and Honda Y. *Analytical Model of a Magnetorheological Damper and Its Application to the Vibration Control*. IEEE International Conference on Industrial Electronics, Control and Instrumentation, Nagoya, Japan, pp: 1850-1855, 2000.

Pandian S.R. and Takemura F. *Control Performance of an Air Motor - Can Air Motors Replace Electric Motors?*. IEEE International Conference on Robotics and Automation, Detroit, USA, pp: 518-524, 1999.

Papadopoulos C.A. *Brakes and Clutches Using ER Fluids*. Mechatronics, pp.719-726, 1998.

Pratt G.A. and Williamson M.M. *Series Elastic Actuators.* IEEE International Conference on Intelligent Robots and Systems, Pittsburgh, USA, vol. 1, pp: 399-406, 1995.

Pratt G.A., Williamson M.M., Dillworth P., Pratt J., Ulland K. and Wright A. *Stiffness Isn't Everything.* Fouth International Symposium on Experimental Robotics, Stanford, USA, 1995.

Pratt G.A., Willisson P., Bolton C. and Hofman A. *Late Motor Processing in Low-Impedance Robots: Impedance Control of Series-Elastic Actuators.* American Control Conference, Boston, USA, Vol. 4, pp: 3245-3251, 2004.

Raibert M. H. and Craig J. J. *Hybrid Position/Force Control of Manipulators.* Journal of Dynamic Systems, Measurement, and Control, Vol.102, NO.6, pp:126-133, 1981.

Richard C. D. and Robert H. B. *Modern Control Systems.* Prentice Hall, 1997.

Robinson D. W. and Pratt J. E. *Series Elastic Actuator Development for a Biomimetic Walking Robot.* IEEE/ASME Conf. on Advanced Intelligent Mechatronics, Atlanta, USA, pp: 561-568, 1999.

Robinson D. W. *Design and Analysis of Series Elasticity in Closed-loop Actuator Force Control.* PhD thesis, Massachusetts Institute of Technolog, USA, 2000.

Robinson D. W. and Pratt G. A. *Force Controllable Hydro-Elastic Actuator.* IEEE International Conference on Robotics and Automation, San Francisco, USA, pp: 1321-1327, 2000.

Roy J. and Whitecomb L.L. *Adaptive Force Control of Position/Velocity Contolled Robots: Theory and Experiment.* IEEE Transactions on Robotics and Automation, Vol. 18, No. 2, pp: 121-137, 2002.

Sakaguchi M. and Furusho J. *Development of ER Actuators and Their Applications to Force Display Systems* . IEEE Virtual Reality Annual International Symposium, Seattle, USA, pp: 66-70, 1998.

Sakakibara, S. *A two-armed intelligent robot assembles mini robots automatically* . 22nd International Conference on Industrial Electronics, Control, and Instrumentation, Hawaii, USA, Vol. 3, pp: 1879-1883, 1996.

Scarfogliero U., Folgheraiter M. and Gini G. *Advanced Steps in Biped Robotics: Innovative Design and Intuitive Control Through Spring-Damper Actuator* . 4th IEEE-RAS International Conference on Humanoid Robots, Los Angeles, USA, Vol. 1, pp: 196-214, 2004.

Sensinger J.W. and Weir R.F. *Design and Analysis of a Non-Backdrivable Series Elastic Actuator.* 9th International Conference on Rehabilitation Robotics, Chicago, USA, pp: 390-393, 2005.

Sharon A., Hogan N. and Hardt E.D. *High Bandwidth Force Regulation and Inertia Reduction Using a Macro/Micro Manipulator system.* IEEE International Conference on Robotics and Automation, Philadelphia, USA, pp: 126-132, 1988.

Shen Y., Xi N. and Li W.J. *Contact and Force Control in Microassembly.* IEEE International Symposium on Assembly and Task Planning, Besancon, France, pp: 60-65, 2003.

Shin D.H., Han D.H. and Kim H.J. *7. Open-Loop Velocity Control of the Troweling Robot.* IEEE/RSJ International Conference on Intelligent Robots and Systems, pp: 1920 - 1925, Vol.3, 1999.

Siciliano B. and Valavanis K.P. *Control Problems in Robotics and Automation.* Springer, London, 1998.

Silva C.W. de *Sensory Information Acquisition for Monitoring and Control of Intelligent Mechatronic System.* International Journal of Information Acquisition. Vol.1, No.1, pp: 89-99, 2004.

Silva C.W. de *Mechatronics - An Intelligent Approach.* CRC Press, Boca Roton, FL, 2005.

Spencer B.F., Dyke S.J., Sain M.K. and Carlson. J.D. *Phenomenological Model of A Magnetorheological Damper.* Journal of Engineering Mechanics, ASCE, pp: 230-238, 1997.

Stanway R. *The Development of Force Actuators Using ER and MR Fluid Technology.* IEE Colloquium on Actuator Technology: Current Practic and New Developments, pp: 6/1-6/5, 1995.

Steven D. E. and Warren P. S. *Three Dynamic Problems in Robot Force Control.* IEEE International Conference on Robotics and Automation, Scottsdale, USA, pp: 392-397, 1989.

Sugano S.,Tsuto S.and Kato I. *Force Control of the Robot Finger Joint equipped with Mechanical Compliance Adjuster.* International conference on Intelligent Robots and Systems, Raleigh, USA, pp: 2005-2012, 1992.

Sulzer J.S., Peshkin M.A. and Patton J.L. *MARIONET: An Exotendon-Driven Rotary Series Elastic Actuator for Exerting Joint Torque.* International conference on Robotics for Rehabilitation, Chicago, USA, 2005.

Sun H. and Chiu G. T.-C. *Nonlinear Observer Based Force Control of Electro-Hydraulic Actuators.* Proceedings of the American Control Conference, san Diego, USA, 1999.

Takesue N., Asaoka H., Lin J., Sakaguchi M., Zhang G. and Furusho J. *Development and Experiments of Actuator Using MR Fluid.* Proceedings of 2000 IEEE International Conference on Industrial Electronics, Control and Instrumentation, Nagoya, Japan, pp: 1838-1843, 2000.

Takesue N., Furusho J. and Sakaguchi M. *Improvement of Response Properties of MR-Fluid Actuator by Torque Feedback Control.* International Conference on Robotics & Automation, Seoul, Korea, pp: 3825-3830, 2001.

Takesue N., Kiyota Y. and Furusho J. *Development of fast response MR-Fluid Actuator.* SICE 2002, Proceedings of the 41st SICE Annual Conference, Osaka, Japan, Vol. 2, pp: 949-953, 2002.

Takesue N., Furusho J. and Kiyota Y. *Analytic and Experimental Study on Fast Response MR-fluid Actuator.* IEEE Int. Conf. on Robotics and Automation, Taipei, China pp: 202-207, 2003.

Vischer D.and Khatib O. *Design and Development of High-Performance Torque-Controlled Joints.* Transactions on Robotics and Automation, Vol.11, NO.4, 1995.

Valency T. and Zacksenhouse M. *Instantaneous Model Impedance Control for Robots.* IEEE/RSJ International Conference on Intelligent Robots and Systems, Takamatsu, Japan, Vol. 1, pp: 757-762, 2000.

Whitcomb L., Arimoto S., Naniwa T., and Ozaki F. *Experiments in Adaptive Model-Based Force Control.* IEEE International Conference on Robotics and Automation, Nagoya, Japan, pp: 1846-1853, 1995.

Whitney D.E. *Historical Perspective and State fo the Art in Robot Force Control.* IEEE International Conference on Robotics and Automation, St. Louis, USA, pp: 262-268, 1985.

Wilfinger L.S., Wen J.T. and Murphy S.H. *Integral Force Control with Robustness Enhancement.* IEEE Control Systems Magazine, Vol. 14, pp: 31-40, 1994.

Williamson M. M. *Series Elastic Actuators.* Master thesis, Massachusetts Institute of Technology, USA, 1995.

Williamson M. M. *Robot Arm Control Exploiting Natual Dynamics.* PhD thesis, Massachusetts Institute of Technology, USA, 1999.

Xu Y.S. and Paul R.P. *On Position Compensation and Force Control Stability of a Robot with a Compliant Wrist.* IEEE International Conference on Robotics and Automation, Philadelphia, USA, pp: 1173-1178, 1988.

Yabuta T., Yamada T., Tsujimura T. and Sakata H. *Force Control of Servomechanism Using Adaptive Control.* IEEE Journal of Robotics and Automation, Vol. 4, No. 2, 1988.

Yoo J.H. and Wereley N.M. *Design of a High-Efficiency Magnetorheological Valve.* Journal Intelligent Material System and Structures, Vol. 13, pp: 679-685, 2002.

Yoshikawa T., Sugie T. and Tanaka N. *Dynamics Hybrid Position/Force Control of Robot Manipulators - Controller Design and Experiment.* IEEE Journal of Robotics and Automation, Vol. 4, No. 6, 1988.

Yoshikawa T. *Force Control of Robot Manipulators.* IEEE International Conference on Robotics and Automation, pp: 220-226, San Francisco, USA, 2000.

Youcef-Toumi K. and Guts D.A. *Impact and Force Control.* IEEE International Conference on Robotics and Automation, Scottsdale, USA, pp: 410-416, 1989.

Yang J.H., Lian F.L. and Fu L.C. *Adaptive Hybrid Position/Force Control for Robotic Manipulators with Compliant Links.* IEEE International Conference on Robotics and Automation, Nagoya, Japan, pp: 603-608, 1995.

Zhou W., Chew C.-M. and Hong G.-H. *Property Analysis for Series MR-Fluid Damper Actuator System.* Proceedings of IEEE Conference on Robotics, Automation and Mechatronics (RAM04), Singapore, pp:560-565, 2004.

Zhou W., Chew C.-M. and Hong G.-H. *Inverse Dynamics Control of Series Damper Actuator Based on MR Fluid Damper.* IEEE/ASME International Conference on Advanced Intelligent Mechatronics (AIM05), Monterey, USA, pp:473-478, 2005.

Zhou W., Chew C.-M. and Hong G.-H.. *Development of A Compact Double-Disk Magneto-Rheological Fluid Brake.* Robotica, accepted, 2007

Zhu W.H. and Salcudean S.E. *Teleoperation with Adaptive Motion/Force Control.* IEEE International Conference on Robotics and Automation, Detroit, USA, pp: 231-237, 1999.

Zinn M., Khatib O., Roth B. and Salisbury, J.K. *A New Actuation Approach for Human Friendly Robot Design.* Proceedings of International Symposium on Experimental Robotics, Sant' Angelo d'Lschia, Italy, July, 2002.

Zinn M., Khatib O., Roth B. and Salisbury, J.K. *Towards A Human-Centered Intrinsically-Safe Robotic Manipulator.* Second IARP - IEEE/RAS Joint Workshop on Technical Challenges for Dependable Robots in Human Environments, LAS-CNRS, Toulouse, France, October 2002

Zinn M., Khatib O., Roth B. and Salisbury, J.K. *Actuation Methods For Human-Centered Robotics and Associated Control Challenges.* Second Joint CSS/RAS International Workshop on Control Problems in Robotics and Automation, Las Vegas, NV, December 2002.

WEBSITES

1. Force Control Actuator, ME Dept, NUS
http://guppy.mpe.nus.edu.sg/%7Elegged_group/serieselasticactuators.htm/.

2. SDA system performance demostration - low output impedance.
http://guppy.mpe.nus.edu.sg/%7Elegged_group/SysDemo1.wmv.

3. SDA system performance demostration - high impact torlerance ability.
http://guppy.mpe.nus.edu.sg/%7Elegged_group/ExpVideo2.wmv.

Appendix A

Proof of the Statements

Statement 1: To ensure a minimum overall bandwidth ω_{min} for the SDA plant, the damper bandwidth should satisfy following requirement:

$$\omega_D \geq \frac{1}{0.64}\omega_{min}$$

Proof:

The model of SDA plant and its block diagram are shown in Fig.A.1. In the SDA plant, a DC motor (assuming with armature control) is series connected with a damper. The motor input is armature voltage U, output is motor velocity V. The damper input is motor velocity V and output is damping force F. G_m, G_D and G_s are the transfer functions of motor, damper and the SDA plant respectively.

Therefore,

$$G_m = \frac{V(s)}{U(s)} \tag{A.1}$$

$$G_D = \frac{F(s)}{V(s)} \tag{A.2}$$

$$G_s = G_m G_D = \frac{F(s)}{U(s)} \tag{A.3}$$

The transfer function of a DC motor (armature control) can be represented as a first order model (Dorf, 2004). And as mentioned in Section 6.1.1, the transfer function of damper can also be expressed with a first order model(Zhou, 2005-1).

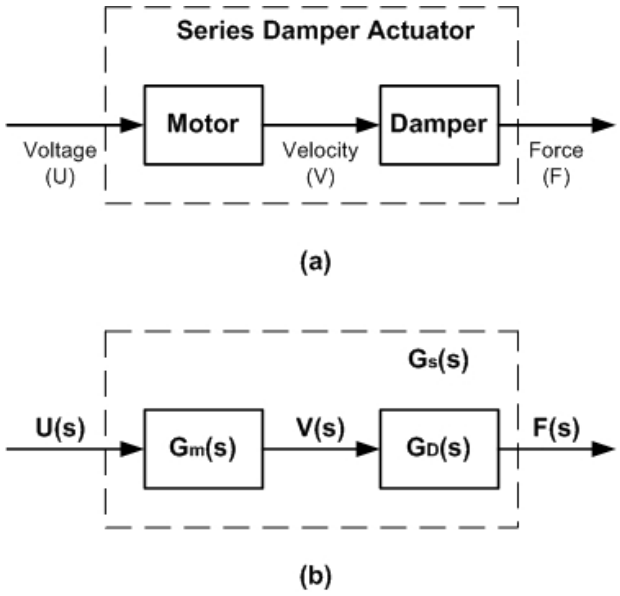

Figure A.1: SDA Plant model (a) and the block diagram (b)

Therefore, we can give following assumptions:

$$G_m(s) = K_m \frac{\omega_m}{s + \omega_m} \tag{A.4}$$

$$G_D(s) = B \frac{\omega_D}{s + \omega_D} \tag{A.5}$$

where K_m is the gain of the motor, ω_m is the bandwidth of the motor, B is the gain of the damper, and ω_D is the bandwidth of the damper.

Therefore, the transfer function of the SDA plant can be written that:

$$G_s(s) = G_m G_D = K_m B \frac{\omega_m \omega_D}{s^2 + (\omega_m + \omega_D)s + \omega_m \omega_D} \tag{A.6}$$

Denote the bandwidth of SDA plant by ω_s. It can be known from Eq. A.6 that, ω_s is fully determined by ω_m and ω_D. Now let's discuss the relationship between ω_s, ω_m and ω_D.

Assume that:

$$\omega_1 = max\{\omega_m, \omega_D\} \tag{A.7}$$

$$\omega_2 = min\{\omega_m, \omega_D\} \tag{A.8}$$

Then Eq. A.6 can be rewritten as:

$$G_s(s) = K_m B \frac{\omega_1 \omega_2}{s^2 + (\omega_1 + \omega_2)s + \omega_1 \omega_2} \tag{A.9}$$

Normalizing Eq. A.9 by ω_2^2 gives that:

$$G_s(S) = K_m B \frac{\omega_1/\omega_2}{(s/\omega_2)^2 + (1 + \omega_1/\omega_2)(s/\omega_2) + \omega_1/\omega_2} = K_m B \frac{r}{S^2 + (1+r)S + r} \tag{A.10}$$

where $S = s/\omega_2$, $r = \omega_1/\omega_2 \geq 1$.

Based on the definition of bandwidth, the bandwidth of SDA plant, ω_s, can be calculated from follow equation:

$$\frac{|G_s(j\omega_s)|}{K_m B} = -3dB \tag{A.11}$$

Solving Eq. A.11 gives that:

$$\omega_s = \omega_2 \sqrt{\frac{\sqrt{(r^2+1)^2 + 4r^2} - (r^2+1)}{2}} \tag{A.12}$$

When $r = 1$, it gives that:

$$\omega_s = \omega_2 \sqrt{\sqrt{2} - 1} = 0.64\omega_2 \tag{A.13}$$

Plot ω_s/ω_2 versus r and show in Fig.A.2. Plot the bode gain of $G_s(S)$ (Eq. A.10 with different values of r and show in Fig.A.3.

It can be seen from Fig.A.2, with the increasing of r, ω_s approaches to ω_2. If $r >> 1$, that is $\omega_1 >> \omega_2$, then $\omega_s = \omega_2$. With the decreasing of ω_1, the ratio of ω_s over ω_2 will also deceases. The minimum of ω_s is $\omega_s = 0.64\omega_2$ when $\omega_1 = \omega_2$. Same results can be observed from Fig.A.3, the bode gain of $G_s(S)$ with different valuse of r. The bandwidth of $G_s(S)$, the frequency where the gain drops to $-3dB$, increase from $0.64\omega_2$ to ω_2 with the increasing of r.

Now, it can be concluded that the bandwidth of SDA plant,ω_s, is varying from

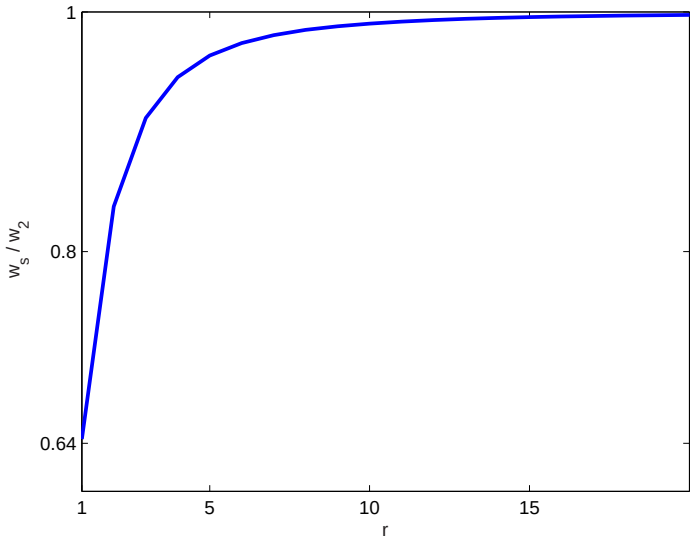

Figure A.2: Bandwidth of SDA plant (G_s) with different values of r

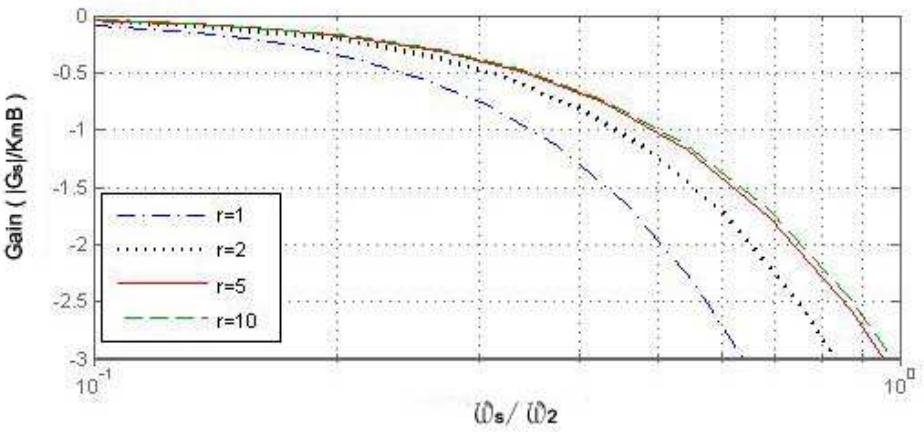

Figure A.3: Bode gain of SDA plant (G_s) with different values of r

100% to 64% of ω_2, that is the smaller one of motor bandwidth (ω_m) and damper bandwidth (ω_D), depending on the ration between them ($r = \omega_1/\omega_2$). Therefore, if the bandwidth of motor and damper are both larger than $\frac{1}{0.64}\omega_{min}$, the overall bandwidth of SDA system ω_s must be larger than ω_{min}. In other words, the sufficient condition for $\omega_s \geq \omega_{min}$ is:

$$\omega_m \geq \frac{1}{0.64}\omega_{min} \qquad and \qquad \omega_D \geq \frac{1}{0.64}\omega_{min}$$

The Statement 1 is proved.

Statement 2: To ensure a minimum overall bandwidth ω_{min} for the SDA plant, the DC motor (free end) bandwidth $\omega_{m'}$ should satisfy following requirement:

$$\omega_{m'} \geq \frac{J_m + J_D/N^2}{0.64 J_m}\omega_{min}$$

Proof:

The DC motor (armature control) transfer function can be written as (Dorf, 2004):

$$G_m(s) = \frac{V(s)}{U(s)} = \frac{\frac{k_t}{R_a J}}{s + \frac{k_e k_t + R_a b}{R_a J}} = K_m \frac{\omega_m}{s + \omega_m} \tag{A.14}$$

where b is equivalent viscous coefficient reflected at motor shaft, J is equivalent inertia reflected at motor shaft, ω_m is the motor bandwidth, and

$$\omega_m = \frac{k_e k_t + R_a b}{R_a J} \tag{A.15}$$

In the SDA plant, the motor shaft is connected with the damper input end via a gear reduction as shown in Fig.A.4, Where b_m is rotor damping coefficient of the motor, J_m is rotor inertia, N is gear ratio, J_D is the series damper input shaft inertia, and B is damping coefficient of the series damper and $B \geq 0$.

It can be known that:

$$b = b_m + B/N^2 \tag{A.16}$$

$$J = J_m + J_D/N^2 \tag{A.17}$$

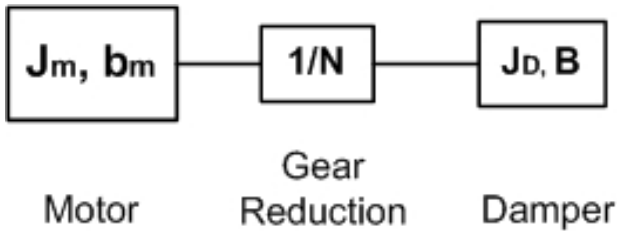

Figure A.4: Motor connected with damper via a gear reduction of a ratio N

When the motor output end is free (without the connection with the series damper), the motor bandwidth $\omega_{m'}$ can be written as:

$$\omega_{m'} = \frac{k_e k_t + R_a b_m}{R_a J_m} \tag{A.18}$$

Since $B \geq 0$, it can be written that:

$$\frac{\omega_m}{\omega_{m'}} = \frac{\frac{k_e k_t + R_a b}{R_a J}}{\frac{k_e k_t + R_a b_m}{R_a J_m}} \geq \frac{\frac{k_e k_t + R_a b_m}{R_a J}}{\frac{k_e k_t + R_a b_m}{R_a J_m}} = \frac{J_m}{J} = \frac{J_m}{J_m + J_D/N^2} \tag{A.19}$$

Therefore

$$\omega_m \geq \frac{J_m}{J_m + J_D/N^2}\omega_{m'} \tag{A.20}$$

According to the conclusion made in Appendix A, the motor bandwidth ω_m should satisfy:

$$\omega_m \geq \frac{1}{0.64}\omega_{min} \tag{A.21}$$

Therefore, combining Eq. A.20, the sufficient condition for Eq. A.21 is:

$$\omega_{m'} \geq \frac{J_m + J_D/N^2}{0.64 J_m}\omega_{min} \tag{A.22}$$

Then the Statement 2 is proved.